

# An Investigation of Satellite Maneuvering and Orientation Strategies using an Air Bearing Table



THESIS PRESENTED IN PARTIAL FULFILLMENT OF THE REQUIREMENTS  
FOR THE DEGREE OF MASTER OF SCIENCE IN ELECTRICAL &  
ELECTRONIC ENGINEERING AT THE UNIVERSITY OF STELLENBOSCH

SUPERVISOR: MNR J TREURNICHT

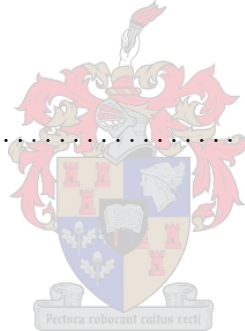
DECEMBER 2005

# Declaration

I, the undersigned, hereby declare that the work contained in this thesis is my own original work and that I have not previously in its entirety or in part submitted it at any university for a degree.

Signature: .....

Date: .....



# Abstract

In this thesis, the maneuvering and orientation of an inspection/service satellite is investigated. This thesis will demonstrate a simplified satellite maneuver around another satellite (for docking purposes). This is illustrated with a cart on an air bearing table (frictionless environment) which simplifies the problem to two dimensions.

A mathematical model of the system was designed and simulated (Matlab) for this maneuver. With the simulation, different strategies were considered to maneuver the cart in a circle around another object. The conclusion was made that approximating the circle with segments would conserve propellant. This strategy was implemented on the air bearing table.

Implementation on the air bearing table required several sensors and actuators. The cart is fitted with two thrusters and a momentum wheel for maneuvering and orientation. Sensors included a yaw rate gyro, dual axes accelerometer and absolute position sensor. The absolute position sensor was implemented with two ultrasonic sensors. With the measurements from the sensors an Extended Kalman Filter was implemented to estimate states.

Windows based control software used state estimates and measurements from sensors to implement the strategy. This program communicates via an RF-link to a microprocessor on the cart to give actuator commands. The maneuver around an object was successfully implemented on the air bearing table using two different orientation strategies, (1) rotation with the angle controller and (2) open loop angle control with the momentum wheel.

# Uittreksel

In hierdie tesis is die beweging en orientasie van 'n inspeksie satelliet ondersoek. 'n Eenvoudige satelliet beweging rondom 'n ander satelliet word gedemonstreer met 'n kar op 'n lugtafel (wrywinglose oppervlak) wat die probleem tot twee dimensies vereenvoudig.

'n Wiskundige model van die stelsel is ontwerp en gesimuleer (Matlab) vir die beweging. Verskillende strategië is ondersoek vir sirkel beweging. Die gevolgtrekking is gemaak deur die sirkel met segmente te benader gas gespaar word. Laasgenoemde strategie is geïmplementeer op die lugtafel.

Die volgende sensors en aktueerders is gemonteer op die kar vir implimentering van die strategie. Die kar het twee stuwars en 'n reaksie wiel vir beweging en orientasie. Sensors sluit in 'n giro, twee as versnellingsmeter en absolute posisie sensor. Die absolute posisie sensor bestaan uit twee ultrasoniese sensore. 'n Uitgebreide Kalman filter is ontwerp om toestande af te skat wat nie deur die sensore gemeet word nie.

Die beheer program (Windows gebaseerd) gebruik afgeskatte toestande en metings van die sensore om die beheer strategie te implementeer. Die program kommunikeer deur 'n RF-skakel met die mikroverwerker om aktueerder bevale te gee. Die suksesvolle beweging van die kar om 'n objek op die lugtafel is geïmplimenter met twee verskillende orientasie strategië, (1) orientasie met behulp van 'n hoek beheerder en (2) ooplus hoek beheer met die reaksie wiel.



# Acknowledgements

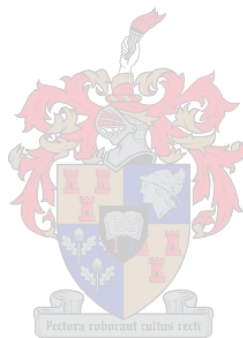
I would like to thank the following people for their help during this thesis:

- Thank you God for your helping hand.
- Mnr. J. Treurnicht, my supervisor, for his help and guidance throughout this thesis
- Corne van Daalen for all his help especially on controller implementation.
- Iain Peddle for his explanation of the mathematical model and EKF.
- Everybody in the ESL lab for all their help and motivation. From carrying the cart to EKF design.
- Nic Northcote for help, motivation and proof reading this thesis.
- Last but definitely not the least my 2nd year colleague's in no specific order: Fanus Groenewald, Cobus Jacobs, Pieter Theron and Jacob Venter for their help, understanding and motivation.



# Contents

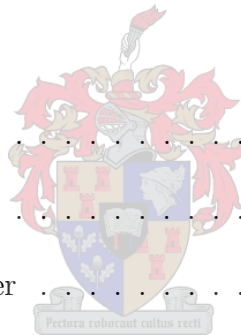
<b>Declaration</b>	<b>ii</b>
<b>Abstract</b>	<b>iii</b>
<b>Uittreksel</b>	<b>iv</b>
<b>Acknowledgements</b>	<b>v</b>
<b>List of Figures</b>	<b>xi</b>
<b>List of Tables</b>	<b>xvi</b>
<b>Nomenclature</b>	<b>xvii</b>
<b>Nomenclature</b>	<b>xvii</b>
<b>1 Introduction</b>	<b>1</b>
1.1 Task Description . . . . .	4
1.2 Overview of System . . . . .	5
1.2.1 Objectives . . . . .	5
1.2.2 Equipment . . . . .	6
<b>2 Overview of system</b>	<b>7</b>
2.1 Mathematical model . . . . .	7



2.1.1	Coordinate System . . . . .	7
2.1.2	Equations of Motion . . . . .	10
2.1.3	Extended Kalman Filter [EKF] . . . . .	11
2.2	Hardware . . . . .	13
2.2.1	Satellite Simulator . . . . .	13
2.2.2	Thrusters . . . . .	14
<b>3</b>	<b>Strategy of Satellite Attitude and Position Control</b>	<b>16</b>
3.1	Different Circular Strategy Options . . . . .	19
3.1.1	Circular . . . . .	20
3.1.2	N-Segment . . . . .	21
3.2	Results Analysis . . . . .	27
3.2.1	Strategy . . . . .	27
3.2.2	System Requirements . . . . .	29
<b>4</b>	<b>Sensor and Actuator Development</b>	<b>30</b>
4.1	Angle and Range Sensor . . . . .	30
4.1.1	Alternatives . . . . .	30
4.1.2	Beam Width . . . . .	32
4.1.3	Obtaining Position . . . . .	33
4.1.4	Implementation . . . . .	36
4.2	Momentum Wheel . . . . .	37
4.2.1	Current Loop . . . . .	37
4.2.2	Velocity Loop . . . . .	40
4.3	Accelerometer . . . . .	44

<b>5</b>	<b>Implementation of Strategy</b>	<b>45</b>
5.1	Angular Velocity Control . . . . .	45
5.1.1	Simulation . . . . .	45
5.1.2	Results . . . . .	47
5.2	Angle Control . . . . .	48
5.2.1	Simulation . . . . .	48
5.2.2	Results . . . . .	49
5.3	Extended Kalman Filter [EKF] . . . . .	50
5.3.1	Simulation of the EKF . . . . .	50
5.3.2	Implementing the EKF . . . . .	53
5.4	Overview of System . . . . .	53
<b>6</b>	<b>Simulation Results</b>	<b>57</b>
6.1	Two Different Rotation Strategies . . . . .	57
6.1.1	Angle Control . . . . .	57
6.1.2	Open Loop Angle Control . . . . .	59
6.2	Results . . . . .	60
6.2.1	Angle Control . . . . .	60
6.2.2	Open Loop Angle Control . . . . .	62
6.3	Kalman Filter Correction . . . . .	64
<b>7</b>	<b>Conclusion</b>	<b>65</b>
7.1	Summary . . . . .	65
7.2	Recommendations . . . . .	67
	<b>Bibliography</b>	<b>68</b>

<b>A Strategy Results</b>	<b>71</b>
A.1 Sensor Angle Width . . . . .	71
<b>B Ultrasonic Sensor</b>	<b>73</b>
B.1 Aperture Mask . . . . .	73
B.2 Sensor position . . . . .	75
B.3 Object position . . . . .	76
B.4 Signal Inversion . . . . .	77
B.5 Flow Chart of position detection program . . . . .	77
<b>C DC motor model</b>	<b>78</b>
<b>D Current Loop</b>	<b>83</b>
D.1 Sampling frequency . . . . .	83
D.2 Current Measurement . . . . .	84
D.3 Current Loop Controller . . . . .	85
<b>E Velocity Loop</b>	<b>87</b>
E.1 Discrete Controller . . . . .	87
E.2 Velocity measurement . . . . .	88
E.3 Anti Aliasing filter . . . . .	89
E.4 Pre-Filter . . . . .	90
<b>F Strategy Implementation</b>	<b>91</b>
F.1 Inertial relationship between the Momentum wheel and Cart . . . . .	91
F.2 Discrete controller of the cart angular velocity . . . . .	91
F.3 Conversion of gyro measurement . . . . .	92



F.4 Inertial measurement of the Cart . . . . . 93

F.5 Plant simplification of the Angular velocity controller . . . . . 94

F.6 Angle acquire constant . . . . . 95

**G EKF 97**

G.1 EKF equation derivation . . . . . 97

G.2 EKF variance calculation . . . . . 97

**H Simulation Results 99**

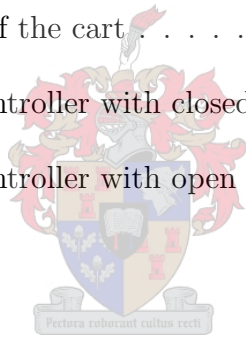
H.1 Control strategy with angle controller . . . . . 99

H.2 Control strategy with open loop angle control . . . . . 100

H.3 Angular Acceleration of the cart . . . . . 100

H.4 Results for strategy controller with closed loop angle control . . . . . 101

H.5 Results for strategy controller with open loop angle controller . . . . . 104



# List of Figures

1.1	Autonomous satellite docking system [21] . . . . .	1
1.2	Air Bearing Table Testing with Chaser on left and Target on Right [21] . . . . .	2
1.3	Satellite arm deployment for docking [22] . . . . .	3
2.1	Coordinate system . . . . .	8
2.2	The Euler Angles: Yaw $\psi$ , Pitch $\theta$ and Roll $\phi$ [ (3-2-1) sequence ] . . . . .	9
2.3	Illustration of 6 DOF equation of Motion . . . . .	10
2.4	Picture of air bearing table and cart . . . . .	13
2.5	Picture of cart . . . . .	14
2.6	Thruster . . . . .	14
2.7	Thruster profile from [20] with permission from author . . . . .	15
3.1	Circular movement of Satellite . . . . .	16
3.2	Circular movement . . . . .	17
3.3	Circular movement in segments . . . . .	17
3.4	Circle divided in segments . . . . .	18
3.5	4 segment illustration of movement . . . . .	18
3.6	Simulink Model of Strategy . . . . .	19
3.7	Circular Motion . . . . .	20
3.8	Measurements of Circular motion . . . . .	21

3.9	Resultant velocity vector . . . . .	21
3.10	Resultant velocity vector (Fig. 3.9 [zoomed]) . . . . .	22
3.11	Simulation of cart motion on the segments and heading of cart (Using Y thruster) . . . . .	23
3.12	Measurements of strategy simulation (Using Y thruster) . . . . .	23
3.13	Simulation of cart motion on the segments and heading of cart (Using X and Y thrusters) . . . . .	24
3.14	Measurements of strategy simulation (Using X and Y thrusters) . . . . .	25
3.15	Simulation of cart motion on the segments, cart stopped at end . . . . .	26
3.16	Measurements of strategy simulation, cart was stopped at end . . . . .	26
3.17	Total time thrusters are activated . . . . .	27
3.18	Sensor Angle Width vs. N-segments . . . . .	28
3.19	Total thrust time and sensor angle width for a different number of segments . . . . .	28
3.20	Thruster topology . . . . .	29
4.1	Light reflection from Solar Cell . . . . .	31
4.2	Ultrasonic sensor beam width [6] . . . . .	32
4.3	Sensor position . . . . .	34
4.4	Position calculation . . . . .	35
4.5	Beam angle crossing . . . . .	35
4.6	Timing diagram of ultrasonic sensors . . . . .	36
4.7	Angle and Distance measurement of Ultrasonic sensors . . . . .	37
4.8	Driving circuit for the Momentum Wheel from Fig. C.2, Fig. C.3 and Fig. C.4 . . . . .	38
4.9	DC Motor Block Diagram . . . . .	38
4.10	One leg of the H-bridge driving the DC Motor (From Fig. 4.8) . . . . .	39



4.11	Current Loop Block Diagram with scaling factors . . . . .	39
4.12	Current Loop Step response . . . . .	40
4.13	Velocity Loop Block diagram . . . . .	40
4.14	Simplified velocity controller block diagram . . . . .	41
4.15	Tacho velocity measurement from Fig. C.2, Fig. C.3 and Fig. C.4 . . . . .	42
4.16	Simulink model of velocity controller . . . . .	42
4.17	Simulink model of current loop in velocity controller [Fig. 4.16] . . . . .	43
4.18	Step response of the Velocity Controller . . . . .	43
4.19	Accelerometer measurement circuit for one axis . . . . .	44
5.1	Simulink model of Angular Velocity Plant . . . . .	46
5.2	Bode plot of closed loop plant . . . . .	47
5.3	Step response of cart angular velocity controller . . . . .	47
5.4	Angular controller Simulink model . . . . .	48
5.5	Bode plot of closed loop Angle controller . . . . .	49
5.6	Step response of cart angle control . . . . .	49
5.7	EKF measurements . . . . .	50
5.8	Block diagram of System with Controller and EKF . . . . .	51
5.9	Simulation and EKF measurements . . . . .	52
5.10	System layout . . . . .	53
5.11	Flow chart of program on microprocessor . . . . .	55
5.12	Flow chart of Delphi program . . . . .	56
5.13	Control program GUI . . . . .	56
6.1	Initial condition of cart . . . . .	57
6.2	Control steps on each segment . . . . .	58

6.3	Angle control of cart . . . . .	59
6.4	Cart movement around an object . . . . .	60
6.5	EKF state measurement angle $[\phi]$ and absolute velocity . . . . .	61
6.6	Uneven table . . . . .	61
6.7	Cart movement round an object . . . . .	62
6.8	EKF state measurement $[\phi]$ and absolute velocity . . . . .	63
6.9	Acceleration measurement and EKF position state measurement . . . . .	64
A.1	Sensor Angle Width . . . . .	71
A.2	Sensor Angle Width . . . . .	72
B.1	Aperture Mask of the Ultrasonic sensor . . . . .	73
B.2	Picture of Aperture Mask and Casing of the Ultrasonic Sensor . . . . .	74
B.3	Object detection . . . . .	76
B.4	ECHO inversion . . . . .	77
B.5	Flow chart of position detection program . . . . .	77
C.1	DC Motor equivalent circuit . . . . .	78
C.2	DC motor Electronics schematic . . . . .	80
C.3	DC motor Electronics schematic . . . . .	81
C.4	DC motor Electronics schematic . . . . .	82
E.1	Bode Plot of Closed loop Velocity Controller Plant . . . . .	88
E.2	Angular velocity in $[\text{rad/s}]$ to $[\text{ticks}]$ . . . . .	89
E.3	Butterworth low pass filter . . . . .	89
F.1	$\omega$ $[\text{rad/s}]$ to $\omega$ $[\text{ticks}]$ conversion of the cart . . . . .	92
F.2	Angular velocity of the momentum wheel and the cart . . . . .	93

F.3 Root locus of closed loop plant . . . . . 94

F.4 Bode plot of closed loop angular velocity plant and approximation . . . . . 94

F.5 Delta D . . . . . 95

F.6 Delta D (D1 - D2) . . . . . 96

H.1 Actuator commands of the cart . . . . . 101

H.2 Ultrasonic measurements . . . . . 102

H.3 EKF state measurements . . . . . 102

H.4 X and Y velocity estimates from EKF . . . . . 103

H.5 Actuator commands of the cart . . . . . 104

H.6 Ultrasonic measurements . . . . . 105

H.7 EKF state measurements . . . . . 105

H.8 Velocity estimates from EKF . . . . . 106



# List of Tables

2.1 Thruster force profile approximation parameters from [20] with permission from author . . . . .	15
4.1 Price Comparison . . . . .	31
4.2 Slit thickness . . . . .	33
4.3 Mosfet states . . . . .	37
F.1 Results of Moment of Inertia measurement . . . . .	93
H.1 Non Linear Strategy Controller . . . . .	99
H.2 Non Linear Strategy Controller . . . . .	100



# Nomenclature

## Acronyms

2D	2 Dimensional
A/D	Analog to Digital
ASDS	Autonomous Satellite Docking System
CCD	Charge Coupled Device
DC	Direct Current
DOF	Degrees of Freedom
EKF	Extended Kalman Filter
EMC	Electromagnetic current
ESL	Electronics Systems Laboratory
GUI	Graphical User Interface
HD	Hard Drive
KF	Kalman Filter
PCB	Printed Circuit Board
PI	Proportional Integral
PSD	Position Sensitive Device
PWM	Pulse Width Modulation
RF	Radio Frequency
RPM	Revolutions per minute
$T^{-1}$	Attitude Transformation Matrix
VELFBA	Velocity Feedback channel A
VELFBB	Velocity Feedback channel B



**Letters**

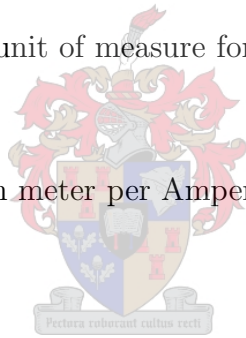
L	Torque on the X axis
M	Torque on the Y axis
N	Torque on the Z axis
p	Angular rate round the X-axis
q	Angular rate round the Y-axis
r	Angular rate round the Z-axis
$u$	Velocity in the X-axis
$\dot{u}$	Acceleration in the X-axis
$v$	Velocity in the Y-axis
$\dot{v}$	Acceleration in the Y-axis
$V_1$	Initial Velocity
$V_2$	Velocity on the next Segment
$V_R$	Resultant Velocity
$w$	Velocity in the Z-axis
$\dot{w}$	Acceleration in the Z-axis
X	Axis orthogonal to both the Y and Z axis
Y	Axis orthogonal to both the X and Z axis
Z	Axis orthogonal to both the Y and X axis

**Subscripts**

B	Body Axis
I	Inertial Axis
O	Orbital Axis
PWM	Pulse Width Modulation
s	Sampling time
X	Axis direction
Y	Axis direction
Z	Axis direction

**Abbreviations**

C	cos
cm	centimeter
F	Force
g	gravitational acceleration
Hz	Hertz
I	Moment of Inertia
kg	kilogram
kHz	kilo Hertz
LUX	The metric unit of measure for illuminance of a surface.
m	mass
MHz	Mega Hertz
mNm/A	milli Newton meter per Ampere
msec.	milli second
mV	milliVolt
nsec.	nano second
$\omega$	Angular Velocity
rad	radians
S	sin
sec.	second
T	Time
tx	X Thruster time ON
ty	Y Thruster time ON
$\mu$ sec	micro second
V	Volt
W	Watt



# Chapter 1

## Introduction

About 40 years ago the first automatic docking of satellites in space was done. This was a great achievement for scientists and engineers. This made it possible to build large space stations as individual pieces with the docking done autonomously. The risk of losing human life was now also less due to this. For example, a rescue vessel could be sent to another one in distress to help retrieve astronauts aboard.

Because it is very expensive to launch a satellite it is a challenge for an engineer to extend the life of the satellite. To solve this problem it would help if a satellite could be refueled or serviced to extend its life. If all satellites are made with the architecture to enable on-orbit servicing to upgrade the system or to refuel, it will cut the number of satellite launches thereby saving money. The idea is to have an industry wide on-orbit servicing infrastructure by having a standard autonomous docking system. For the orientation and maneuvering of a satellite, fuel is needed. With extra fuel the following is possible: redirection of orbit, observation of new crisis areas, and the number of satellites used for global coverage could be minimized.

A typical Autonomous Satellite Docking System (ASDS) from the Michigan Aerospace Corporation [21] is shown in Fig. 1.1.

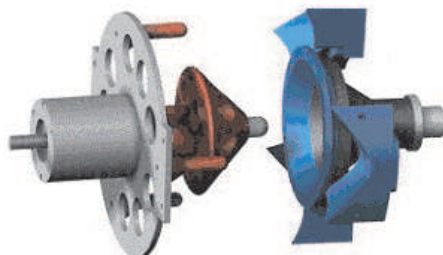


**Figure 1.1:** *Autonomous satellite docking system [21]*



The testing of their docking system was implemented on an air bearing table with two carts floating on compressed air by means of air bearing pads. This simulated two satellites in proximity. Each cart contained the following: an on-board computer for control and logging data, RF-link to communicate with a ground station and thrusters for maneuvering.

This simulation is frictionless due to the air cushions and a nearly perfectly flat table. This allows a 2D simulation of micro gravity maneuvers. Control software and position/orientation sensors guided the two satellites in proximity as if in-orbit. The chaser end of the docking mechanism was mounted to one of the carts and the target end to the other cart. The testing is illustrated in Fig. 1.2.

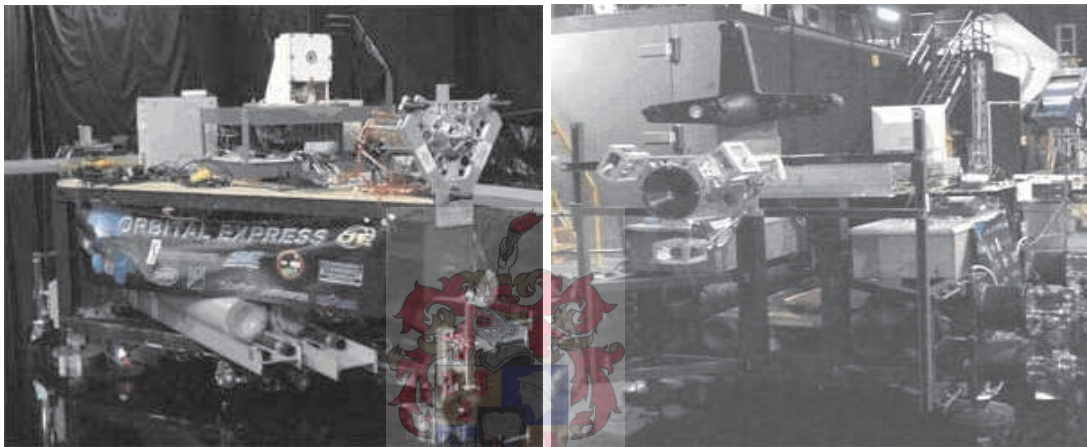


**Figure 1.2:** *Air Bearing Table Testing with Chaser on left and Target on Right [21]*

Critical components are a main cause of a short satellite lifetime. If satellites were made to be serviceable, these components could be replaced. An automated payload exchange system would be able to "repair" the satellite by replacing the damaged unit. Service/inspection satellites could also be used to deploy micro satellites for the following: earth aperture formation flight or deploying nano satellites for inspection to give a damage report on other satellites for repair.

Refueling and repairing satellites using space transportation systems is very expensive, orbit range limited and human lives are unnecessarily involved. Autonomous satellite docking systems would allow autonomous servicing and refueling without these risks.

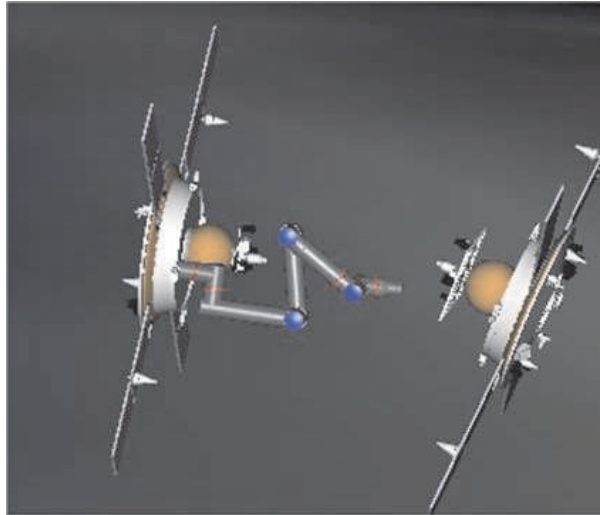


**Figure 1.3:** *Satellite arm deployment for docking [22]*

In this thesis, maneuvering and orientation of an inspection/service satellite is investigated. This thesis will demonstrate a simplified satellite maneuver around another satellite (for docking purposes). A technique is developed for the two dimensional case as implemented on the air bearing table. The development of the simulations and a demonstration of this technique is discussed in the next section.



## 1.1 Task Description

The aim of this thesis is to investigate and develop a strategy to maneuver and orientate a cart around another in a frictionless environment. The demonstration of the maneuver was done with a cart on an air bearing table similar to the experiment from Michigan Aerospace Corporation. The thesis is divided into the following tasks:

- **Mathematical Model / Simulation**

A mathematical model of the system was designed and simulated (Matlab) for the maneuver on the air bearing table. The model consisted only of 3DOF due to the 2 dimensional test environment. The model could be extended to 3 dimensions.

- **Strategy Analysis**

The primary objective is to maneuver the cart in a circle around another object. The size of the air bearing table limited the maneuver to a semicircle. The extension of the maneuver to a full circle is straightforward. To conserve gas, a semicircle could be approximated with segments. The most viable strategy is then implemented on the air bearing table.

- **Development of sensors and actuators**

From the simulation it is evident that a few extra sensors and actuators are necessary for the maneuver on the air bearing table. Existing sensor and actuators included a gyroscope and two thrusters. To maneuver and orientate the cart an absolute position sensor is needed. A few options were considered for implementation of this sensor on the air bearing table including optic, magnetic and ultrasonic technologies. For acceleration measurement of the cart an accelerometer is used. To enable the rotational control of the cart, a momentum wheel was developed.

- **Control Algorithm**

A control algorithm was developed that uses the available sensor inputs with an Extended Kalman Filter (EKF) to estimate other states.

- **Implementing and Testing**

The strategy was implemented on an air bearing table with a cart as the inspection satellite. The other satellite is represented by a stationary object to illustrate the concept.

## 1.2 Overview of System

### 1.2.1 Objectives

The presentation of the thesis document is given below:

**Chapter 2:** A brief explanation on coordinate systems is followed by the mathematical model. Then the EKF equations required for control are derived. This chapter also describes and references previous hardware work done including the cart and air bearing table.

**Chapter 3:** Strategies for maneuvering and orientation of the cart on a semicircle are investigated. This is done by simulation. The maneuver implemented is concluded from this. This enables the selection of suitable components used to implement the strategy.

**Chapter 4:** The choice of a suitable position sensor for the air bearing table scenario is discussed. The use of an accelerometer and the development of the momentum wheel are also included in this chapter.

**Chapter 5:** The objective of this chapter is the implementation of the strategy from Chapter 3. Controllers and the EKF needed for implementing the strategy are developed. An overview of the system is also given.

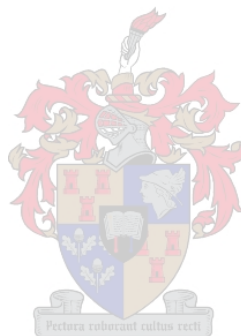
**Chapter 6:** This chapter includes control strategies and simulation results. The results are from two different orientation strategies and include actuator commands, position measurement and state estimation. EKF correction is explained as a conclusion to this Chapter.

**Chapter 7:** The final conclusion gives a summary of goals achieved and recommendations for future work are discussed.

## 1.2.2 Equipment

For simulating the satellite maneuver and orientation strategy an air bearing table and cart is used. The cart is currently fitted with 3 air bearing pads, 2 thrusters, 4 high-pressure compressed-air bottles and batteries. The cart and air bearing table was already constructed before hand. Fig. 2.5 and 2.4 illustrate the cart and air bearing table.

To implement the strategy and minimize costs, known and available off-the-shelf sensors were used such as an accelerometer and gyroscope. An absolute position sensor was developed by the author. For orientation control, a momentum wheel is used. The DC motor with wheel and driving circuit electronics were available for work described herein.



# Chapter 2

## Overview of system

### 2.1 Mathematical model

#### 2.1.1 Coordinate System

Spaceflight analysis requires knowing the apparent position and motion of objects as seen by the spacecraft. For this, a coordinate system must be chosen. Practically any coordinate system will do, but choosing the correct one can increase the insight into the problem by allowing concise analysis and simulation. To define the coordinate system two characteristics must be specified: the location of the center and what the coordinate system is fixed with respect to. The following three coordinate systems describe the attitude of a satellite: Body Coordinates, Orbital Coordinates and Inertial Coordinates from [14], [15] and [16].

- **Body Coordinates**

The center of mass of the satellite acts as the origin of the body coordinate system. The coordinate system is aligned with the body of the satellite. This reference frame is used to orientate the satellite with respect to another reference frame. The axes are defined as  $X_B$ ,  $Y_B$  and  $Z_B$ .

- **Orbital Coordinates**

The origin of the orbit coordinate system is also at the satellite's center of mass. This coordinate system is fixed with respect to the orbit. The  $Z_0$  axis points toward the earth center (Nadir pointing), the  $X_0$  axis is perpendicular to the  $Z_0$  axis and points in the direction of velocity in a circular orbit, and the  $Y_0$  axis is in the orbit anti-normal direction.

- **Inertial Coordinates**

The inertial reference  $X_I$ ,  $Y_I$  and  $Z_I$  frame has its origin at the center of the earth and is fixed with respect to inertial space. The  $Z_I$  axis is fixed with respect to the earth's geometric north pole, the  $X_I$  axis is in the Vernal Equinox direction and  $Y_I$  axis completes the orthogonal set.

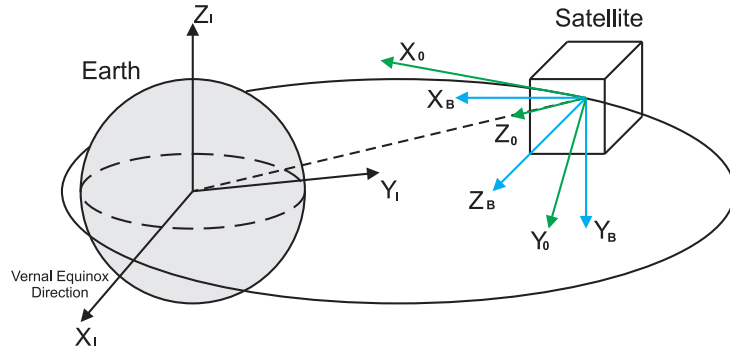


**Figure 2.1:** *Coordinate system*

Due to the nature of the task at hand, the maneuver around another satellite will change the position and angle of the coordinate system slightly. The body axes still remain at the origin of the satellite. The inertial reference changes with the origin at the center of another satellite. The attitude transformation matrix  $\mathbf{T}^{-1}$  to transform a vector from body coordinates to reference inertial coordinates (also called the inverse direction cosine matrix) is given by [17]:

$$\begin{bmatrix} u_I \\ v_I \\ w_I \end{bmatrix} = \mathbf{T}^{-1} \begin{bmatrix} u_b \\ v_b \\ w_b \end{bmatrix} \quad (2.1)$$

$$\mathbf{T}^{-1} = \begin{bmatrix} C\theta C\psi & S\phi S\theta C\psi - C\phi S\psi & C\phi S\theta C\psi + S\phi S\psi \\ C\theta S\psi & S\phi S\theta S\psi + C\phi C\psi & C\phi S\theta S\psi - S\phi C\psi \\ -S\theta & S\phi C\theta & C\phi C\theta \end{bmatrix} \quad (2.2)$$

where  $S = \sin$  and  $C = \cos$

Because the satellite maneuver is simulated on an air bearing table, a cart represents the satellite which maneuvers and orientates around another object. This simplifies the problem to two dimensions in which case  $\theta$  and  $\phi$  are zero.  $\mathbf{T}^{-1}$  then simplifies to:

$$\mathbf{T}^{-1} = \begin{bmatrix} C\psi & -S\psi & 0 \\ S\psi & C\psi & 0 \\ 0 & 0 & 1 \end{bmatrix} \quad (2.3)$$

The Euler angles from Eq. 2.2 are illustrated in Fig. 2.2.

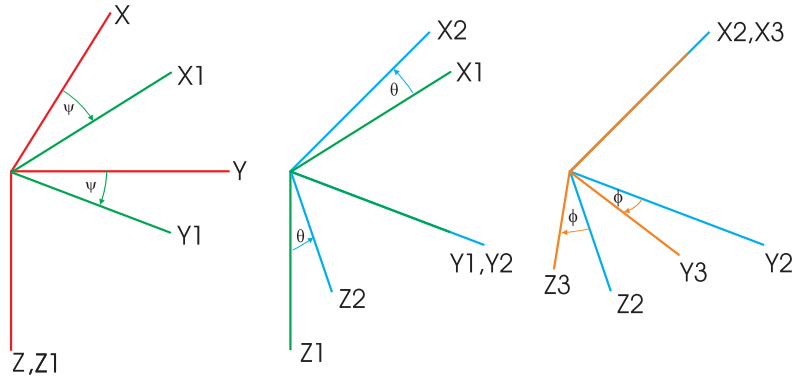


**Figure 2.2:** *The Euler Angles: Yaw  $\psi$ , Pitch  $\theta$  and Roll  $\phi$  [ (3-2-1) sequence ]*

The cart is maneuvered in the X-Y plane therefore the cart's body velocities are transformed to its inertial velocities with Eq. 2.1 and 2.3:

$$u_0 = u_b \cos(\psi) - v_b \sin(\psi) \quad (2.4)$$

$$v_0 = u_b \sin(\psi) + v_b \cos(\psi) \quad (2.5)$$

To calculate the Euler angles from the body rates (Chapter 2.1.2) the following rates are calculated and integrated [17]:

$$\begin{bmatrix} \dot{\phi} \\ \dot{\theta} \\ \dot{\psi} \end{bmatrix} = \begin{bmatrix} 1 & \sin(\phi) \tan(\theta) & \cos(\phi) \tan(\theta) \\ 0 & \cos(\phi) & -\sin(\phi) \\ 0 & \sin(\phi) \sec(\theta) & \cos(\phi) \sec(\theta) \end{bmatrix} \begin{bmatrix} p \\ q \\ r \end{bmatrix} \quad (2.6)$$

The cart only rotates in the  $Z_b$  axis due to the two dimensional movement, therefore  $p$  and  $q$  are zero. Eq. 2.6 now simplifies to,

$$\dot{\psi} = r \quad (2.7)$$

The cart attitude can also be represented with a quaternion, but due to the clear physical interpretation of this 3DOF model, Euler angles are used.



## 2.1.2 Equations of Motion

The satellite maneuver and orientation are represented with the 6 DOF Equations of Motion. To simplify matters the reference axis center is chosen at the body axis center. It is also assumed that the satellite center of mass is at the origin of this axis. The 6 DOF model for the body axes simplifies to [17],

$$m[\dot{u} + wq - rv] = F_X \quad (2.8)$$

$$m[\dot{v} + ur - pw] = F_Y \quad (2.9)$$

$$m[\dot{w} + vp - qu] = F_Z \quad (2.10)$$

$$I_x \dot{p} + (I_z - I_y)rq = L \quad (2.11)$$

$$I_y \dot{q} + (I_x - I_z)pr = M \quad (2.12)$$

$$I_z \dot{r} + (I_y - I_x)rq = N \quad (2.13)$$

where,

$m \Rightarrow$  mass

$u, v, w \Rightarrow$  Velocity in the X, Y and Z directions respectively

$p, q, r \Rightarrow$  Angular rate round the X, Y and Z axes respectively

$F_X, F_Y, F_Z \Rightarrow$  Forces in X, Y and Z directions respectively

$L, M, N \Rightarrow$  Torque on X, Y and Z axes respectively

$I_x, I_y, I_z \Rightarrow$  Moment of Inertia round the X, Y and Z axis

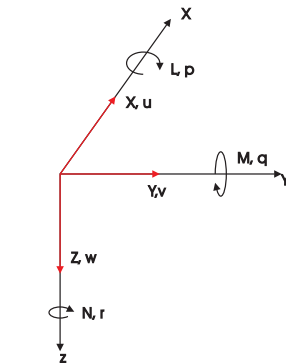


**Figure 2.3:** Illustration of 6 DOF equation of Motion

Due to the 2D assumptions from the previous section, the following are zero:  $p$ ,  $\dot{p}$ ,  $q$ ,  $\dot{q}$ ,  $L$ ,  $M$ ,  $w$  and  $Z$ . The 6 DOF model is now simplified to a 3 DOF model:

$$m[\dot{u} - rv] = F_X \quad (2.14)$$

$$m[\dot{v} + ur] = F_Y \quad (2.15)$$

$$I_z \dot{r} = N \quad (2.16)$$

These equations are used in the simulation of the strategy in Chapter 3.1. The equations are also the base of the non-linear Kalman filter [EKF] dynamic equations.

### 2.1.3 Extended Kalman Filter [EKF]

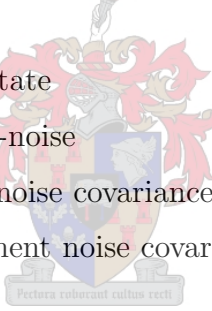
The EKF [12] is implemented due to the non-linear dynamic equations of motion from Eq. 2.14, 2.15 and 2.16. The measurement equations are also non-linear (see Section 5.3.1). For non-linear filters most systems may be described by:

$$\dot{\underline{x}}(t) = \underline{f}(\underline{x}, t) + \underline{w}(t) \quad \text{x-state} \quad (2.17)$$

$$y(t) = h(\underline{x}, t) + \underline{v}(t) \quad \text{w, v-noise} \quad (2.18)$$

$$Q = E[\underline{w} \underline{w}^T] \quad \text{process noise covariance} \quad (2.19)$$

$$R = E[\underline{v} \underline{v}^T] \quad \text{measurement noise covariance} \quad (2.20)$$



The discretized non-linear measurement equation:

$$\underline{y}_k = h(\underline{x}_k) + \underline{v}_k \quad (2.21)$$

Due to the non-linear system, a 1st order approximation (linearization) is used to describe the system dynamics in the vicinity of some state  $\underline{x} = \hat{\underline{x}}$  (current best estimate).

$$F_k = \left. \frac{\partial f(\underline{x})}{\partial \underline{x}} \right|_{\underline{x}=\hat{\underline{x}}_k} \quad (2.22)$$

$$H_k = \left. \frac{\partial h(\underline{x})}{\partial \underline{x}} \right|_{\underline{x}=\hat{\underline{x}}_k} \quad (2.23)$$

In order to make use of the discrete KF mathematics the discrete fundamental matrix is calculated with,

$$F_{dk} = I + F_k T_s + \frac{F_k^2 T_s^2}{2!} + \frac{F_k^3 T_s^3}{3!} + \dots \quad (\text{Taylor series expansion}) \quad (2.24)$$

Eq. 2.24 is usually approximated with,

$$F_{dk} = I + F_k T_s \quad (2.25)$$

With Eq. 2.23 and 2.25, the KF gain is calculated with,

$$M_k = F_{dk} P_{k-1} F_{dk}^T + Q_k \quad (2.26)$$

$$L_k = M_k H_k^T (H_k M_k H_k^T + R_k)^{-1} \quad (2.27)$$

$$P_k = (I - L_k H_k) M_k \quad (2.28)$$

$F_{dk}$  and  $H_k$  are updated on each KF sample time with new states,  $\hat{\underline{x}}$ .  $Q_k$ , the process noise covariance is,

$$Q_k = \int_0^{T_s} \Phi(t) Q \Phi(t)^T dt \quad (2.29)$$

The discretized measurement noise matrix  $R_k$  consists of a matrix of variances. Now with an updated  $L_k$ , the states must be propagated and the required innovation with measured data is done. The state propagation is of course non-linear, implying that we should perform integration of some kind to find what will be referred to as  $\bar{\underline{x}}_k$  from  $\dot{\underline{x}} = f(\underline{x}) + w$ . Euler integration is used for state propagation,

$$\bar{\underline{x}}_k = \hat{\underline{x}}_{k-1} + \dot{\hat{\underline{x}}}_{k-1} T_s \quad (2.30)$$

$$\text{with,} \quad (2.31)$$

$$\dot{\hat{\underline{x}}}_{k-1} = f(\hat{\underline{x}}_{k-1}) \quad \text{, non-linear dynamic equations} \quad (2.32)$$

The innovation is calculated with,

$$\hat{\underline{x}}_k = \bar{\underline{x}}_k + L_k [y_k - h(\bar{\underline{x}}_k)] \quad (2.33)$$

Note that  $h$  and  $f$  may also be functions of some deterministic input  $\underline{u}$  without loss of generality. The assumption of Eq. 2.25 instead of an higher order approximation, does not in general degrade the performance of the EKF. The reason for this is because the true non-linear dynamics are used to perform state propagation and  $F_{dk}$  is only used to find  $L_k$  and  $P_k$ . The EKF offers no guarantees as the linear system KF which relies heavily on  $P_k$  to give an indication of estimation accuracy and convergence.  $P_k$  may indicate excellent performance, while the filter performs poorly.

## 2.2 Hardware

### 2.2.1 Satellite Simulator

The satellite simulator consists of two parts. One is the air bearing table and the other a cart. The table frame is constructed with 15 adjustable metal legs. On top of this a table top consisting of a sheet of wood with glass on top. Glass gives a smooth surface for the cart to glide on. A barrier is fitted to the table top to stop the cart from falling off. The table is very stiff and is adjustable for leveling. Measurements of the table top are 3.24 X 1.87 m.

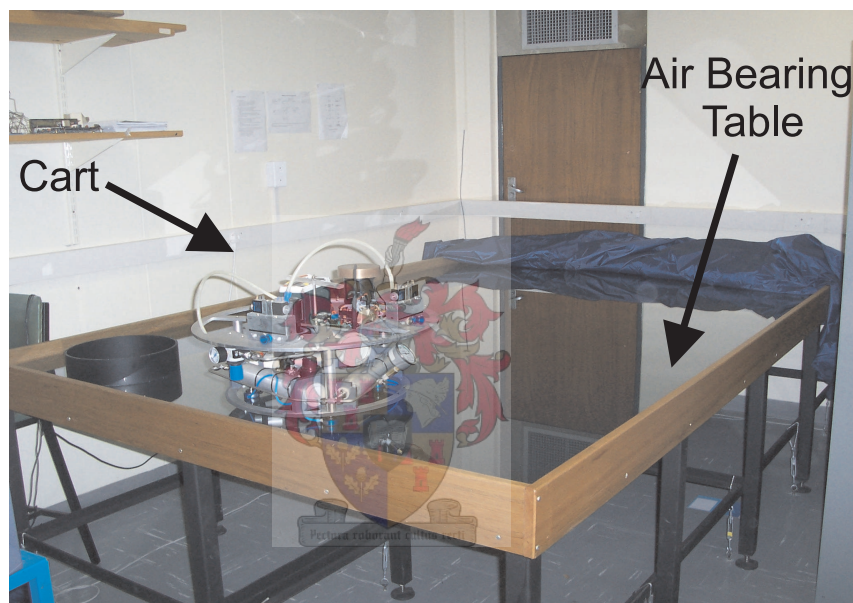


**Figure 2.4:** *Picture of air bearing table and cart*

The cart frame is constructed from aluminum and is fitted with three carbon feet, two thrusters, 4 gas canisters, batteries and electronics. The 3 carbon feet are supplied with nitrogen from 3 gas canisters. Pressure in these bottles varies from 50 - 180 bar to keep the cart adrift. The thrusters are supplied with nitrogen from 1 gas canister with a capacity of 180 bar. They are perpendicular to each other and are adjusted to thrust through the center of mass of the cart. The thruster characteristics are described further in Chapter 2.2.2.

There are two 12V lead acid batteries on the cart to power the electronics. Current electronics consist of a gyroscope [9] and a driving circuit for the thrusters. To implement the strategy discussed in Chapter 3, the cart must be able to maneuver and orientate on the air bearing table. The thrusters and momentum wheel are used for lateral maneuvers and orientation respectively. Sensors used to measure lateral movement and orientation are

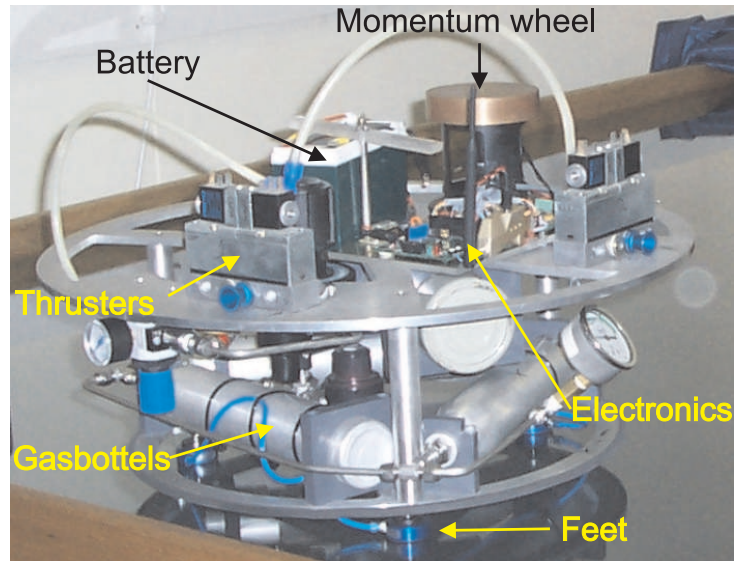


**Figure 2.5:** *Picture of cart*

an accelerometer and gyroscope. Maneuver and orientation requires an absolute position sensor which is designed in Chapter 4.1. The control and measurements of the sensors is done with a Cygnal F8051005 microprocessor [18].

## 2.2.2 Thrusters

Fig. 2.6 illustrates one of the FESTO thrusters mounted on the cart. The thruster is controlled by two electric coils rated 24V. A pneumatic switch is located below the coils. This switch requires a minimum gas pressure of 1 bar to open and close. By energizing one coil the thruster opens and by energizing the other the thruster is closed. Due to a rated pressure of 1 - 10 bar for a thruster, the gas is regulated. The nominal working value used is 5 bar.

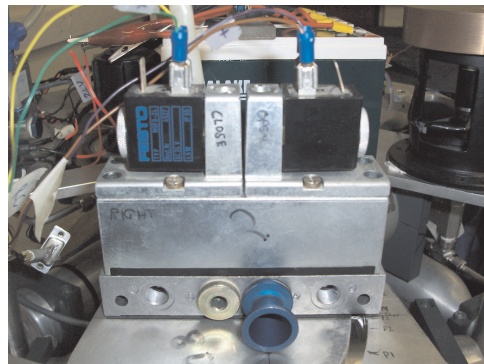


**Figure 2.6:** *Thruster*

The relationship between the block wave voltage input and the force output is known from [20]. The thruster profile was approximated with straight line sections. The turn-on and turn-off time, rise and fall time and steady state force level were identified with the criteria that the differences between the integral of the estimated and approximated force profiles are as little as possible. These criteria ensured that the energy contained in the estimated and approximated force profile was the same. The identified parameters are shown in Table 2.1.

Turn-on time	10msec.
Turn-off time	10msec.
Rise time	90msec.
Fall time	90msec.
Steady-state force	1.27N

**Table 2.1:** *Thruster force profile approximation parameters from [20] with permission from author*

The estimated thruster force profile, approximated force profile and input signal is shown in Figure 2.7.

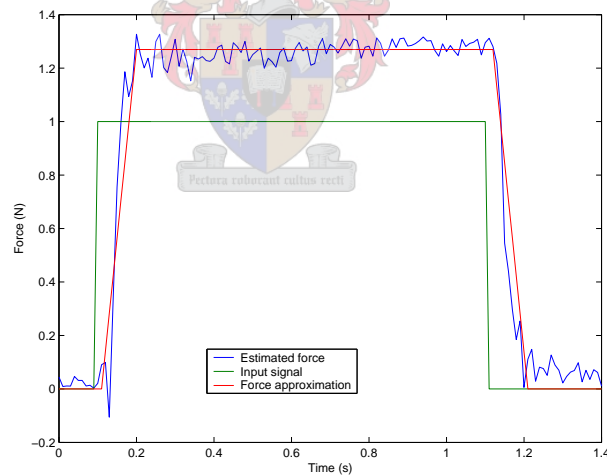


**Figure 2.7:** *Thruster profile from [20] with permission from author*

## Chapter 3

# Strategy of Satellite Attitude and Position Control

Different strategies for maneuvering around an object on the air bearing table are investigated. The requirements of a position sensor are dependent on what strategy is implemented. Due to the size of the table only a semicircle maneuver is considered. Fig. 3.1 illustrates the semicircle maneuver.

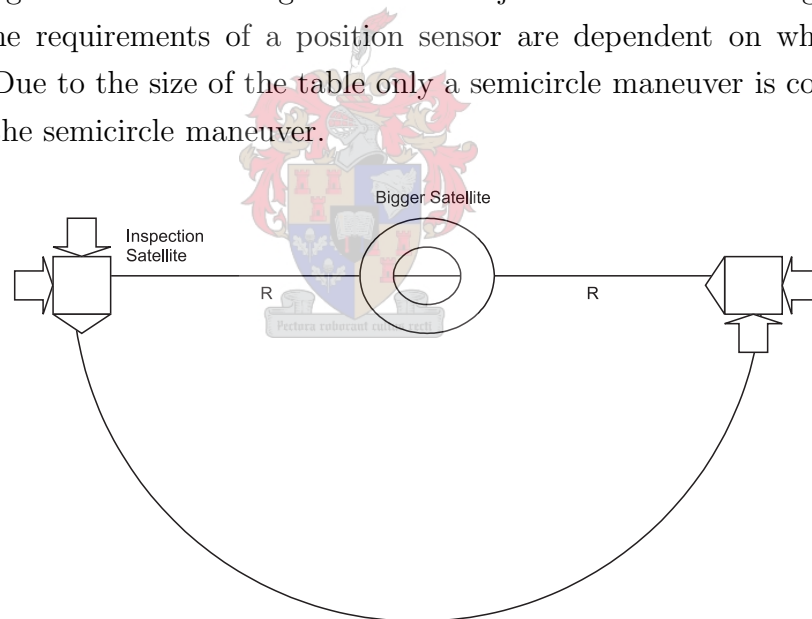


**Figure 3.1:** *Circular movement of Satellite*

A few strategies are investigated to complete the circular movement:

- **Circular thrust strategy**

For circular motion, the cart is rotated with a constant velocity with the thruster facing the middle of the circle. The thruster operates continuously on this maneuver as shown in Fig. 3.2.

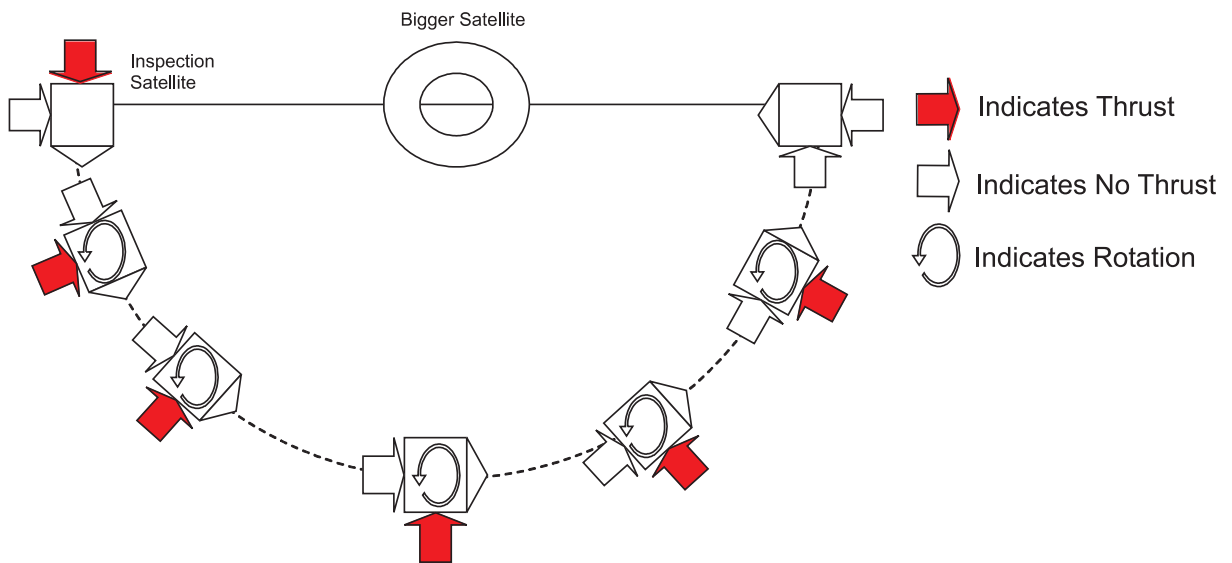


**Figure 3.2:** *Circular movement*

- **Circular segment thrust strategy, with X and Y components**

Another method for approximating a circular track is by splitting a segment in two X and Y components. This method however has its problems, due to the frictionless surface. The cart cannot stop and rotate in an infinitely short time.

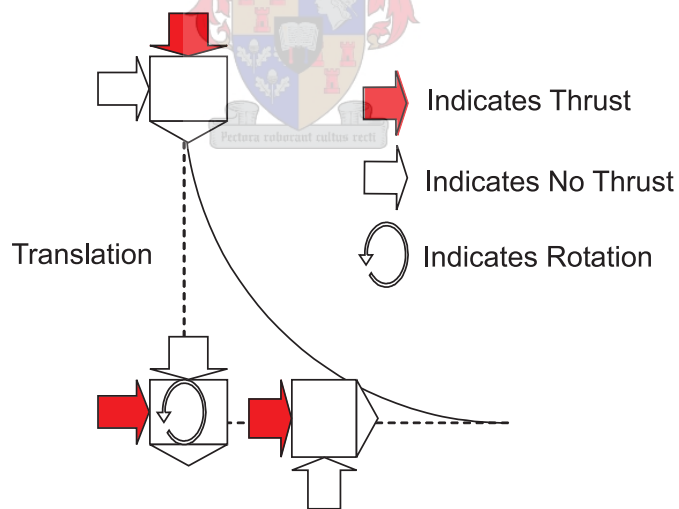


**Figure 3.3:** *Circular movement in segments*



- **Segmented thrust strategy**

Another strategy would be to approximate the circle with segments as illustrated in Fig. 3.4. An large number of segments will approximate a circle.

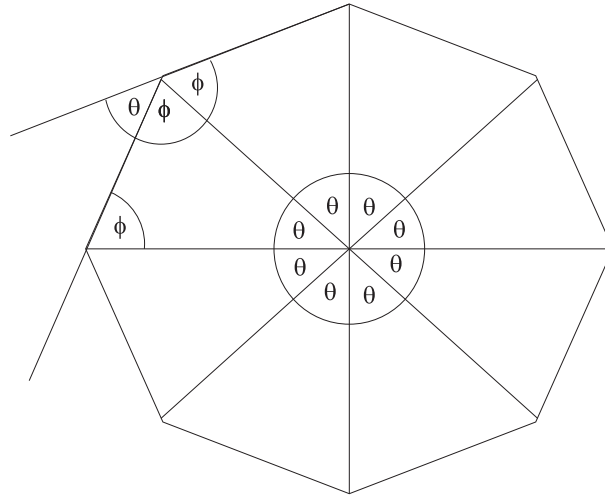


**Figure 3.4:** *Circle divided in segments*

The following equations are evident of an equilateral polygon (Fig. 3.4),

$$\theta = \frac{360}{N}, \quad N = \text{number of sides of a equilateral polygon} \quad (3.1)$$

$$\phi = \frac{180^\circ - \theta}{2} \quad (3.2)$$

The angle the cart rotates through on each segment is  $\theta^\circ$ . With  $N = 8$ ,  $\theta$  and  $\phi$  equals  $45^\circ$  and  $67.5^\circ$  respectively.

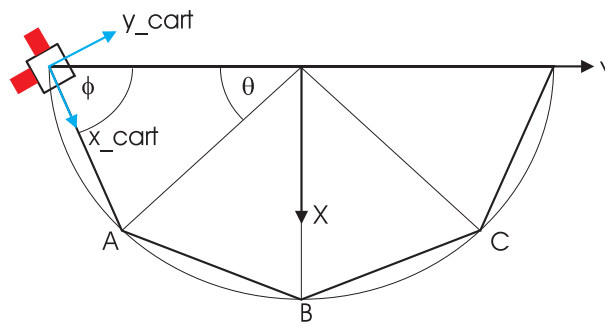


**Figure 3.5:** *4 segment illustration of movement*

The exact movement is as follows for a 4 segment semicircle: The cart starts off in the  $\phi$  direction. At points A, B and C the cart rotates and moves to the next segment.

### 3.1 Different Circular Strategy Options

The different strategies for maneuvering the cart around in a semicircle are simulated in Simulink. The Simulink simulation shown in Fig. 3.6 consists of the following:

- Equations of motion (1), from Eq. 2.14, 2.15 and 2.16.
- Axis transformation (Eq. 2.4, 2.5 and 2.7) and control strategy (2).
- Measurements and control outputs (3).

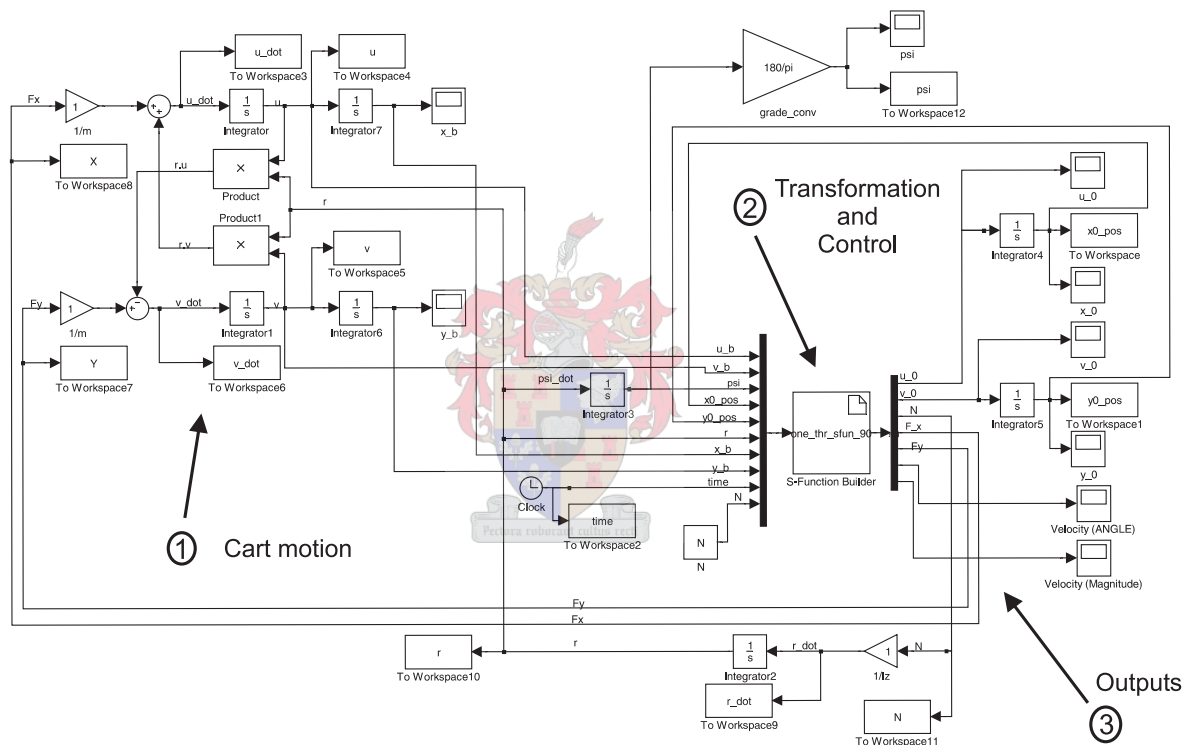
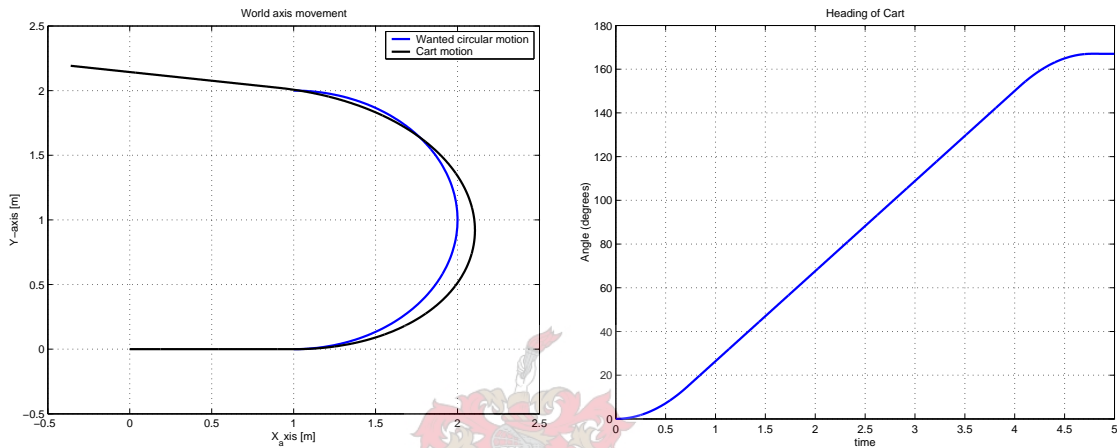


Figure 3.6: Simulink Model of Strategy

Simulation is done with unit values for power, radius, mass and inertia. The cart was given an initial velocity to ensure that the initial thrust is similar for all the evaluated strategies. Different strategies for circular motion are considered in the next sections.

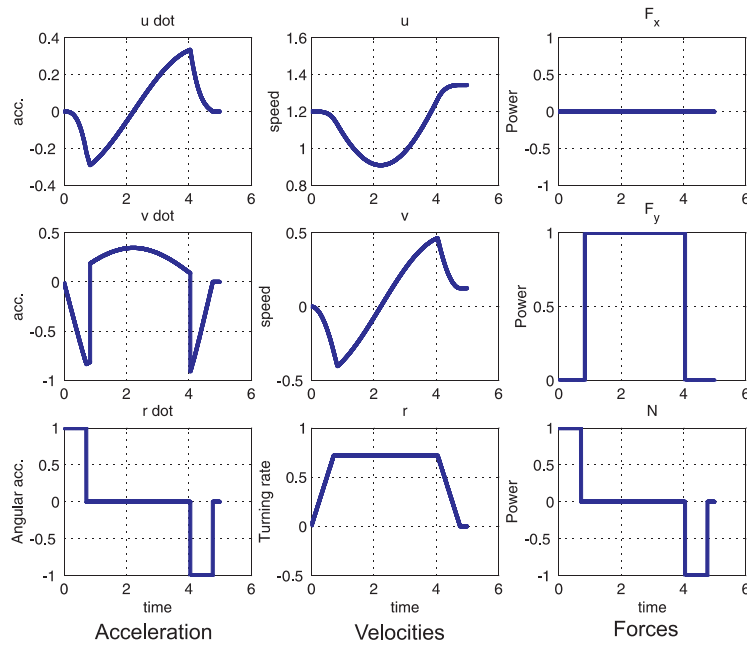
### 3.1.1 Circular

Continuous movement around a circle requires rotation with a constant angular velocity while thrusting continuously. This method causes the gas usage to be ineffective with a total thrust time of 3.2 sec. (Simulation in Matlab, see Fig. 3.8 [ $F_y$ ]). Simulation measurements of this maneuver are shown in Fig. 3.7 (left). The radius of the circle is a function of thrust and angular velocity. Stopping the cart at the end of the semicircle would involve a complex maneuver due to the build-up velocity.



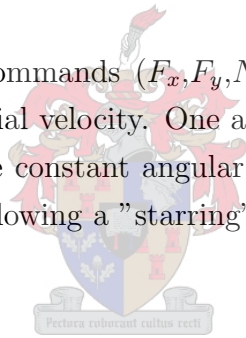
**Figure 3.7:** *Circular Motion*

Fig 3.7 (right) gives an indication of the angle of the cart. From this it is evident that the cart is rotated throughout the whole maneuver with a constant rate.



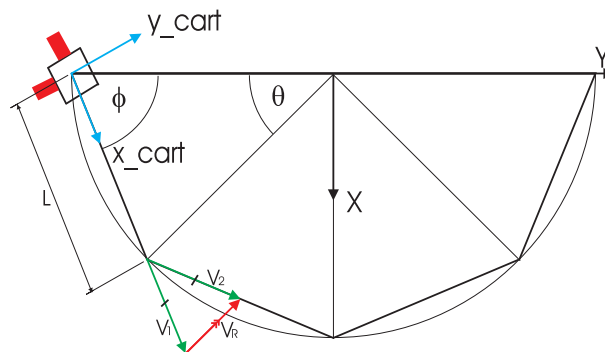
**Figure 3.8:** *Measurements of Circular motion*

Fig. 3.8 show the controller commands ( $F_x, F_y, N$ ), velocities ( $u, v, r$ ) and accelerations ( $\dot{u}, \dot{v}, \dot{r}$ ).  $u$  clearly shows the initial velocity. One advantage of this maneuver is the small field of view (FOV). Due to the constant angular velocity, the y axis of the cart always faces the object in the center allowing a "staring" imager to be used.



### 3.1.2 N-Segment

When the circular movement is approximated with segments, the cart must rotate a certain angle and then thrust for a certain time on each segment to translate to the next segment. To keep the cart at constant velocity, the angle and time that the thrusters are switched on for is critical. These values are calculated from Fig. 3.9 and 3.10.



**Figure 3.9:** *Resultant velocity vector*

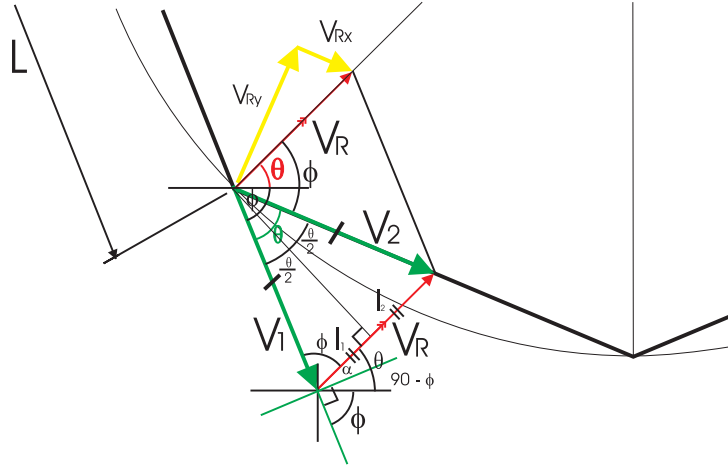


**Figure 3.10:** Resultant velocity vector (Fig. 3.9 [zoomed])

From Fig. 3.10 the following is evident,

$$\sin\left(\frac{\theta}{2}\right) = \frac{l_1}{|V_1|} \quad (3.3)$$

$$|V_R| = l_1 + l_2 = 2|V_1| \sin\left(\frac{\theta}{2}\right) \quad (3.4)$$

The velocity of the cart must be constant over all the segments. By applying a thrust in the direction of  $V_R$  the velocity vector will change from  $V_1$  to  $V_2$  ensuring translation to the next segment with constant velocity. On each segment, the cart must turn through  $\theta^\circ$  to face in the direction of  $V_R$ . The thrust needed for translation is discussed next with two different strategies:

### 1. Using the Y thruster

If only the Y thruster is used to move to the next segment the cart must first rotate in the direction of  $V_R$ . The angle the cart must rotate through on each segment is  $\theta^\circ$  for a N segment semicircle (Eq. 3.1). With the known angle of  $V_R$  the time the thruster is switched on for is calculated as:

$$a_y \times t_y = v_y = |V_R| \quad (3.5)$$

From Eq. 3.4,  $|V_R|$

$$t_y = \frac{2|V_1| \sin\left(\frac{\theta}{2}\right)}{a_y} \quad (3.6)$$

The analysis will be performed with unity values. If the strategy is implemented on the air bearing table,  $V_1$ ,  $\theta$  and  $a_y$  are known. In simulation the cart is initialized with starting angle  $\phi^\circ$  on the first segment and is therefore only rotated  $\frac{\theta^\circ}{2}$  on this segment. The X thruster is used to acquire the correct speed and coast forwards on

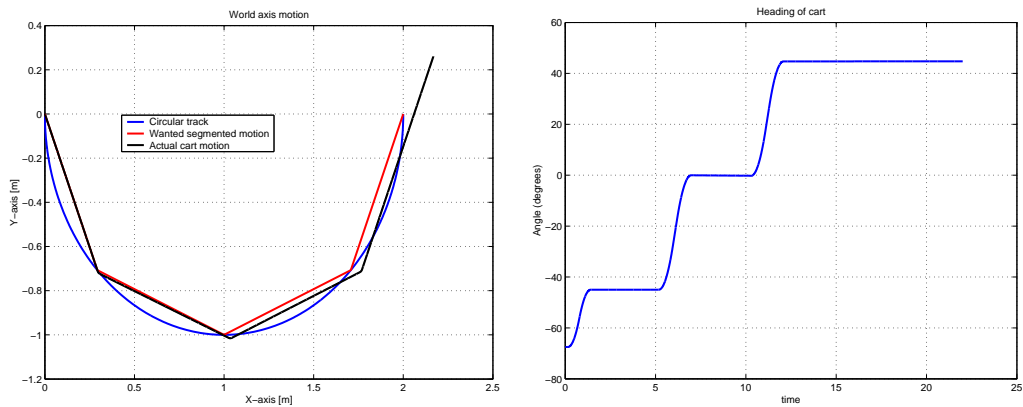


**Figure 3.11:** *Simulation of cart motion on the segments and heading of cart (Using Y thruster)*

the 1st segment. Just before the end of each segment, (1) the cart rotates through  $\theta^\circ$  to achieve the correct attitude for thrusting in the  $V_R$  direction and (2) the Y thruster is switched on for the time calculated in Eq. 3.6 to translate to the next segment as illustrated in Fig. 3.11 (left). In the simulation results in Fig. 3.11 (left) the thruster is switched on before the end of the segment to compensate for overshoot between the 1st and 2nd segment. This however is not done for the other segments. Fig. 3.11 (right) shows the heading angle changes of the cart.

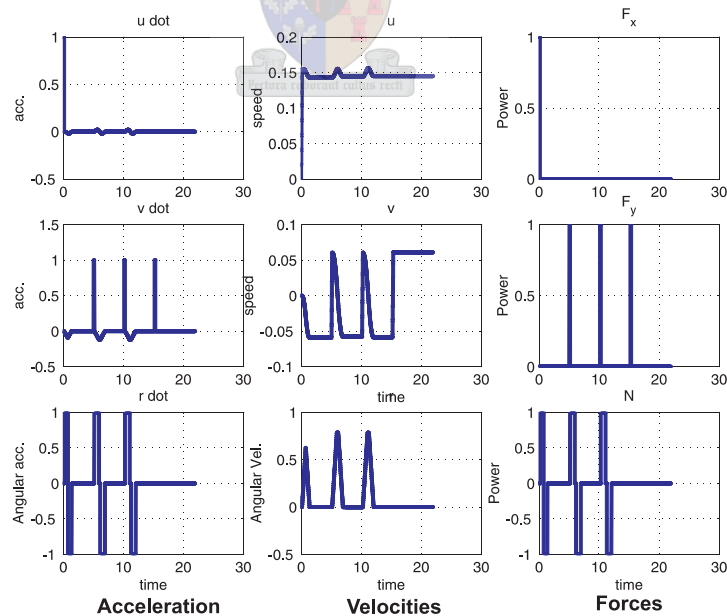


**Figure 3.12:** *Measurements of strategy simulation (Using Y thruster)*

Simulation data in Fig. 3.12 includes actuator forces  $F_x$ ,  $F_y$  and  $N$  and measurements of the velocity and acceleration in the x and y directions. Also included are the angular velocity and acceleration.

## 2. Using the X and Y thrusters simultaneously

Both thrusters (X and Y) are used to translate to the next segment. The cart is rotated on each segment by  $\theta^\circ$  during the thrust idle period. With a combination of thrust from the X and Y thrusters, the vector  $V_R$  (with X and Y components) is implemented for translation to the next segment (Fig. 3.10 (yellow lines)).

$$V_{Rx} = |V_R| \cos(\phi) \quad (3.7)$$

$$V_{Ry} = |V_R| \sin(\phi) \quad (3.8)$$

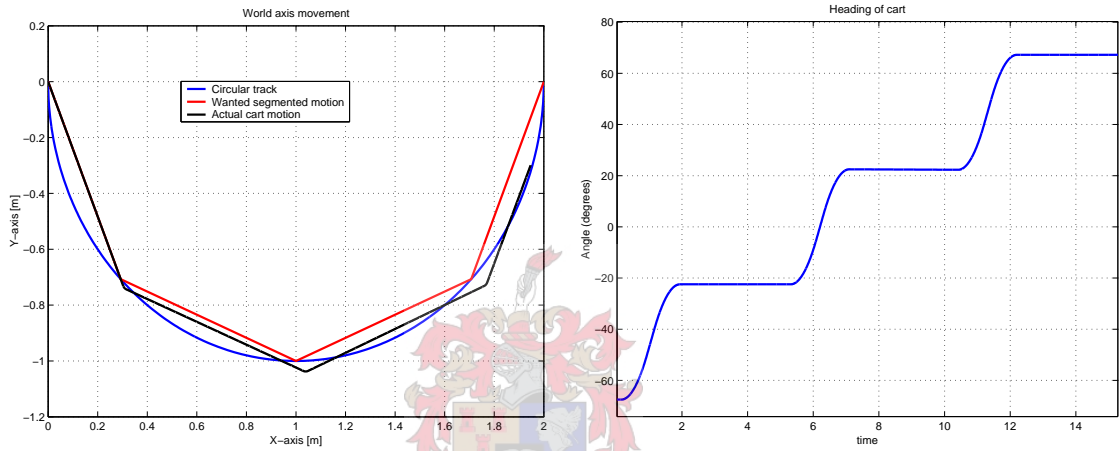


**Figure 3.13:** *Simulation of cart motion on the segments and heading of cart (Using X and Y thrusters)*

From Eq. 3.6, 3.7 and 3.8, the duration that the X and Y thrusters are switched on is given by:

$$t_x = \frac{2 |V_1| \sin(\frac{\theta}{2})}{a_x} \cos(\phi) \quad (3.9)$$

$$t_y = \frac{2 |V_1| \sin(\frac{\theta}{2})}{a_y} \sin(\phi) \quad (3.10)$$

The procedure for rotation and thrust on each segment is the same as in the previous section, the only difference being that the X and Y thrusters are used for translation between segments. The maneuver is shown in Fig. 3.13 (left). Data from the simulation include velocity and acceleration measurements ( $u, v, r, \dot{u}, \dot{v}, \dot{r}$ ) and control forces ( $F_X, F_Y, N$ ), see Fig. 3.14. Fig. 3.13 (right) shows the heading of the cart.

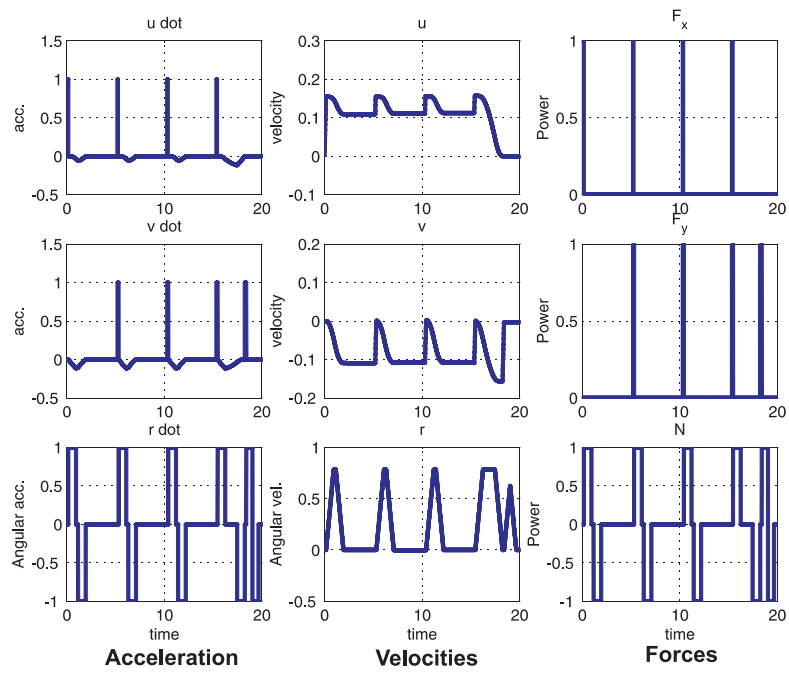
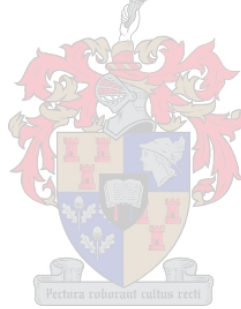


Figure 3.14: Measurements of strategy simulation (Using X and Y thrusters)





### Stopping on the last segment

The initial strategy was to maneuver continuously around another satellite/object. To conclude the segmented movement the cart can be stopped by rotating through  $112.5^\circ$  to oppose the velocity vector on the last segment and using the main thruster to stop. When the cart is stopped it rotates to face the object in the centre thus the heading becomes  $180^\circ$ . Fig. 3.15 (left) shows the cart maneuvered over 4 segments and stopped. See Fig. 3.15 (right) for the heading of the cart.

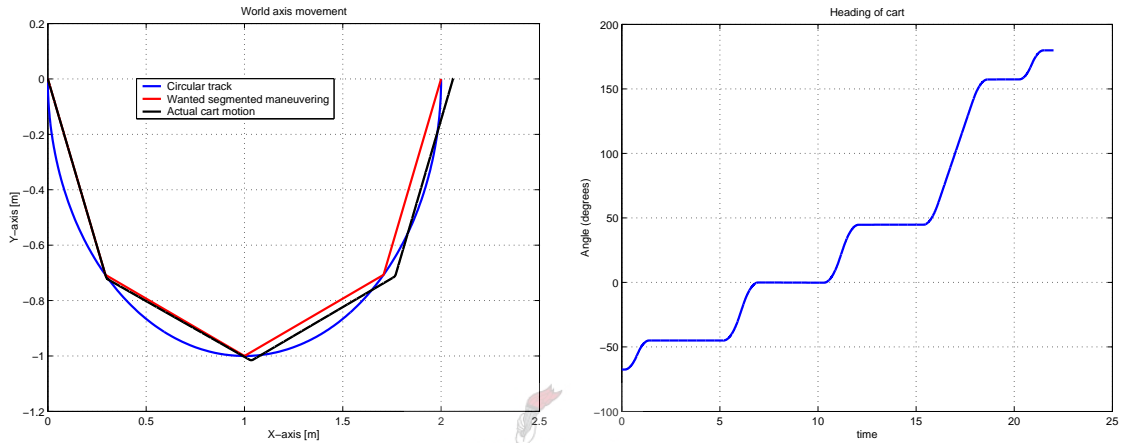


**Figure 3.15:** *Simulation of cart motion on the segments, cart stopped at end*

Simulation measurements and control commands are shown in Fig. 3.16.

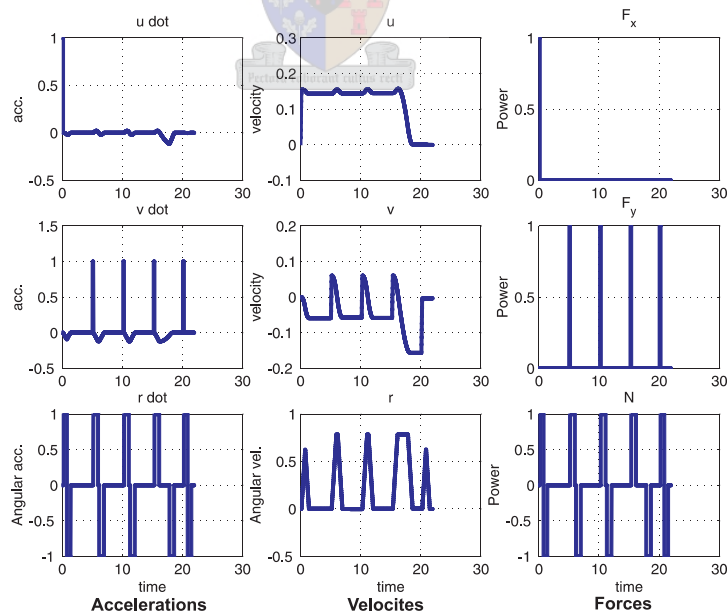


**Figure 3.16:** *Measurements of strategy simulation, cart was stopped at end*

The overshoot seen on all the segments can be compensated for. If the cart is rotated earlier in the direction of  $V_R$  the thruster can be switched on for translation to the next segment.

## 3.2 Results Analysis

### 3.2.1 Strategy

From simulation analysis it was evident that continuous thrusting (Section 3.1.1) is an ineffective method for circular motion. The rotate then thrust method (segment) is a more viable option due to less thrust time. Total thrust times for both segment cases examined (ie. translation with Y thruster and translation with X and Y thrusters simultaneously) are illustrated in Fig. 3.17 (These times include the initial starting thrust). The results are for 3-15 segments in a semicircle.

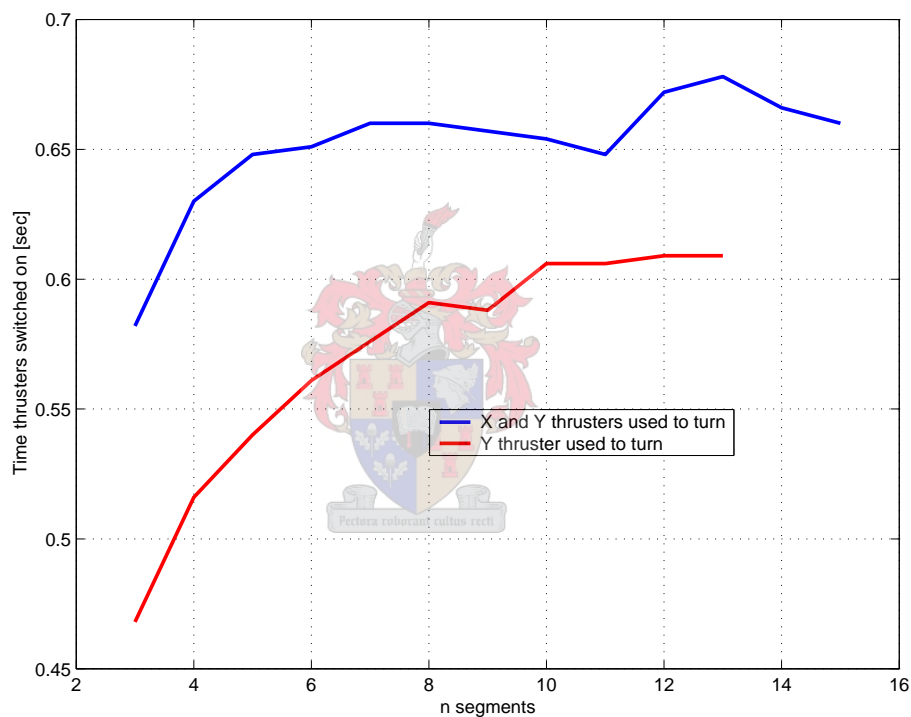


**Figure 3.17:** *Total time thrusters are activated*

From Fig. 3.17 it is evident that using the Y thruster to translate from one segment to the next was the best option. It uses much less gas and is therefore less expensive.

**How many segments must be used?**

Throughout the maneuver over the segments, the angle from the y-axis to the object increases and decreases. The number of segments affects the maximum deviation of this angle. Therefore by choosing the number of segments the position sensor angle width is also chosen. The sensor angle width is illustrated in Fig. 3.18 for 3 - 8 segments in a semicircle, from Appendix A.1.

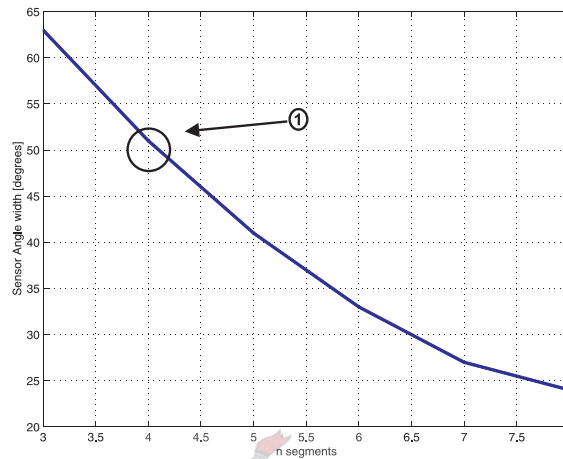


**Figure 3.18:** *Sensor Angle Width vs. N-segments*

The following conclusion was reached:

Firstly only the Y thruster is used to translate from one segment to the next because of its cost effectiveness. Secondly, a normalized value system is used as cost function to obtain a working number of segments as shown in Fig. 3.19 (1). For the remainder of this thesis 4 segments were used. This figure illustrates normalized thrust times and sensor angle widths for N segments.

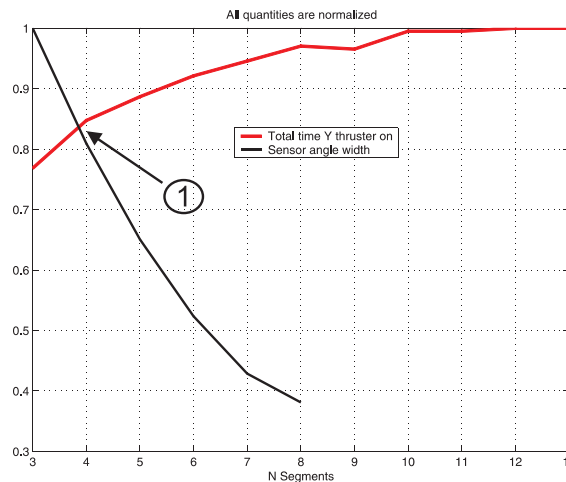


**Figure 3.19:** *Total thrust time and sensor angle width for a different number of segments*

### 3.2.2 System Requirements

The following sensors and actuators are necessary:

- **Actuators**

The cart is fitted with two thrusters mounted perpendicularly to each other to enable lateral movement (Fig 3.20). A momentum wheel is used for orientation control. If the inertias of the momentum wheel and cart are known, then a open loop angle controller could be used to rotate the cart, see Section 6.1.2. Another option is to implement an angle controller with the position sensor and momentum wheel used to rotate the cart.

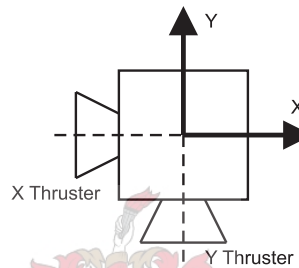


**Figure 3.20:** *Thruster topology*

- **Sensors**

A yaw rate gyro is already fitted on the cart. Additional sensors are needed with the following specifications:

Position Sensor

With 4 segments used to approximate a semicircle a sensor beam width of approximately  $50^\circ$  is needed (Fig. 3.18, (1)). The sensor must also be capable of detecting the distance to an object.

Accelerometer

A dual axis accelerometer is needed to measure the acceleration of the cart.

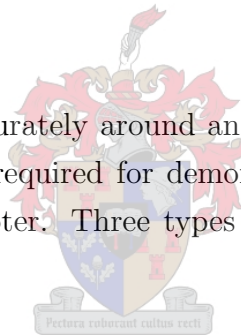
# Chapter 4

## Sensor and Actuator Development

### 4.1 Angle and Range Sensor

#### 4.1.1 Alternatives

To maneuver and orientate accurately around an object, another sensor to measure the relative position of the cart is required for demonstration purposes. The choice of this sensor is described in this chapter. Three types of sensors were considered: magnetic, optical and ultrasonic.



#### Optical position sensor

If an optical sensor such as a CCD camera is chosen the image must be visible. An optical camera is therefore not a viable option in space due to the darkness in eclipse, but can still be used in the air bearing table application to illustrate the principle. A PSD sensor requires an incident light to operate satisfactorily. Both these options require the inspection satellite to be fitted with some sort of light source.

The reflection from the sun on the satellite being inspected can also be used as a source of light. Tests were done on a solar cell to measure the amount of light reflected. A 20W halogen light bulb was placed in a tube to focus the light beams at the solar cell. The solar cell was mounted on a protractor which could be set to measure the various test angles. The reflected light was measured with a light meter (LUX units). Even when it was conducted in a dark room, this experiment was not successful as the reflected intensity was too low. This sensor option was ruled out for the air bearing table application.

Next, the same experiment was done but with the light replaced by solar illumination (measured at 111 000 LUX). Five measurements were done each with the light meter on the  $0^\circ$  axis. The protractor was then rotated from side to side in discrete steps of  $5^\circ$ . The results are in Fig. 4.1. To detect the reflected light some sort of light intensity detector

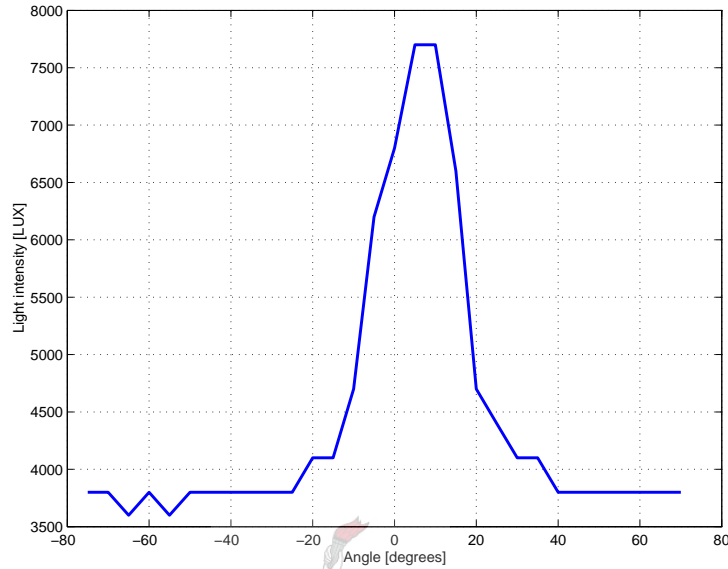


**Figure 4.1:** *Light reflection from Solar Cell*

is needed. The angle could then be retrieved by knowing the respective light intensities by fitting a cos or exponential function to the measured data. This is rather complex, and is not viable due to the lack of direct sunlight on the air bearing table. An absolute position sensor is necessary for position and distance measurement. This light intensity sensor will not provide a distance measurement and is thus not a viable option.

## Magnetometer

Attitude and orientation are measured relative to the earth's magnetic field. As a result of the earth's varying magnetic field the accuracy of the measurements can vary. The magnetometer will also not give a relative distance measurement to the object. The absence of a distance measurement as well as the cost of such a sensor, ruled it out as a viable option for position measurement.

Sensor	Price
Ultrasonic	R300 each
Magnetometer	R3000 each

**Table 4.1:** *Price Comparison*

## Ultrasonic position sensor

With two ultrasonic sensors and by means of stereoscopy it is possible to get the position of an object in front of the cart. This will give a range and angle measurement of the object. The ultrasonic sensors were used for position detection for the following reasons:

1. Low cost.
2. Fairly simple to implement.
3. It was a known device in the ESL.
4. Reliable.

The choice of position sensor cannot be implemented in space (satellite application) but is used to illustrate the concept on the air bearing table. The ultrasonic sensor can operate over a working distance of 0.2m to 10m. This is sufficient because the air bearing table is a mere 3.24m×1.87m and the maneuver is done with a circle radius of 1m. The sensor used is the Senscomp [6] 600 Series Smart Sensor (Instrument grade). The next sections describe the implementation of this sensor choice.

### 4.1.2 Beam Width

The sensors are being positioned at a certain distance and angle away from each other. Each sensors beam width is about 12° (from the datasheet [7]). The sensor beam pattern is shown in Fig. 4.2. With the use of an aperture mask it is possible to widen the beam angle. A position sensor beam angle of about 50° is needed. This value is taken from the previous simulation (Chapter 3.2.2).

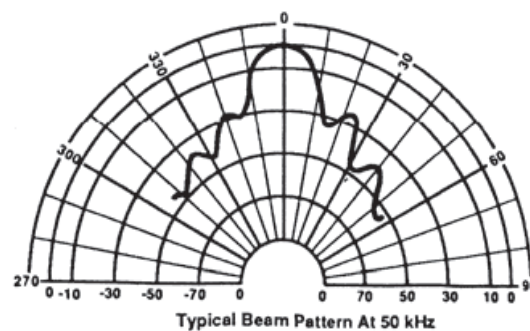


**Figure 4.2:** *Ultrasonic sensor beam width [6]*

The aperture mask is used to increase the beam angle. If the sensor is masked with a rectangular slit as wide as the transducer (horizontal), but only half as wide as the transducer (vertical), then the beam angle is 12 degrees horizontally and 24 degrees vertically. Thus by halving the aperture the beam angle is effectively doubled. The aperture has a radius of 38.74mm. The formula for slit thickness is as follows:

$$n = \frac{\text{Wanted Beam Angle}}{12^\circ} \quad (4.1)$$

$$l = \frac{38.74\text{mm}}{n} \quad (4.2)$$

Thus for a beam angle of 47°,  $n = 3.92$  and  $l = 9.89\text{mm}$ . The slit for the aperture was made 10mm wide.

Beam Angle [degrees]	n	l [mm]
40°	3.33	11.66
45°	3.75	10.33
50°	4.167	9.4
55°	4.58	8.54
60°	5	7.8
65°	5.42	7.3

Table 4.2: *Slit thickness*

The orthographic drawing and pictures of the aperture mask can be seen on Appendix B.1.

### 4.1.3 Obtaining Position

With the two sensors mounted a distance from each other and at a certain angle the two beam angles cross, see Fig. 4.5. If a target is within this area (gray area in Fig. 4.5) the position can be calculated. This must be kept in mind when evaluating this system. From the Fig. 4.3 and Appendix B.2 the position of these sensors is calculated:

$$\theta = -\frac{1}{2}(BA - BW) \quad (4.3)$$

If a Beam angle (BA) and a Beam width (BW) are chosen, the angle at which the sensors must be rotated is calculated.



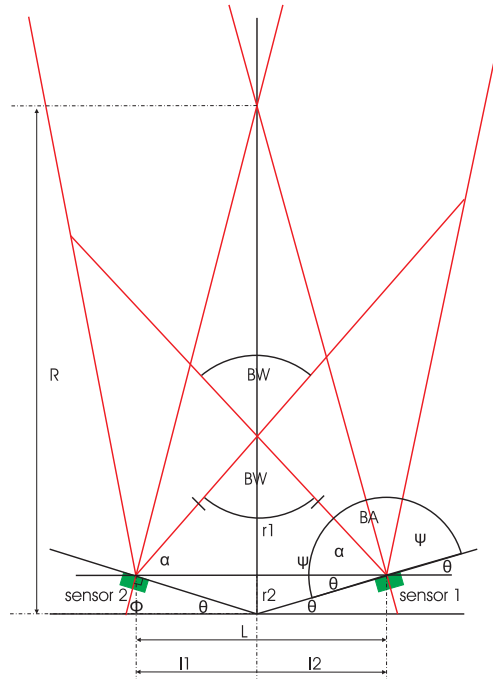


**Figure 4.3:** *Sensor position*

Also from Fig. 4.3 and Appendix B.2 the following is evident:

$$L = 2R \tan \theta \quad (4.4)$$

By calculating  $\theta$  (as mentioned above) and choosing the average distance to the object ( $R$ ),  $L$  (the distance between the sensors) is determined. The distance to the object ( $R$ ) is the distance perpendicular to the middle of the two sensors. At this point the signal is the strongest.

Fig. B.3 (Appendix B.3) gives an indication of how an object would be detected. The position of the detected target can be calculated as follows with  $L$  from above:

When a target is detected, the two distances  $D1$  and  $D2$  (Fig. 4.4) are measured from the ultrasonic sensors. Using geometry, the target distance and angle can be calculated. Now the following equations will illustrate how position is calculated (from Appendix B.3) with these measurements:

$$D^2 = D1^2 + \left(\frac{L}{2}\right)^2 - 2 D1 \frac{L}{2} \cos(c) \quad [\text{Distance to object, } L \text{ is known}] \quad (4.5)$$

$$\rho = \cos^{-1}\left(\frac{D1^2 - D^2 - \left(\frac{L}{2}\right)^2}{-2D\frac{L}{2}}\right) \quad [\text{Angle to object, } L \text{ is known}] \quad (4.6)$$

A beam width (BW) of about  $61^\circ$  is chosen instead of  $50^\circ$  (Chapter 3.2.2). The reason for choosing  $61^\circ$  is to leave margin for error. From this the beam angle (BA) of  $47^\circ$  for each

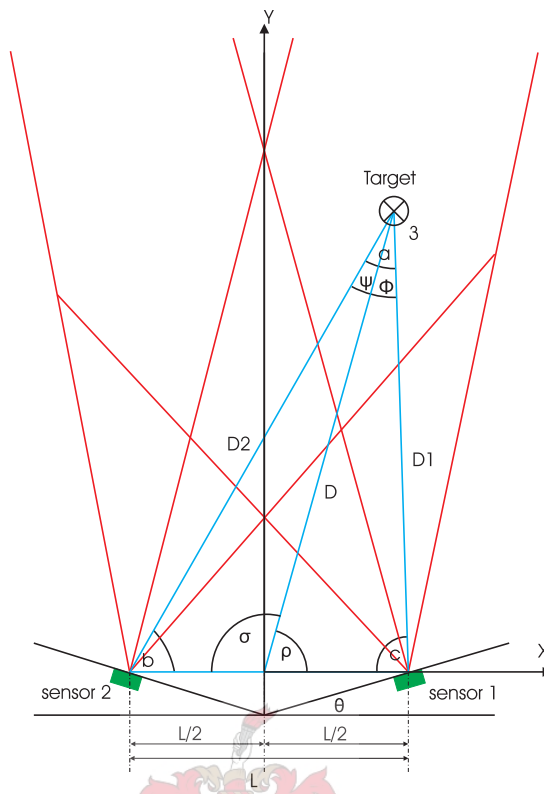


Figure 4.4: *Position calculation*

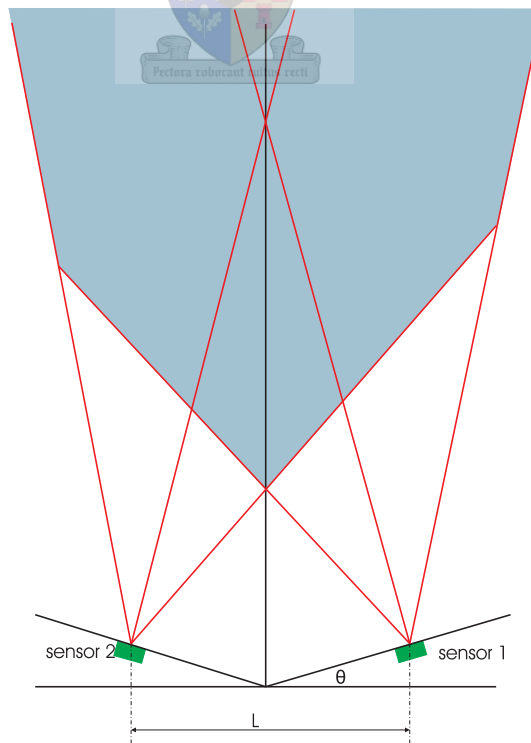
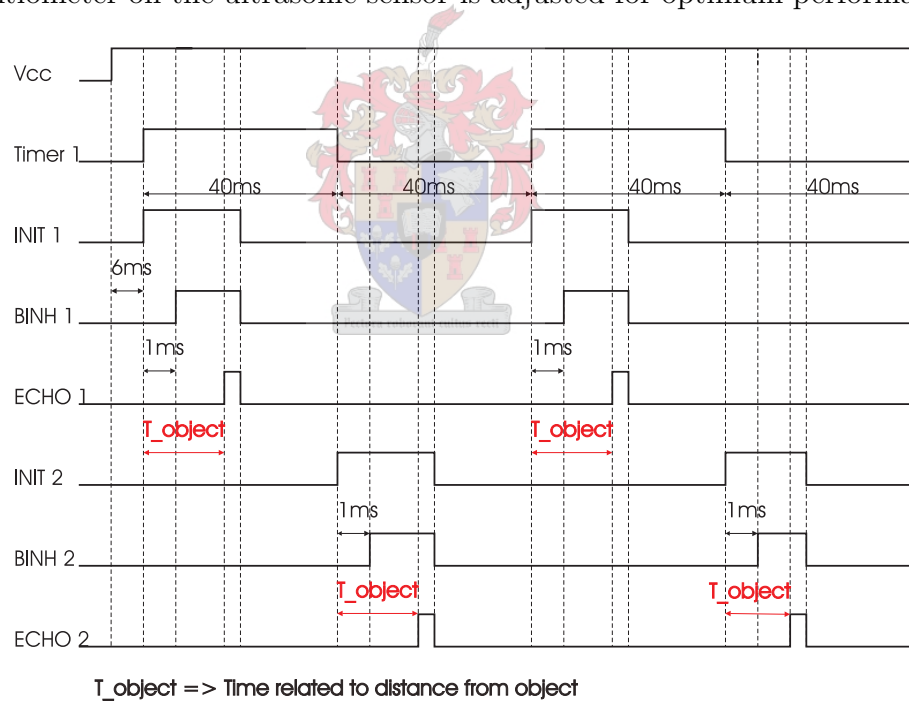


Figure 4.5: *Beam angle crossing*

sensor is sufficient. This gives an aperture mask slit of 9.89mm and  $\theta = 7^\circ$ . Choosing  $R$  equal to 1.15m, the distance where the object will be observed, ( $L$ ) is calculated as 28.24cm. Thus the sensors will be positioned at a  $7^\circ$  angle with a distance of 28.24cm between them.

#### 4.1.4 Implementation

The ultrasonic sensor is driven in single echo mode because only one target is being detected. When the INIT line of the sensor is taken high, the ultrasonic sensor gives a pulse. When this pulse returns, the ECHO line is driven high. The sound is traveling at about 3 msec/m and by measuring the time it takes the pulse to travel to the object and back the distance is calculated. The ultrasonic sensors are pulsed independently on each Timer1 interrupt of the microprocessor. Timer1 runs on a 40ms interrupt, therefore a complete position calculation is given after 80ms. Fig. 4.6 illustrates this concept. The gain potentiometer on the ultrasonic sensor is adjusted for optimum performance at 1m.



**Figure 4.6:** *Timing diagram of ultrasonic sensors*

Because the microprocessor only detects falling edge interrupts, the ECHO signal was inverted (details in Appendix B.4). The flow chart of this program is shown in Appendix B.5. Fig. 4.7 illustrates the results of the position sensor. An object was placed in front of the sensor with a distance of 1m and angle  $22^\circ$ .

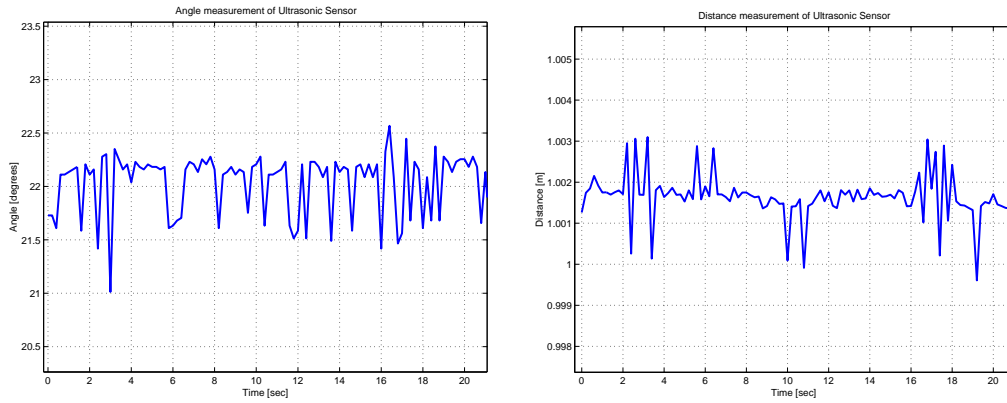


**Figure 4.7:** Angle and Distance measurement of Ultrasonic sensors

## 4.2 Momentum Wheel

The momentum wheel hardware consists of a DC motor [Maxon DC motor (RE 25), 145342] fitted with a reaction wheel obtained from Sunspace [37]. The inertia of the wheel is  $1,5 \times 10^{-3} kg m^2$ . The driving circuit PCB for the DC motor was provided. This circuit included 4 Mosfets in an H-bridge configuration. To make the motor rotate in one direction Q1 was switched on and a PWM signal was applied to Q4. For the motor to turn in the other direction the same is true for Q2 and Q4 respectively, see Fig. 4.8

State	Q1	Q2	Q3	Q4
Stop Motor	1	1	0	0
Direction 1 from Fig. 4.8 red line	0	1	0	PWM
Direction 2 from Fig. 4.8 light blue line	1	0	PWM	0

**Table 4.3:** Mosfet states

The PWM is modelled as a gain. Thus the input to the current loop, voltage  $V_t$  (Eq. 4.7) is duty cycle times the supply voltage,  $V_{cc}$ . The model of the DC motor in Fig. 4.9 is from Eq. (C.1), (C.2), (C.3) and (C.4). The constants in Fig. 4.9 are defined in Appendix C.

### 4.2.1 Current Loop

From Eq. C.5, the plant of the current loop is:

$$G(s) = \frac{I_a}{V_t} = \frac{1}{R_a + sL_a} \quad (4.7)$$

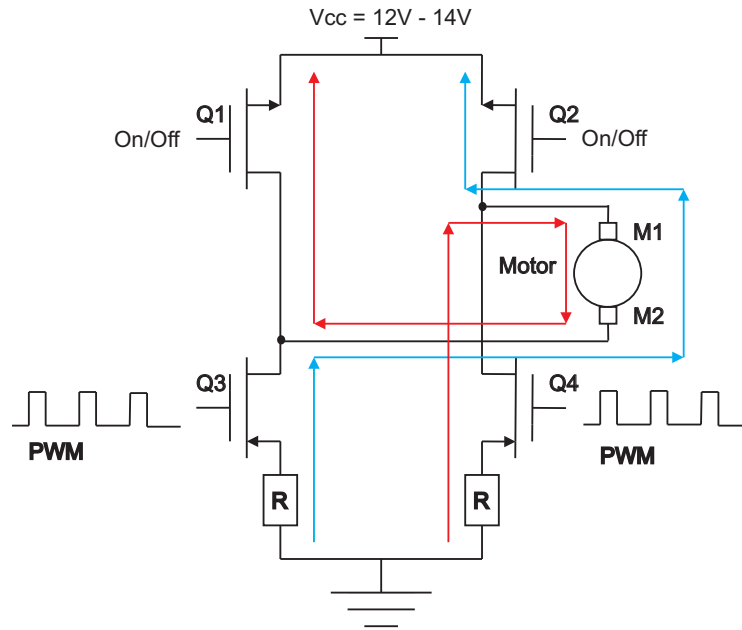


**Figure 4.8:** Driving circuit for the Momentum Wheel from Fig. C.2, Fig. C.3 and Fig. C.4

Using this plant, a PI controller is designed. The proportional term was used to decrease response time but with minimum overshoot. The integrator is used to ensure zero steady state error. The controller was designed as:

$$D(s) = 0.6 \frac{s + 388.5}{s} \tag{4.8}$$

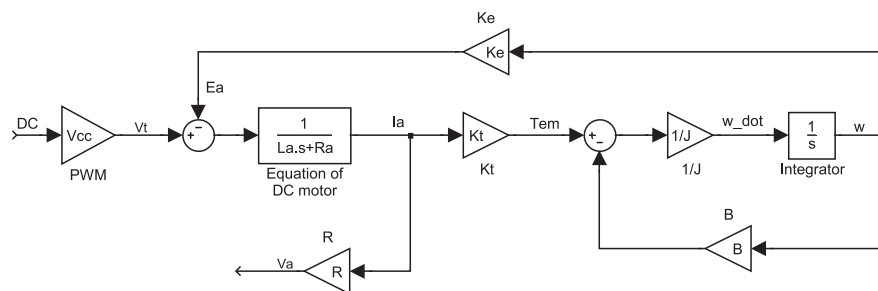


**Figure 4.9:** DC Motor Block Diagram

The sampling time of the system was chosen as a multiple of the PWM period at 360Hz (Appendix D.1). The current through the motor was measured over R as  $V_a$  (see Fig. 4.10). The current measurement is filtered with a low pass filter at 159Hz. This also acts as an anti-aliasing filter.

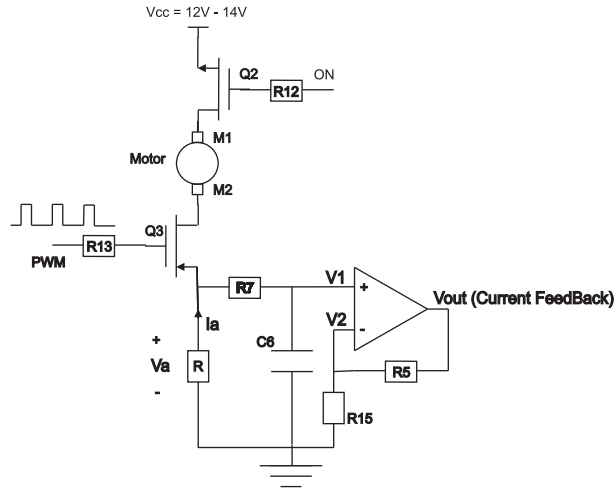


**Figure 4.10:** One leg of the H-bridge driving the DC Motor (From Fig. 4.8)

The closed loop current controller is shown in Fig. 4.11. The current in Ampere to current in ticks conversion constant included in this figure is calculated in Appendix D.2.

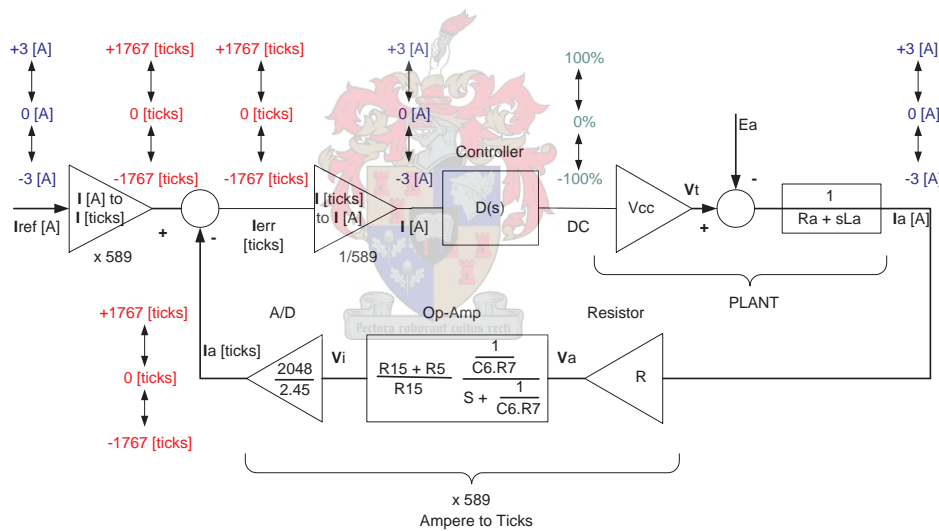


**Figure 4.11:** Current Loop Block Diagram with scaling factors

The controller difference equation was implemented at 360Hz. The controller was designed to give duty cycle percentage as output. The microcontroller however changes a 8 bit register in order to change the duty cycle. Thus 0-100% is given by setting 0 - 255 bits, where 255 is 0% and 0 is 100% duty cycle. The output of the controller is multiplied by 256 which is then used to change the corresponding register. The implemented discrete controller derivation is shown in Appendix D.3.

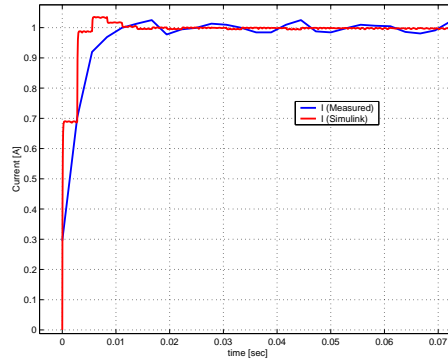


Figure 4.12: Current Loop Step response

The step response of the current loop is shown in Fig. 4.12. A closed loop plant bandwidth of 94.9Hz is achieved. The overshoot is almost zero and the settling time is 10 msec. After simulation, it was clear that there was a gain difference between the simulated system and the physical system due to modelling inaccuracies. The simulated plant was multiplied by 0.55.

### 4.2.2 Velocity Loop

From Fig. 4.9 and 4.11 the velocity loop is modelled.  $E_a$  is taken as a disturbance. B is considered small enough and omitted.

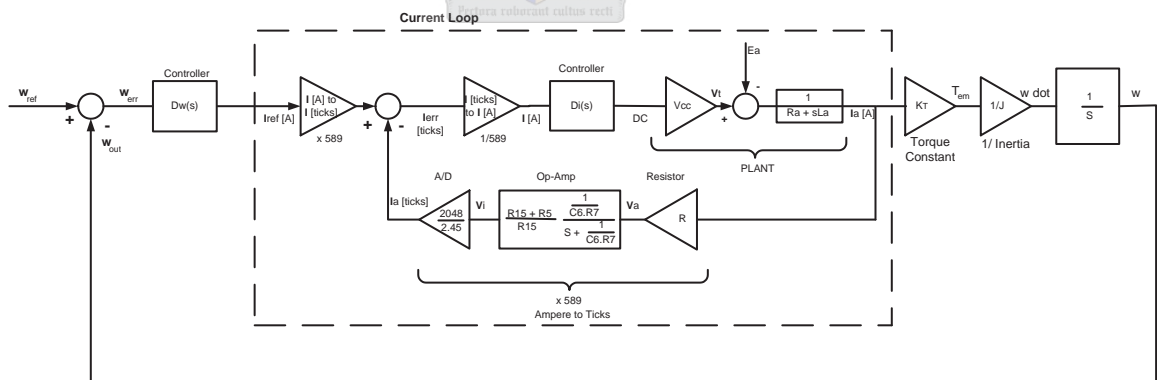


Figure 4.13: Velocity Loop Block diagram

The closed loop current plant  $G_I(s)$  has a bandwidth of 94.9Hz. The outside velocity loop will be closed at 10Hz, almost 10 times slower than the inner current loop. For this reason the dynamics of the current loop can be ignored and the plant of the speed controller is

modelled as:

$$G_{\omega}(s) = \frac{K_t}{J} \frac{1}{s} \quad (4.9)$$

with  $K_t$  and  $J$  as given in Appendix C. The speed loop simplifies to Fig. 4.14.

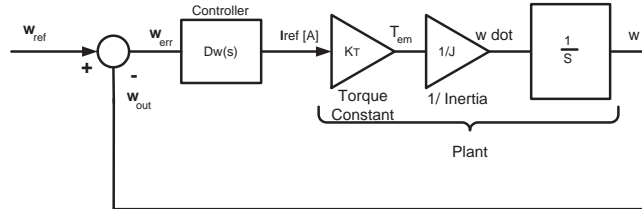


**Figure 4.14:** Simplified velocity controller block diagram

A PI controller was chosen for the same reasons as those stated in Section 4.2.1. The proportional term was used to decrease response time but with minimum overshoot and the integrator term is used to ensure zero steady state error. The controller is designed with  $K_p = 2$  and  $K_i = 0.001$ .

$$D(s) = 2 \frac{s + 0.001}{s} \quad (4.10)$$

When the PWM is switched on, the velocity measurement becomes very noisy. To suppress these high frequency components a low pass filter is added to the controller to ensure roll-off at higher frequencies. The transmission function is therefore suppressed at higher frequencies and the system is made more stable and robust. The filter added is as follow:

$$F(s) = \frac{150}{s + 150} \quad (4.11)$$

The filter has a bandwidth of 24Hz and unity gain. The total velocity controller consists of  $D(s) \times F(s)$ .

$$\text{Controller} = D(s)F(s) = \frac{300s + 0.3}{s^2 + 150s} \quad (4.12)$$

The discrete controller can be found in Appendix E.1.

To prevent controller saturation (due to limited dynamic response) a slew rate limiter is implemented as a pre-filter. The rate is limited at  $74 \text{ rad/s}^2$ . This value is calculated in Appendix E.4. The input current to the current loop controller in the case of the velocity controller is limited to  $\pm 3 \text{ A}$  ( $\pm 1767$  ticks).



The tachometer [36] of the DC motor gives a voltage proportional to the RPM of 0.52V per 1000RPM. The Wheatstone bridge in Fig. 4.15 is used to measure the signed velocity. These two voltages VELFBA and VELFBB (Fig. 4.15) are filtered with a 100Hz low pass Butterworth filter [Appendix E.3].

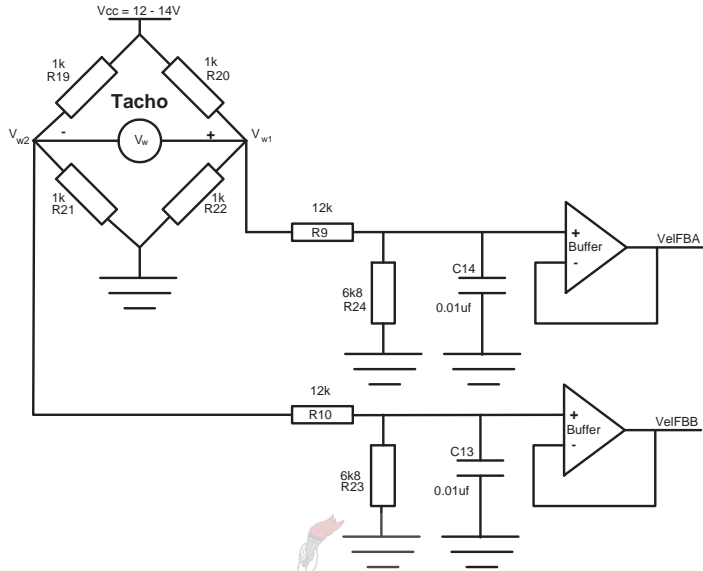


Figure 4.15: Tacho velocity measurement from Fig. C.2, Fig. C.3 and Fig. C.4

The simulation of the speed controller is done in Simulink with the closed loop current plant included. This is done to investigate the effect of it being omitted for design purposes. The simulation worked well with the current loop included. The plant gain of the velocity loop is multiplied with 2.3 to compensate for modeling inaccuracies.

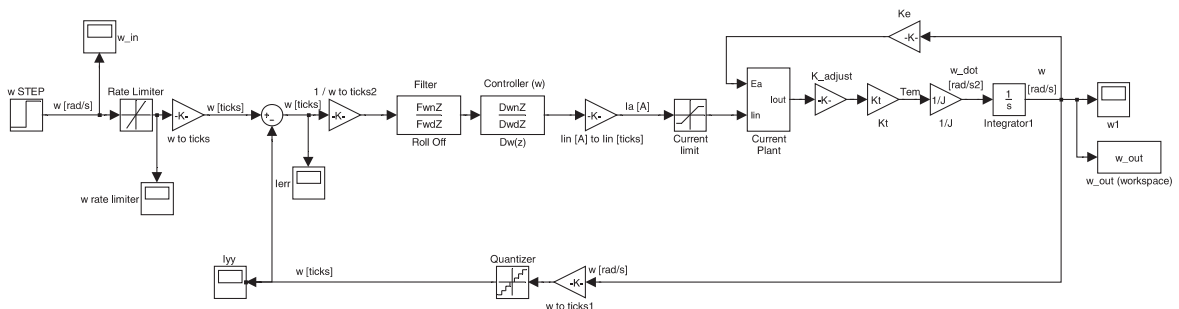


Figure 4.16: Simulink model of velocity controller

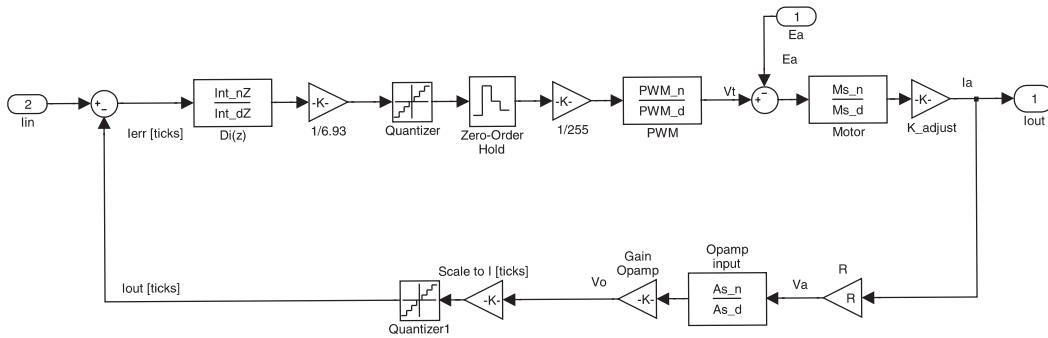


Figure 4.17: Simulink model of current loop in velocity controller [Fig. 4.16]

From Fig. 4.18 it is evident that the settling time for the speed controller is 1.5 sec. for a step of 1000 RPM. There is also no overshoot due to the pre-filter. The two measurements (current and velocity) are read in by the A/D Converter at 360Hz (the same frequency the controllers are implemented). At each sample time the velocity controller calculates the exact value for the reference to the current loop. Once calculated it is passed to the current loop which in turn drives the current loop.

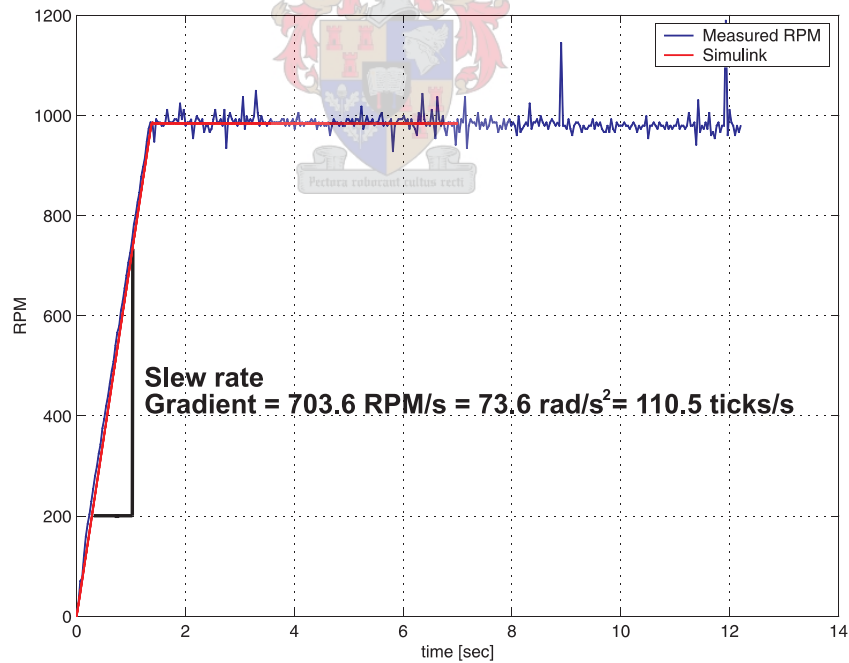
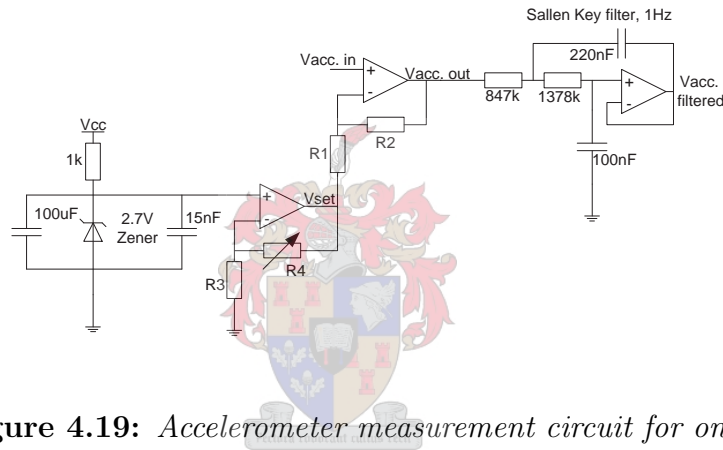


Figure 4.18: Step response of the Velocity Controller

### 4.3 Accelerometer

To move the cart on the air bearing table, the thrusters are used. To measure the acceleration on the x and y axis, a  $\pm 2g$  Dual-Axis Accelerometer [10] is used. The bandwidth of the accelerometer is set to 10Hz. With a supply voltage of 5V, the sensor gives an output of 300mV/g. Acceleration measurements on the air bearing table are in the order of 4-5mg. With this in mind, the signal is amplified by a factor of 11 for better resolution. The accelerometer measurement is integrated for velocity measurement and a low pass filter was therefore included at 1Hz to limit noise levels. Fig. 4.19 illustrates a complete circuit diagram of the accelerometer measurement. The nominal voltage of the accelerometer is in the order of 2.5V. With a gain of 11 the A/D converter and op-amps are saturated, so an offset is needed.



**Figure 4.19:** Accelerometer measurement circuit for one axis

From Fig. 4.19 the offset and gain of the accelerometer measurement:

$$V_{acc. out} = \left(1 + \frac{R2}{R1}\right)V_{acc. in} - \frac{R2}{R1}V_{acc. set} \quad (4.13)$$

$V_{set}$  is adjusted with R4 (Fig. 4.19). The opamps used are OPA2340 [11]. They were chosen for their low output voltage offset which was necessary for accurate measurements. The accelerometer is placed in the center of mass of the cart, with the two axis aligned with the two thrust directions.

# Chapter 5

## Implementation of Strategy

In this chapter additional controllers and a filter is designed to implement the strategy from Section 3.1.2 on the air bearing table. The sensors and actuator developed in Chapter 4 are used for this purpose. The angular velocity and angle control for the cart will be implemented by using the momentum wheel as the actuator. The developed sensors will be integrated with the angle controller and EKF designed.

### 5.1 Angular Velocity Control

#### 5.1.1 Simulation



The closed loop plant of the momentum wheel velocity controller in Chapter 4.2.2 is:

$$G_{\omega_{CL}}(s) = \frac{7498(s + 0.001)}{(s + 75 + 43.3j)(s + 75 - 43.3j)(s + 0.001)} \quad (5.1)$$

By ignoring the slow zero/pole combination for simplicity and adding the inertial ratio between the cart and the momentum wheel, the angular velocity plant of the cart is:

$$G_{\omega_{CL}}(s) = \frac{-14.39}{(s + 75 + 43.3j)(s + 75 - 43.3j)} \quad (5.2)$$

The inertial ratio included from Eq. F.4 (Appendix F.1) is (Fig. 5.1):

$$\omega_{cart} = -\frac{I_{MW}}{I_{cart}} \omega_{MW} \quad (5.3)$$

A PI controller is designed. The proportional term is used to give fast response times to step inputs and the integral term is used to eliminate steady state error.

$$D_{\omega(cart)}(s) = -40 \frac{s + 9.5}{s} \quad (5.4)$$

Appendix F.2 discusses the discrete controller implemented at 360Hz with the  $\omega[rad/s]$  to  $\omega[ticks]$  conversion constant included.

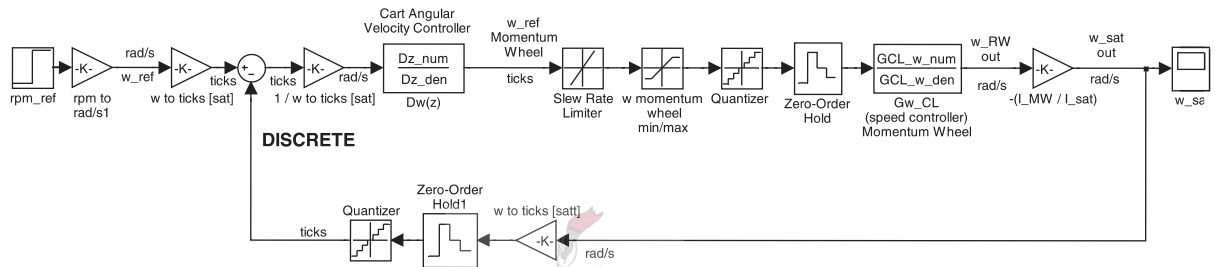


**Figure 5.1:** *Simulink model of Angular Velocity Plant*

The momentum wheel and cart inertias are  $1, 5 \times 10^{-3} \text{ kg.m}^2$  and  $0.782265 \text{ kg.m}^2$  respectively (Appendix F.4). The constant used to convert  $\omega[rad/s]$  (gyro measurement) of the cart to  $\omega[ticks]$  is 605 (Appendix F.3). Thus the A/D converter assigns a value of 605 [ticks] for each rad/s. The gyro is integrated with a 40Hz low pass filter, which also acts as an anti-aliasing filter. No further filtering is therefore needed. The sampling frequency of the gyro signal is 360Hz.

### 5.1.2 Results

The Bode plot in Fig. 5.2 shows a bandwidth of 0.1Hz for the closed loop angular velocity controller of the cart. The design requirements of the controller include a fast settling time with no overshoot. The reason for this is that the angle controller will use this controller and no ringing is wanted during the tracking of an object.

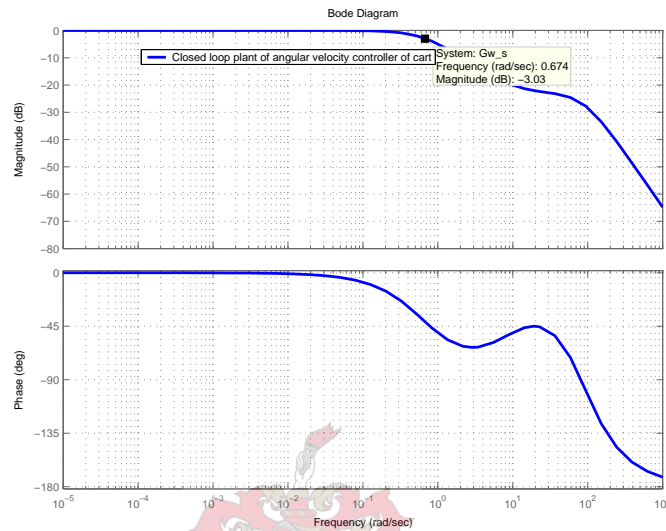


Figure 5.2: Bode plot of closed loop plant.

From Fig. 5.3 it is clear that a settling time of 4 sec. is achieved with no overshoot. The gyro is sampled at 360Hz the same frequency the controller is implemented. The control signal drives the momentum wheel velocity controller. The controller output is limited to  $\pm 3000$  RPM to prevent windup of the integrator.

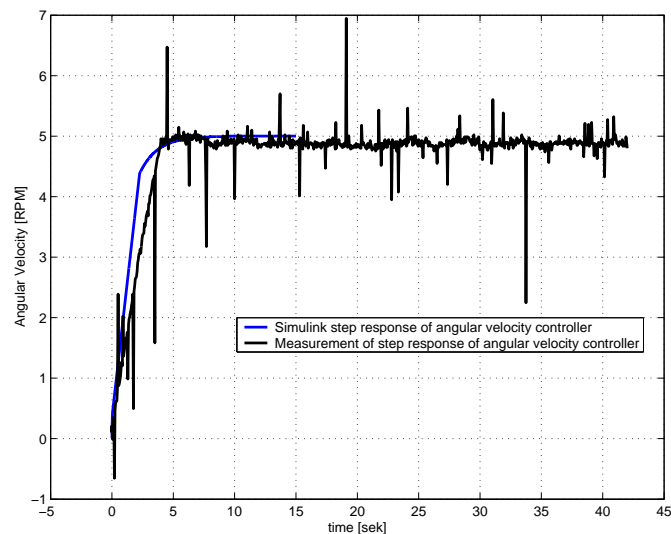


Figure 5.3: Step response of cart angular velocity controller

## 5.2 Angle Control

### 5.2.1 Simulation

The simplified closed loop plant of the angular velocity controller of the cart (Appendix F.5) is:

$$G_{\omega(cart)} = \frac{0.6858}{s + 0.6858} \quad (5.5)$$

The plant includes an integrator to convert rad/s to radians:

$$G_{\theta(cart)} = \frac{0.6858}{s^2 + 0.6858s} \quad (5.6)$$

For a fast response with little overshoot a proportional controller is used.

$$D_{\theta(cart)} = 0.3 \quad (5.7)$$

The angle of the cart is measured with the ultrasonic sensors and can be calculated using Eq. 4.6, but this is complex. An alternative option is to subtract the two measured distances and multiply it with a constant (Appendix F.6). This constant together with a constant to convert  $\omega$ [rad/s] to  $\omega$ [ticks] (Appendix F.3) is included in the controller implemented:

$$D_{\theta(cart)}(z) = -0.07248 \quad (5.8)$$

The Simulink model is shown in Fig. 5.4.

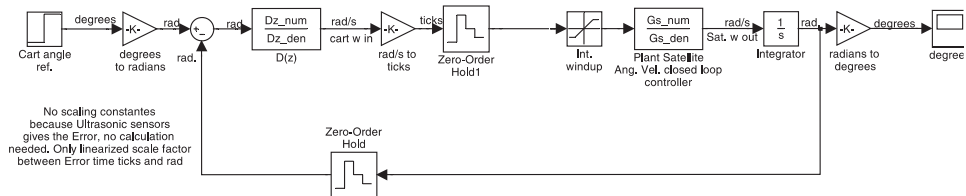


**Figure 5.4:** Angular controller Simulink model

The gyro gives a positive angle in the clockwise direction and  $D1 - D2$  gives a negative angle in the same direction (from Fig. F.5). Therefore the negative sign was used in the controller.

## 5.2.2 Results

The bode plot in Fig. 5.5 shows the closed loop plant with bandwidth of 0.07Hz and dominant first-order roll-off. The bandwidth is constrained by the slow pole from the angular velocity controller, Eq F.7.

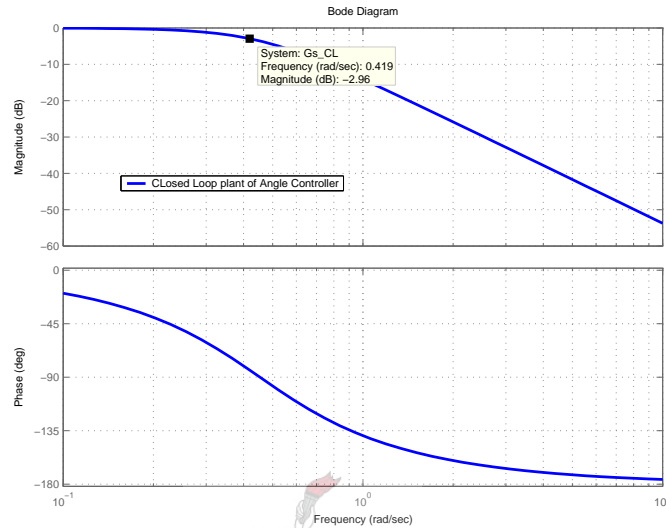


**Figure 5.5:** *Bode plot of closed loop Angle controller*

From Fig. 5.6 it is clear that a settling time of 10 sec. is achieved. The overshoot is less than 5%. The angle controller is implemented on the microprocessor at a frequency of 12.5Hz (80 msec.) so as to coincide with the new ultrasonic measurements that are available to calculate the angle. The control signal from the angle controller is limited to  $\pm 5$  RPM to prevent windup in the system.

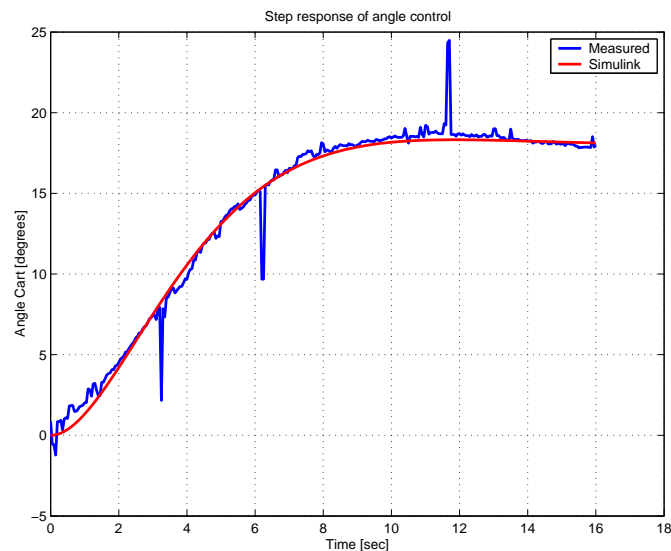


**Figure 5.6:** *Step response of cart angle control*



## 5.3 Extended Kalman Filter [EKF]

An Extended Kalman Filter (EKF) is implemented to estimate the position, velocity, angle and angular velocity states from the non-linear dynamic equations. These states are then used to implement the non-linear control for the maneuver and orientation strategy discussed in Chapter 3.

### 5.3.1 Simulation of the EKF

The dynamic equations in 2.14, 2.15, 2.16 and 2.17 are used:

$$\underline{f}(\underline{x}, t) = \begin{bmatrix} u \\ \dot{u} \\ v \\ \dot{v} \\ r \\ \dot{r} \end{bmatrix} = \begin{bmatrix} u \\ rv \\ v \\ -ur \\ r \\ 0 \end{bmatrix} + \begin{bmatrix} 0 \\ \frac{F_x}{m} \\ 0 \\ \frac{F_y}{m} \\ 0 \\ \frac{N}{I_z} \end{bmatrix}$$

With this in mind, and from Appendix G.1,  $F_{dk}$  is calculated for the EKF gain equations (Eq. 2.26, 2.27 and 2.28),

$$F_{dk} = \begin{bmatrix} 1 & T_s & 0 & 0 & 0 & 0 \\ 0 & 1 & 0 & rT_s & 0 & vT_s \\ 0 & 0 & 1 & T_s & 0 & 0 \\ 0 & -rT_s & 0 & 1 & 0 & -uT_s \\ 0 & 0 & 0 & 0 & 1 & T_s \\ 0 & 0 & 0 & 0 & 0 & 1 \end{bmatrix} \quad (5.9)$$

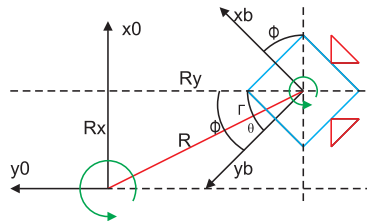


Figure 5.7: EKF measurements

From Fig. 5.7 the measurement equations are calculated as,

$$h(\underline{x}, t) = \begin{bmatrix} R \\ \theta \end{bmatrix} = \begin{bmatrix} \sqrt{x^2 + y^2} \\ \phi - \tan^{-1}\left(\frac{x}{-y}\right) \end{bmatrix} \quad (5.10)$$

From Eq. 2.23 and 5.10,  $H_k$  is calculated:

$$H_k = \begin{bmatrix} x(x^2 + y^2)^{-\frac{1}{2}} & 0 & y(x^2 + y^2)^{-\frac{1}{2}} & 0 & 0 & 0 \\ \frac{1}{y} \left[ \frac{1}{1 + \frac{x^2}{y}} \right] & 0 & \frac{-x}{y^2 + x^2} & 0 & 1 & 0 \end{bmatrix} \quad (5.11)$$

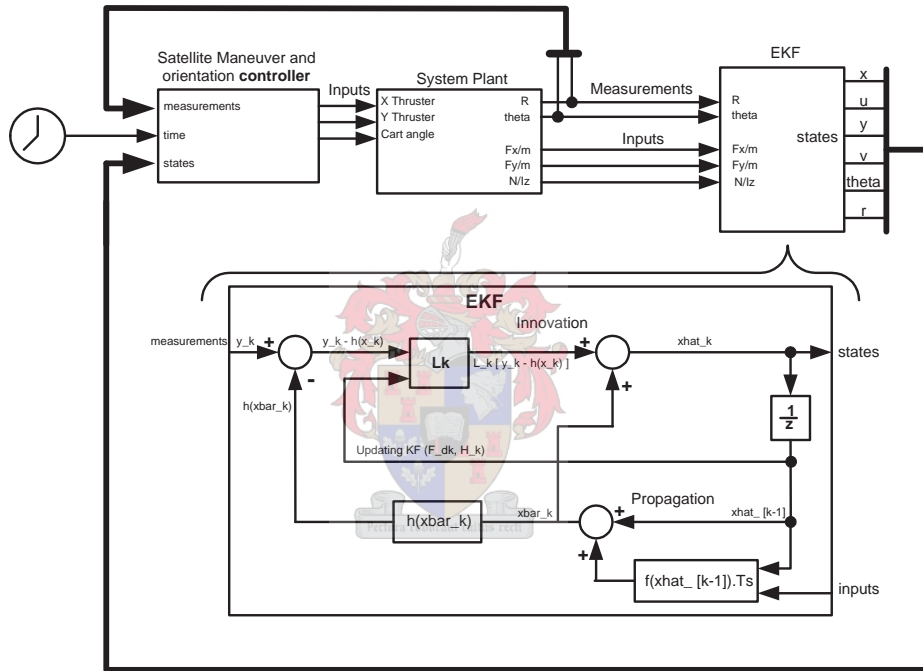


**Figure 5.8:** Block diagram of System with Controller and EKF

The process and measurement noise co-variance matrices ( $Q_k$  and  $R_k$  respectively) used to calculate the Kalman filter gain ( $L_k$ ) are,

$$Q_k = 2\alpha\sigma_m^2 \begin{bmatrix} 1 & 0 & 0 & 0 & 0 & 0 \\ 0 & 0.1 & 0 & 0 & 0 & 0 \\ 0 & 0 & 1 & 0 & 0 & 0 \\ 0 & 0 & 0 & 0.1 & 0 & 0 \\ 0 & 0 & 0 & 0 & 0.001 & 0 \\ 0 & 0 & 0 & 0 & 0 & 0.0001 \end{bmatrix} \quad (5.12)$$

$$R_k = \begin{bmatrix} \sigma_R^2 & 0 \\ 0 & \sigma_\theta^2 \end{bmatrix} \quad (5.13)$$

The values of  $\alpha$ ,  $\sigma_m^2$ ,  $\sigma_R^2$  and  $\sigma_\theta^2$  are calculated in Appendix G.2. Fig. 5.8 illustrates the implementation of the EKF in Matlab. In the simulation, the cart was maneuvered over the first 3 segments on the 4-segment semicircle.

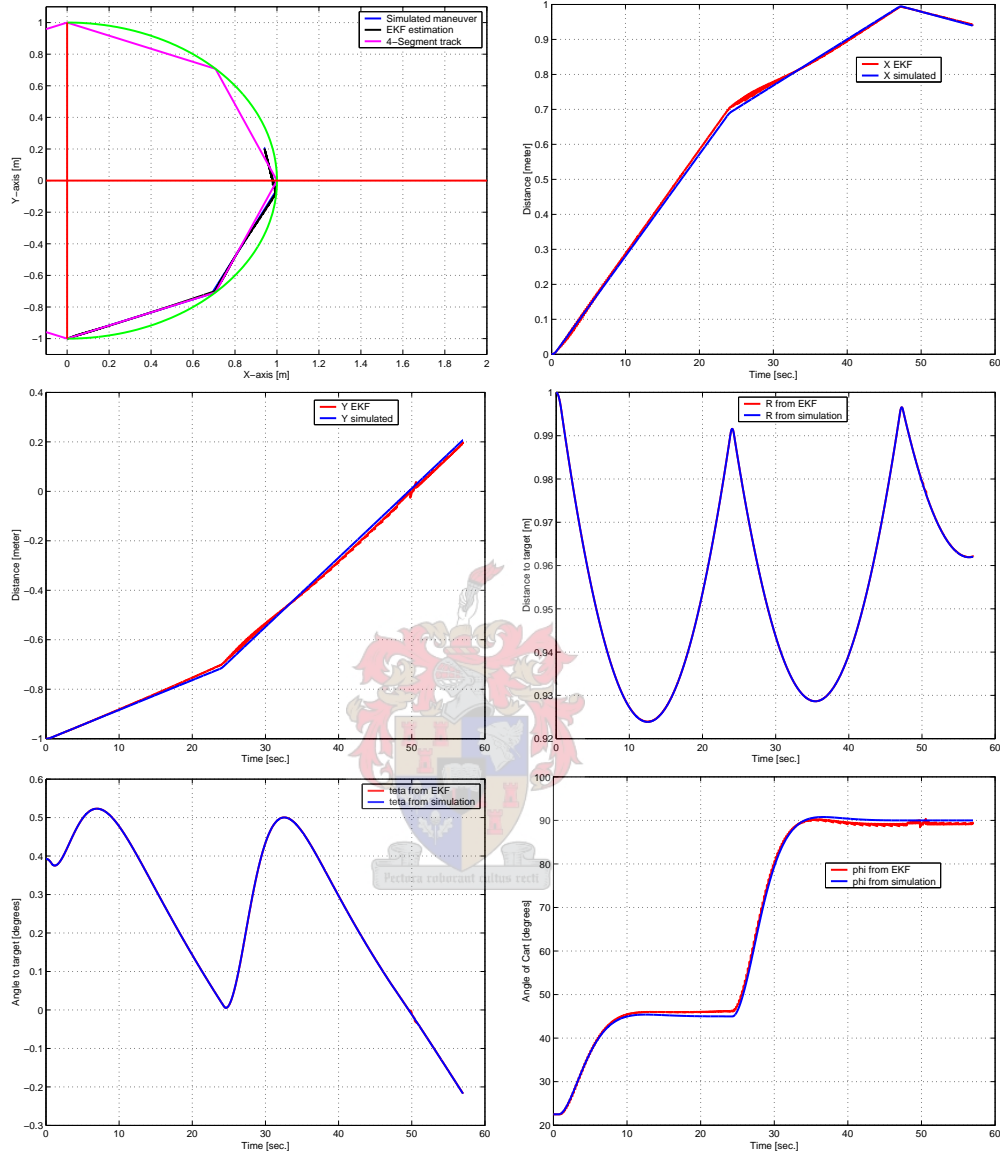


**Figure 5.9:** *Simulation and EKF measurements*

Fig. 5.9 illustrates state estimates from the EKF and simulation measurements. Included in this are position and cart angle measurements. From this figure, it is evident that the filter estimates the states correctly. The propagation and innovation of the filter is implemented at 200msec. The Kalman filter gain equations used to calculate  $L_k$  are implemented at 1 sec. intervals.  $P_k$  is initialized with zeros.

### 5.3.2 Implementing the EKF

The control program on the PC was written in Delphi and communicates with the microprocessor on the cart via RS232 using an RF link [13]. This program receives measurements from the microprocessor which the EKF uses to estimate states. The inputs to the system ( $\frac{F_x}{m} = a_x, \frac{F_y}{m} = a_y, \frac{N}{I_z} = \dot{r}$ ) are also required by the EKF, and are taken from the controller commands in the control program.

The propagation and innovation equations of the EKF are implemented in a 200 msec. period. The EKF gain ( $L_k$ ) is calculated every second with updated  $H_k$  and  $F_{dk}$  matrices (Eq. 5.9 and 5.11).

The maneuver implemented with the cart is controlled by the above mentioned program. This program uses a combination of the EKF estimated states and measurements to implement the strategy from Section 3.1.2. During the maneuver, when the thrusters are switched on, the ultrasonic sensors measurements are clamped and switched off. (The vibration and sound intensity interrupts the working condition of the ultrasonic sensors.) During this period the EKF makes a position error but as soon as a new measurement is available this is corrected. Because the time that the thrusters are switched on for is about the same as the EKF gain update time, this does not have a big influence. This problem is however further investigated in Section 6.3.

## 5.4 Overview of System

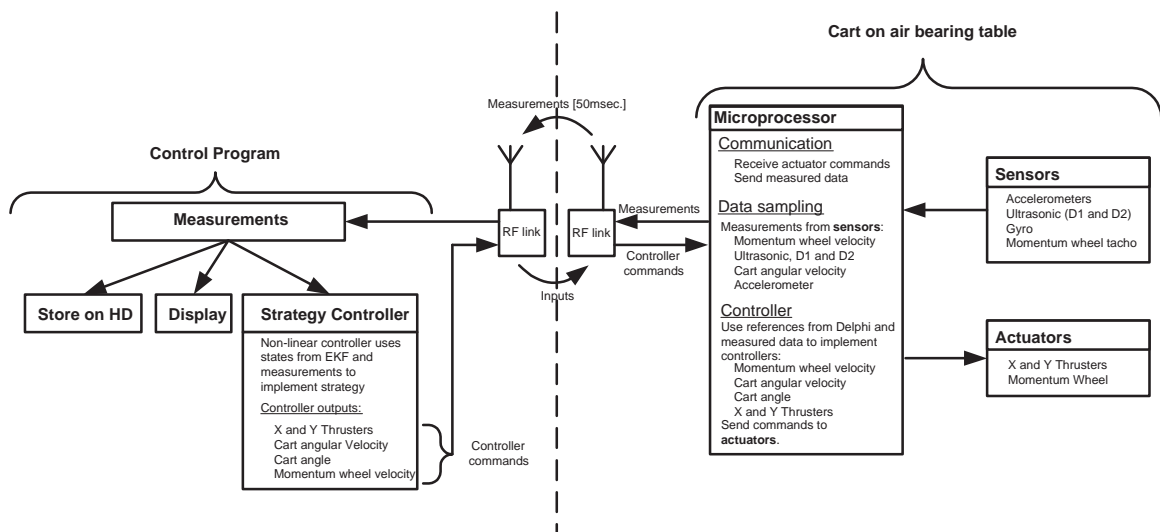


Figure 5.10: System layout

The system consists of two parts, the control program and the cart. The cart is fitted with a microprocessor, sensors and actuators. This is illustrated in Fig. 5.10.

The microprocessor has three tasks:

1. Communication

The microprocessor receives commands from the control program. These commands are references to controllers, thruster ON/OFF or ultrasonic ON/OFF.

The microprocessor sends measurements to the control program in 50 msec. intervals.

2. Data sampling

Data sampling of the gyro, momentum wheel velocity and current sensors are done at 360 Hz. The accelerometer is measured at 10 Hz. These sensors are measured with the Analog to Digital converter of the microprocessor. The distances from the two ultrasonic sensors are sampled at 12.5 Hz. Sampling for the ultrasonic sensors is done with external interrupts. The value of `Timer 0` on the microprocessor is related to the distance.

3. Controller

The difference equations of the momentum wheel current and velocity, cart angular velocity and angle controllers are implemented on the microprocessor. The references from the control program are used to step the controllers. The microprocessor is also used to open and close the thrusters for discrete times. Controller outputs give actuator commands.

Fig. 5.11 illustrates the flow chart of the program implemented on the microprocessor.

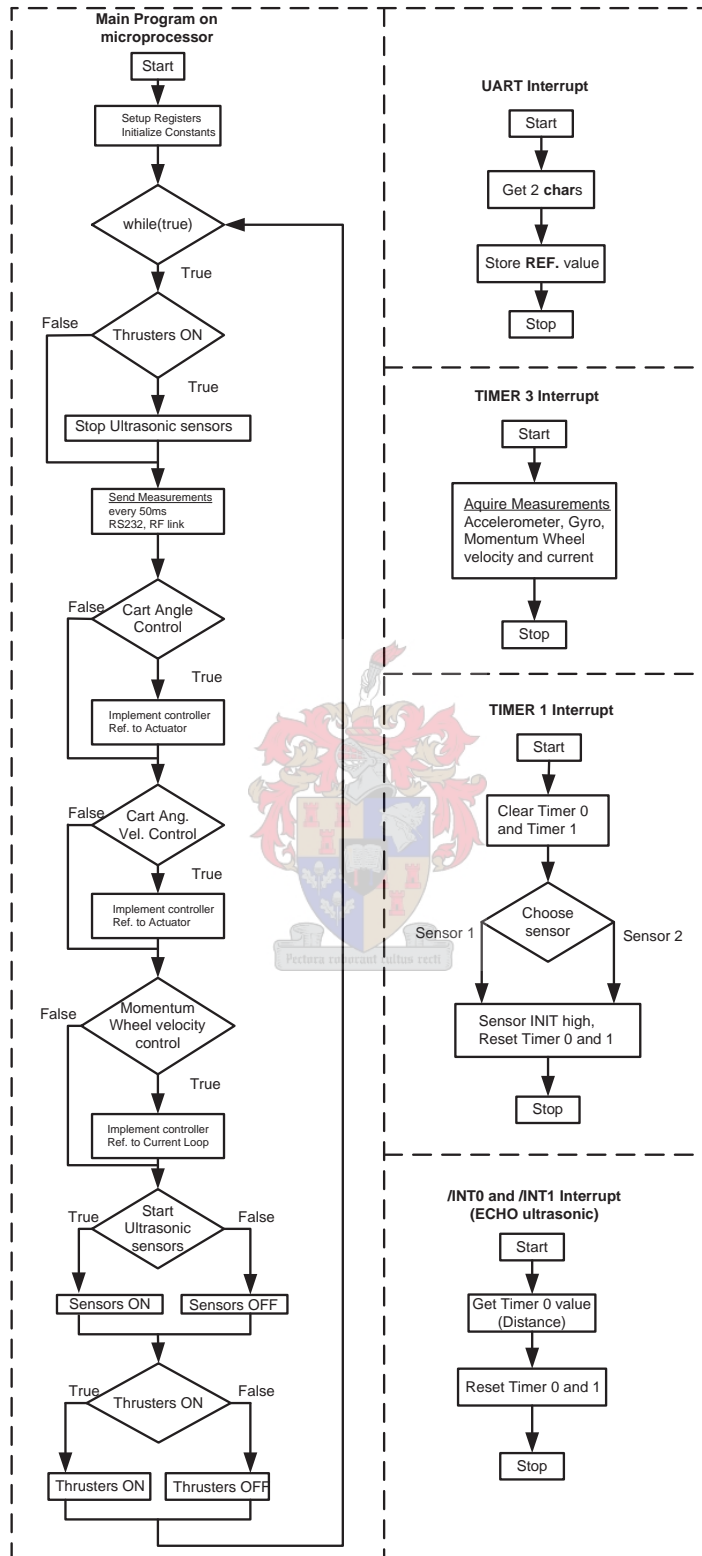


Figure 5.11: Flow chart of program on microprocessor

The control program receives measurements from the microprocessor and they are displayed on screen and stored on disk. Measurements are also used in the Kalman filter to estimate states as described in Section 5.3.2. With the states from the EKF, as well as the measurements, the maneuver is implemented and commands are sent to the microprocessor as needed.

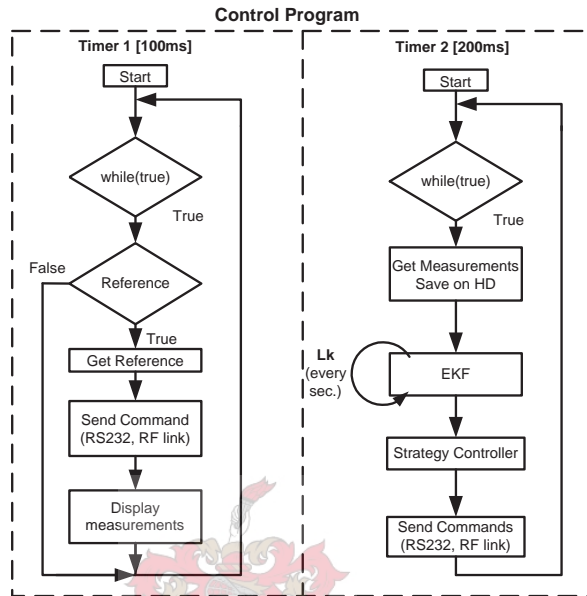


Figure 5.12: Flow chart of Delphi program

The flow chart of this program is shown in Fig. 5.12 with Timer 1 and Timer 2. Timer 1 is used for initialization and the controller/EKF is implemented with Timer 2. The GUI of the control program is displayed in Fig. 5.13. The strategy implemented with the control program is discussed in Section 6.1.1.

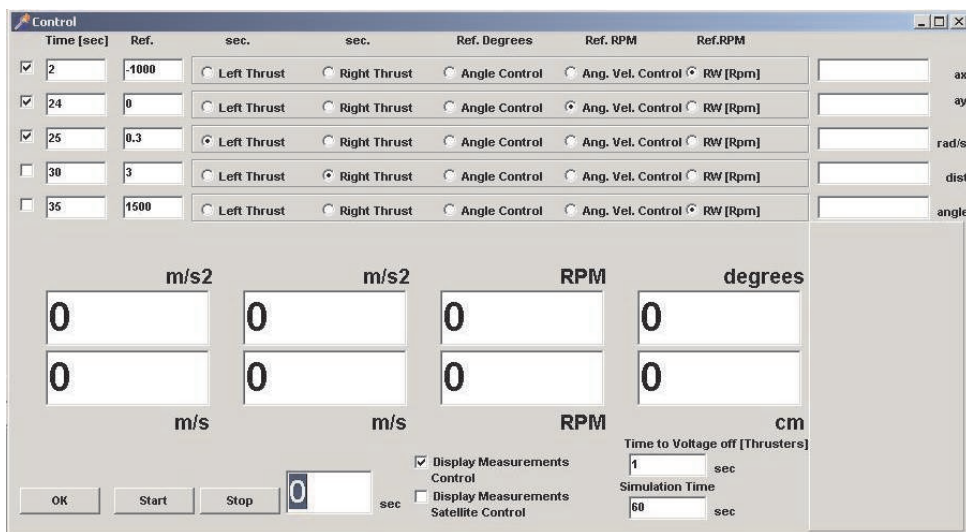


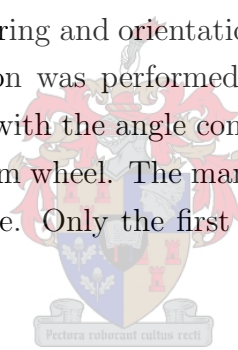
Figure 5.13: Control program GUI

# Chapter 6

## Simulation Results

### 6.1 Two Different Rotation Strategies

The strategies used for maneuvering and orientation on the air bearing table are discussed in this chapter. The orientation was performed using two different strategies. These strategies include: (1) rotation with the angle controller (Chapter 5.2) and (2) open loop angle control with the momentum wheel. The maneuver intended on the air bearing table consist of a 4-segment semicircle. Only the first 3 segments are attempted to illustrate the concept.



#### 6.1.1 Angle Control

Typical initial conditions for the cart on the air bearing table are: (1) A momentum wheel velocity of -1000 RPM, (2) the distance to the object  $R = 1$  m, (3) angle of the cart  $\phi = 22.5$  and (4) the angle measured by the ultrasonic sensors  $\theta = 22.5^\circ$ , see Fig 6.1. Just before the X thruster is switched on for 0.8 sec. to achieve an initial velocity, the angular velocity of the cart is set at 0 RPM for stabilization during thrusting.

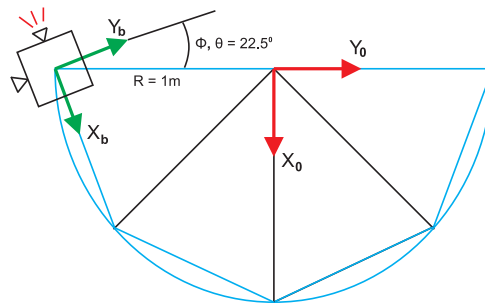


**Figure 6.1:** *Initial condition of cart*



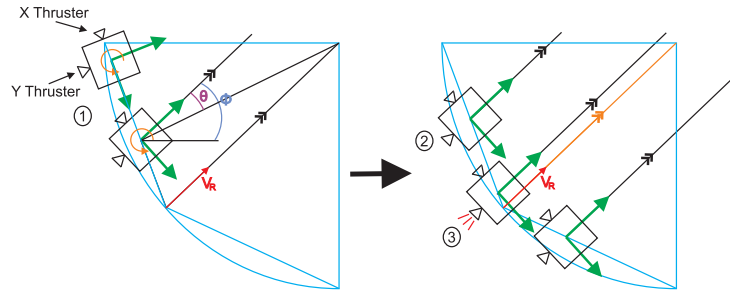


**Figure 6.2:** *Control steps on each segment*

The control steps for the transition from a segment to the next segment is (refer to Fig 6.2):

1. The angle controller is switched on when a specific condition (combination of time and angle ( $\theta$ )) is reached. The cart is rotated to align the Y thruster with the  $V_R$  vector.
2. The angular controller maintains zero angular velocity for thrust purposes after the Y thruster is aligned.
3. To compensate for overshoot the thruster is switched on before the end of the segment. The length of the thrust is calculated from Eq. 3.6.

The velocity of the cart must be low enough to give the angle controller time to rotate the cart in the  $V_R$  direction. At the end of each segment the cart still has non-zero angular velocity; therefore the thruster is switched on while rotating. The velocity of the cart is limited by the susceptibility to an uneven table and friction. Appendix H.1 gives a detailed table (Tabel H.1) of the control strategy.

## 6.1.2 Open Loop Angle Control

This non-linear strategy controller is implemented the same way as described in Section 6.1.1. The only differences are the momentum wheel bias of -2000 RPM and the rotation of the cart is performed by open loop angle control with the momentum wheel.

The acceleration of the momentum wheel is known from the pre-filter (Section 4.2.2), therefore with Eq. H.1 (Appendix H.3) the rate of the cart is calculated as,  $\dot{\omega}_{cart} = \pm 0.141 rad/s^2$ . If the momentum wheel is accelerated as in Fig. 6.3 the cart is also accelerated with the inertial relationship included. When the yellow area (Fig. 6.3) equals half the angle needed (say  $\frac{\sigma^\circ}{2}$ ), the momentum wheel is returned to its initial velocity. This gives a total angle rotated of  $\sigma^\circ$ .

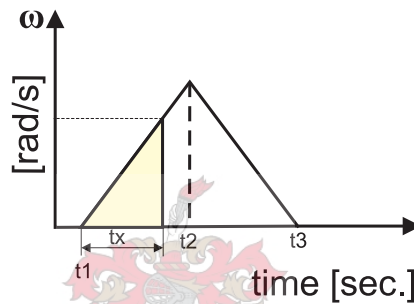


**Figure 6.3:** *Angle control of cart*

With this in mind, the time that the momentum wheel is accelerated and then decelerated can be calculated. The same is true when turning the cart in the other direction. Appendix H.2 gives a detailed table (Tabel H.2) of the control strategy.

## 6.2 Results

### 6.2.1 Angle Control

This section gives the results of the implemented strategy controller, with the rotation performed by the angle controller. The initial conditions are evident from Fig. 6.5 (left), H.1 (top, right) and H.2 (Appendix H.4). Appendix H.4 also includes figures (Fig. H.1) of the actuator commands from the controller. On each segment the three control steps from Section 6.1.1 are implemented.

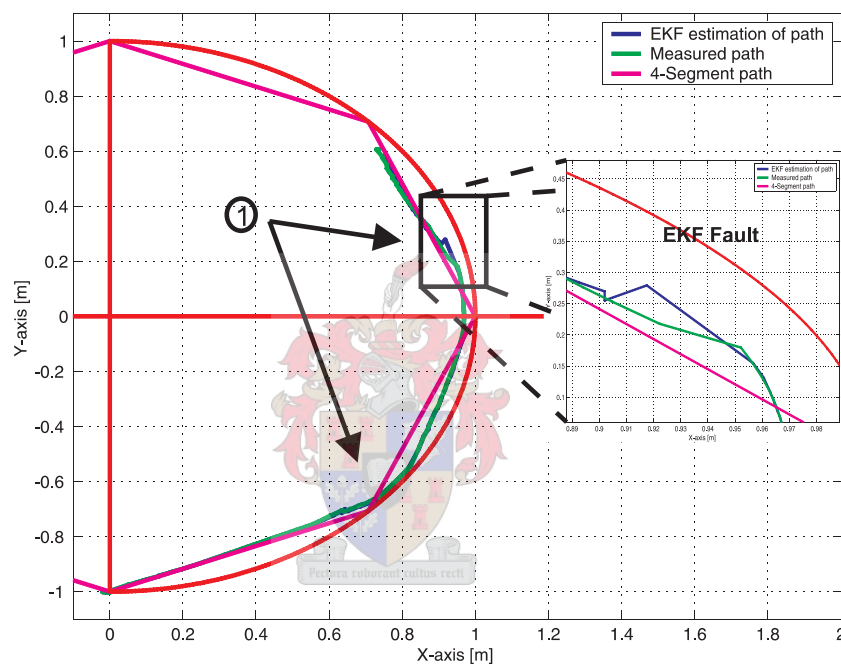


**Figure 6.4:** *Cart movement around an object*

From Fig. 6.4 it is evident that the cart was maneuvered around an object following the segments. The transition from the 1st to the 2nd segment has a small amount of overshoot but was compensated for on the transition from the 2nd to the 3rd segment. The cart ended perfectly on the third segment. The overshoot and round transition from one segment to the next is due to the slow angle controller, rotating cart (as discussed in Section 6.1.1) and an uneven table. The uneven table made it very difficult to follow the segments with the cart. The table was constantly adjusted (with great difficulty) for better measurements.

The position measurement is clamped when the ultrasonic sensors are switched off. This is done when the thrusters are switched on. This results in a fault in the EKF position estimation, see (1) in Fig. 6.4. More on this in Section 6.3.

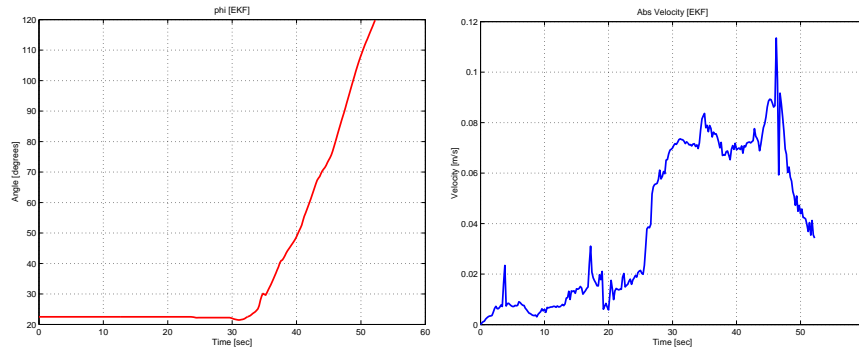


**Figure 6.5:** *EKF state measurement angle  $[\phi]$  and absolute velocity*

The continuously rotating cart is displayed in Fig. 6.5 (left). Although the cart was facing in the  $V_R$  direction on each thrust, the cart was still rotating a small amount during thrusting.

The time and angle that the Y thruster is switched on for during a transition to the next segment, is based on the principle of constant velocity. Fig. 6.5 (right) illustrates the constant velocity at 0.07m/s. The velocity increases and decreases toward the end of the measurement due to an uneven table.

To quantify the uneven effect of the table the following must be considered:

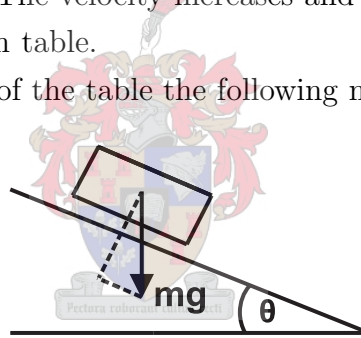


**Figure 6.6:** *Uneven table*

If the uneven table has a slope of  $\theta$ . The acceleration on the sloped surface is from Fig. 6.6:

$$\text{Acc.} = g.\sin(\theta) \quad (6.1)$$

$$\approx g.\theta \quad , \theta \text{ very small} \quad (6.2)$$

If the cart attains a velocity error of 0.01 m/s over a period of 20 sec. the constant acceleration is almost equal to  $0.0005 \text{ m/s}^2$ . With Eq. 6.2 the angle  $\theta$  is 0.51 mrad. Thus the glass table top drops  $50\mu\text{m}$  per meter, which is much worse than a granite surface ( $5\mu\text{m}$  per meter).

## 6.2.2 Open Loop Angle Control

This section gives the results of the open loop angle control strategy. The same experiment is performed as in Section 6.2.1, but now the cart is rotated with an open loop angle controller as discussed in Section 6.1.2. The initial conditions are evident from Fig. 6.8 (left), H.5 (top, right) and H.6 at a time prior to 25 sec. (Appendix H.5). Actuator command measurements are shown in Fig. H.5.

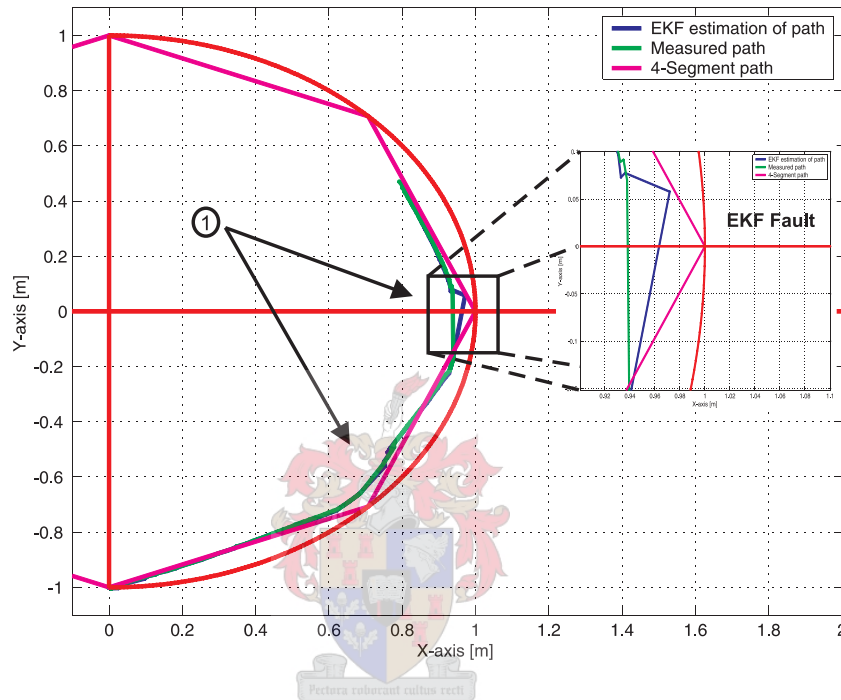


**Figure 6.7:** *Cart movement round an object*

From Fig. 6.7 it is evident that the cart was successfully maneuvered around the object. This measurement shows a compensation for overshoot on each segment and the cart therefore follows the segmented track perfectly. The reason for the earlier transition between the two segments is the faster rotation of the cart with the open loop angle controller. The open loop angle control has its drawbacks, one being zero disturbance rejection. Because the position measurement is clamped when the thrusters are switched on, the estimated EKF position is faulty in this period, see (1) from Fig 6.7. To get a good measurement the table had to be leveled with great difficulty. The table is very stiff, if one of the feet is adjusted the whole table tends to twist. This gives an endless iterative process for leveling.

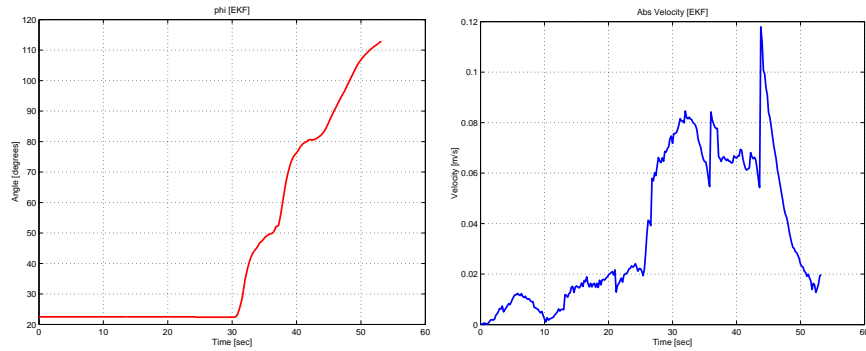
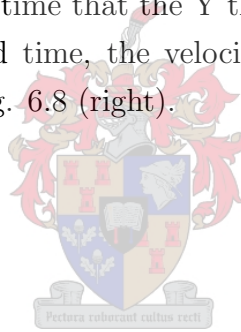


**Figure 6.8:** *EKF state measurement  $[\phi]$  and absolute velocity*

The two open loop angle rotations are illustrated in Fig. 6.8 (left). On the 3rd segment, the cart is controlled to face the object and the angle does not settle. It is clear from the angle measurement that the open loop angle control is much faster than the closed loop one. The thruster could be switch on earlier to compensate for overshoot. In this thrust period the cart has a smaller angular velocity.

With the velocity estimate, the time that the Y thruster is switched on for is calculated. By thrusting for this calculated time, the velocity is kept constant at 0.07m/s except where the table was uneven, Fig. 6.8 (right).



### 6.3 Kalman Filter Correction

The jumps in the X and Y (Fig. H.3 and H.7) position estimation of the EKF are due to the absence of new measurements. This occurs when the ultrasonic sensors are switched off (when the thrusters are switched on). To restore this problem the Kalman filter is propagated without new measurements to correct the position. This propagation is done with the innovation as,  $\hat{\underline{x}}_k = \underline{\bar{x}}_k + 0$ , instead of,  $\hat{\underline{x}}_k = \underline{\bar{x}}_k + L_k[y_k - h(\underline{\bar{x}}_k)]$  (Eq. 2.33). When new measurements are not available,  $L_k$  is not required. As soon as new measurements are available, the innovation is done with the updated  $L_k$  term to calculate the new EKF states. With this modification, the strategy (rotation done with the angle controller) is implemented and the position measurements and EKF estimates are illustrated in Fig 6.9.

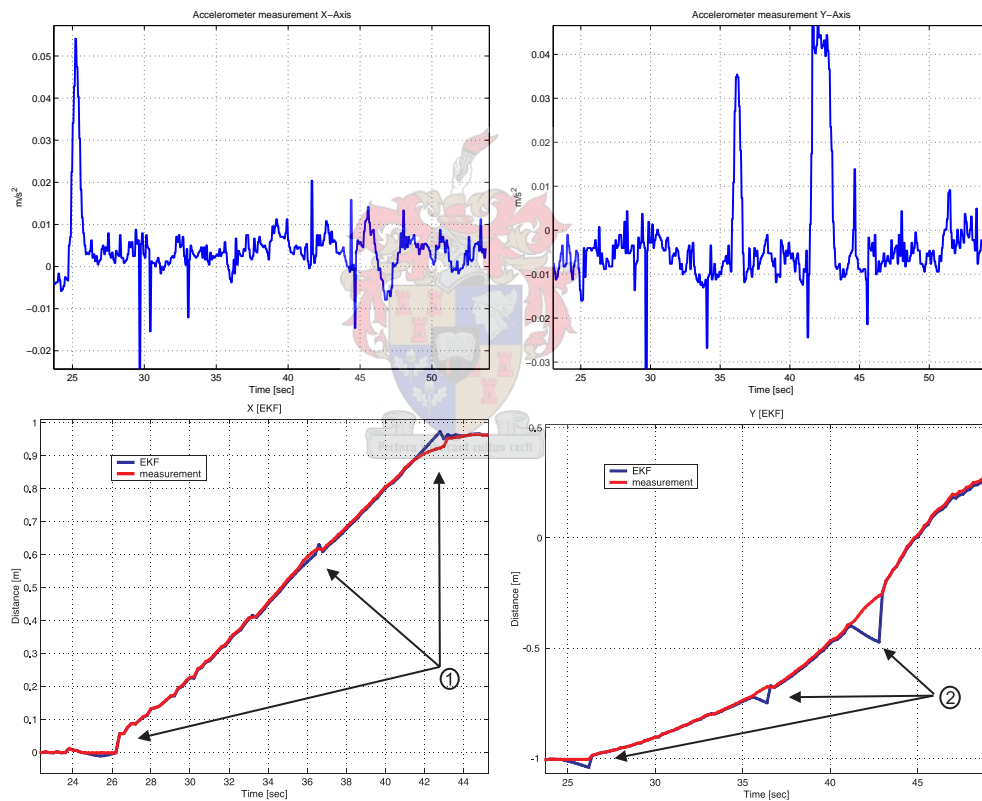


**Figure 6.9:** Acceleration measurement and EKF position state measurement

From the figure above (see (1) and (2)) it is evident that the filter propagates when the thrusters are switched on. This results in the deviation. The estimation is not very accurate without new measurements. When the new measurements are available, a state correction is done and the filter tracks the measurement.

# Chapter 7

## Conclusion

### 7.1 Summary

The aim of this thesis was to investigate satellite maneuvering and orientation on an air bearing table. The testing of the designed system was successfully implemented on an air bearing table with a cart moving around a stationary object. The application anticipated is an inspection satellite maneuvering around another satellite for docking purposes. The following results were obtained in this thesis:

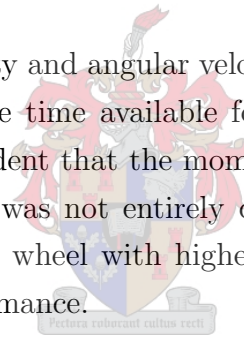
- A complete mathematical model for the maneuver and orientation was designed and implemented in Matlab for simulation. Due to the 2D constrained testing environment the model was only developed for this scenario.
- From this mathematical model a control strategy was designed and simulated for maneuvers around an object. Several options such as circular or segmented motion around the object were considered. From this, the conclusion was made that the segmented maneuver uses less gas and is therefore less expensive and more attractive.
- Sensors and actuators were developed for implementing the strategy on the air bearing table. Sensors included an accelerometer, gyroscope and position sensor. The accelerometer and gyroscope was used to measure the acceleration and angular velocity of the cart. Two ultrasonic sensors were used to determine the distance and angle to the object. The actuator developed was the momentum wheel used for orientation.



- Controllers were designed for the cart angle and angular velocity. These together with the states estimated by an EKF were used to successfully implement the non-linear control strategy.
- Finally, the cart was successfully maneuvered and orientated around an object thereby demonstrating that the strategy was implemented successfully. Obtaining measurements were problematic due to the un-modeled force of the uneven table.
- The cart with the developed electronics, provides a fully functional system that can be used to maneuver and orientate on the air bearing table in future projects.

Another goal of this thesis was to investigate different options of maneuvering around an object. Through simulation it was clear that if circular movement was approximated with segments, the least amount of gas was used for this application. Dividing the semicircle into 4 segments was the most economical when the amount of thrust time and position sensor angle width was considered. The first 3 segments were successfully demonstrated on the air bearing table.

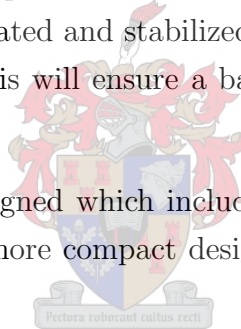
The balance between the velocity and angular velocity of the cart was critical. The faster the cart moved, the shorter the time available for the momentum wheel to rotate the cart. From the results, it is evident that the momentum wheel was able to turn the cart in this short time, but that it was not entirely capable of stopping the cart's rotation when thrusting commenced. A wheel with higher performance capabilities will lead to greatly enhanced system performance.



## 7.2 Recommendations

The following is a list of recommendations for the future work on the system:

- From experience on the air bearing table, it was evident that leveling the table is not easy and that it influences measurements drastically. A properly level table would therefore be a first priority for better quality maneuver measurements.
- For further maneuvering and orientation on the air bearing table, an absolute position and orientation sensor is needed. This is due to the lack of position sensing when no target is detected by the ultrasonic sensors. One suggestion is a camera fitted on the ceiling facing the air bearing table. With this camera and the appropriate algorithm, the cart's orientation and position can be found.
- If a wheel with a greater moment of inertia is fitted to the DC motor, the cart could be rotated faster. A more powerful motor would also help in this regard. This will ensure that the cart is rotated and stabilized before the end of a segment when the thrusting commences. This will ensure a balance between the velocity of the cart and its angular velocity.
- A new PCB could be designed which includes all the electronics from the system. This will give a smaller, more compact design and decrease the EMC, resulting in better measurements.
- From a docking point of view the cart could be maneuvered over all the segments and stopped at the end. The cart could then be rotated to face the object after the maneuvering. This would illustrate a full docking procedure for an inspection satellite moving around an object and docking from the other side. This would be very similar to the simulation in Chapter 3.1.2.



# Bibliography

- [1] MOHAN, N., UNDERLAND T. M. and ROBBINS W. P., Power Electronics : Converters, Applications and Design. *John Wiley & Sons Inc., 1995*
- [2] HOROWITZ P. and HILL W., The Art of Electronics. *Cambridge University, 1995*
- [3] FRANKLIN G. F., POWELL J. D. and WORKMAN M., Digital Control of Dynamic Systems. *Addison Wesley Longman, Inc., 1998*
- [4] FRANKLIN G. F., POWELL J. D. and EMAMI-NAEINI A., Feedback Control of Dynamic Systems. *Prentice-Hall, Inc., 2002*
- [5] HAUS H. A. and MELCHER J. R., Electromagnetic Fields and Energy. *Prentice-Hall, Inc., 1989*
- [6] SENSCOMP GLOBAL COMPONENTS, <http://www.senscomp.com>, World Wide Web, August 2005.
- [7] SENSCOMP GLOBAL COMPONENTS, 600 Series Smart Sensor (Instrument grade), World Wide Web, <http://www.senscomp.com/600smartsensor.htm>, August 2005.
- [8] SERWAY R. A. and BEICHNER R. J., Physics of Scientists and Engineers, 5th Edition. *Saunders College Publishing, 2000*
- [9] ANALOG DEVICES, Angular Rate Sensor ADXRS150, World Wide Web, Data Sheet, <http://www.analog.com/en/prod/0,2877,ADXRS150,00.html>, September 2005
- [10] ANALOG DEVICES, ADXL311 - Dual Axis Accelerometer, World Wide Web, Data Sheet, <http://www.analog.com/en/prod/0,2877,ADXL311,00.html>
- [11] TEXAS INSTRUMENTS, OPA2340 Opamp, World Wide Web, Data Sheet, <http://focus.ti.com/lit/ds/symlink/opa2340.pdf>

- [12] JONES T., Advanced Estimation 813 - Course Notes, Lecture 5. *University of Stellenbosch, 2005*
- [13] HANDYWAVE, HandyPort Wireless RS-232 Transceiver (HPS-120), World Wide Web, <http://www.handywave.com>, September 2005
- [14] BERNER R., Control Moment Gyro Actuator for Small Satellite Applications. *University of Stellenbosch, 2004*
- [15] STEYN W. H., A Multi-Mode Attitude Determination and Control System for Small Satellites, *University of Stellenbosch, 1995*
- [16] WERTZ JAMES R. and LARSON WILEY J., Space Mission Analysis and Design, 3rd Edition. *Microcosm, Inc. and W.J. Larson, 1999*
- [17] TREURNICHT J., Axis Transforms. *University of Stellenbosch, 2003*
- [18] SILICON LABORATORIES, Cygnal C8051F005, World Wide Web, Data Sheet, [http://www2.silabs.com/public/documents/tpub\\_doc/dsheet/Microcontrollers/Precision\\_Mixed-Signal/en/C8051F0xx.pdf](http://www2.silabs.com/public/documents/tpub_doc/dsheet/Microcontrollers/Precision_Mixed-Signal/en/C8051F0xx.pdf)
- [19] SINGER R. A., Estimating Optimal Tracking Filter Performance for Manned Maneuvering Targets, *IEEE Transactions on Aerospace and Electronic Systems, July 1970*
- [20] VAN DAALEN C. E., Strategies for the control of a satellite with thruster misalignment, *University of Stellenbosch, 2005*
- [21] MICHIGAN AEROSPACE CORPORATION, Website, <http://www.michigan.aero.com/satellitedocking/index.shtml>, September 2005
- [22] MA O., Website, [http://saratoga.nmsu.edu/oma/Industrial\\_Exp/Satellite\\_docking.htm](http://saratoga.nmsu.edu/oma/Industrial_Exp/Satellite_docking.htm), September 2005
- [23] SEN P.C., Principles of Electric Machines and Power Electronics, 1st Edition. *John Wiley & Sons Inc., 1997*
- [24] POZAR D. M., Microwave and RF Design of Wireless systems. *Wiley, 2001*
- [25] SKOLNIK, Introduction to Radar Systems, International Student Edition. *McGraw - Hill Kogakusha, Ltd.*
- [26] STANDER M., 'n Ondersoek na 'n aktiewe infrarooi volger wat 'n sein kan volg. (Investigation of an active infrared tracker tracking a signal), Project. *University of Stellenbosch, 1999*

- [27] WOOD C., The Design of a spectroscope to demonstrate spectroscopy techniques. *University of Stellenbosch, 2001*
- [28] HIBBELER R.C., Engineering Mechanics Dynamics. *Prentice Hall, 1995*
- [29] SPEIGEL M. R., Schaum's outline series: Theory and Problems of Theoretical Mechanics. *McGraw - Hill, 1967*
- [30] SIPEX, SP3232ECP, World Wide Web, Data Sheet, <http://www.sipex.com>
- [31] *Moment of Inertia Measurement*, Website, [http://www.sdrl.uc.edu/ucme571/moment\\_inertia.pdf](http://www.sdrl.uc.edu/ucme571/moment_inertia.pdf), September 2005
- [32] PEDDLE I. K., Autonomous Flight of a Model Aircraft. *University of Stellenbosch, 2004*
- [33] ZHOU K. and DOYLE J. C., Essential of Robust Control. *Prentice Hall, 1998*
- [34] ZILL D. G. and CULLEN M. R., Advanced Engineering Mathematics, 2nd Edition. *Jones and Bartlett Publishers, 2000*
- [35] PEBLES P. Z. JR., Probability, Random Variables and Random Signal Principles, 4th Edition. *McGraw Hill, 2001*
- [36] MAXON MOTOR USA, DC-Tacho, World Wide Web, Data Sheet, <http://www.maxonmotorusa.com/products/feedback.cfm>, September 2005
- [37] SUNSPACE, World Wide Web, <http://www.sunspace.co.za/>, September 2005

# Appendix A

## Strategy Results

### A.1 Sensor Angle Width

From the following figures, the angle width of the position sensors is determined for a different number of segments.

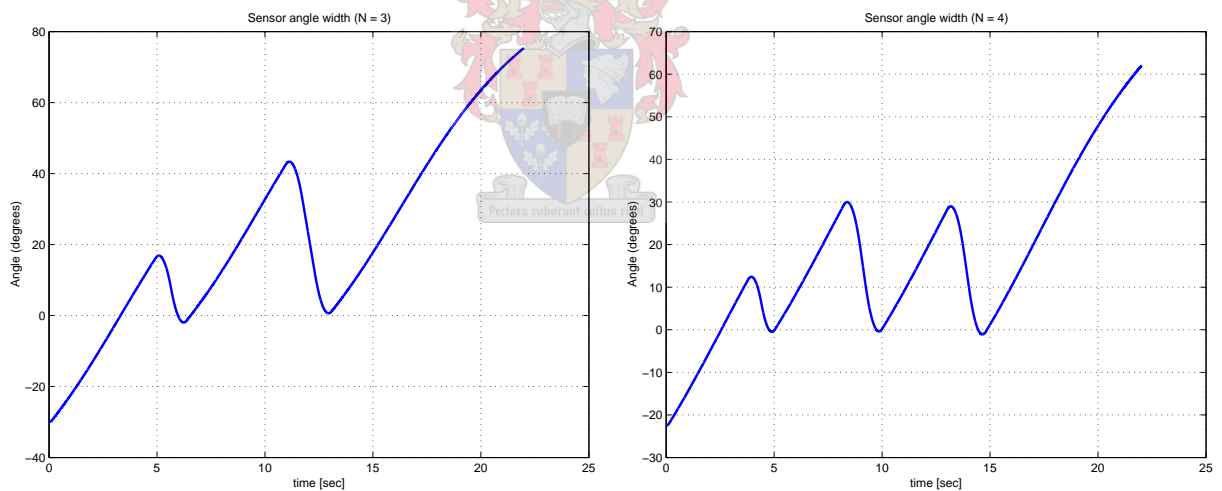


Figure A.1: *Sensor Angle Width*

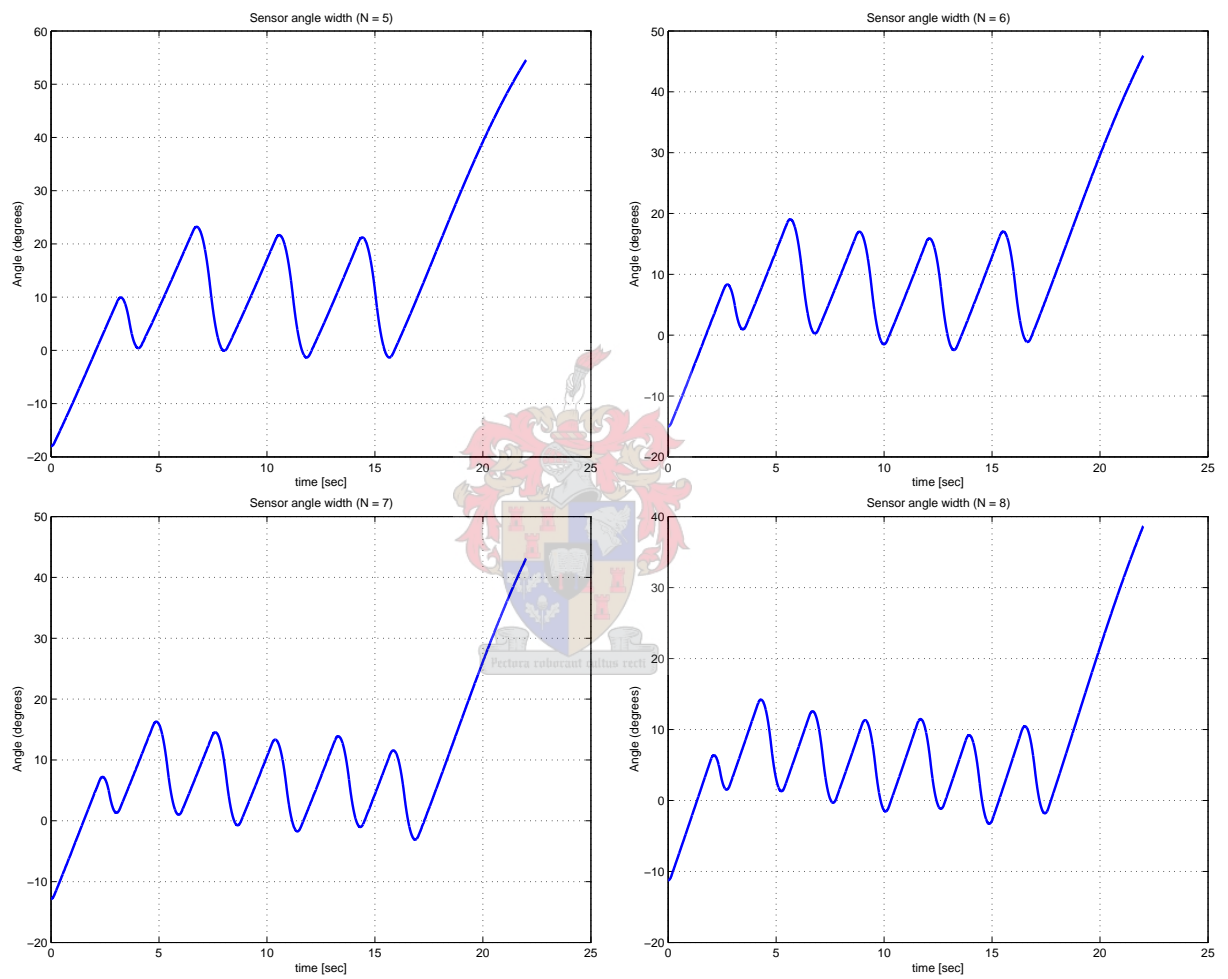


Figure A.2: *Sensor Angle Width*

# Appendix B

## Ultrasonic Sensor

### B.1 Aperture Mask

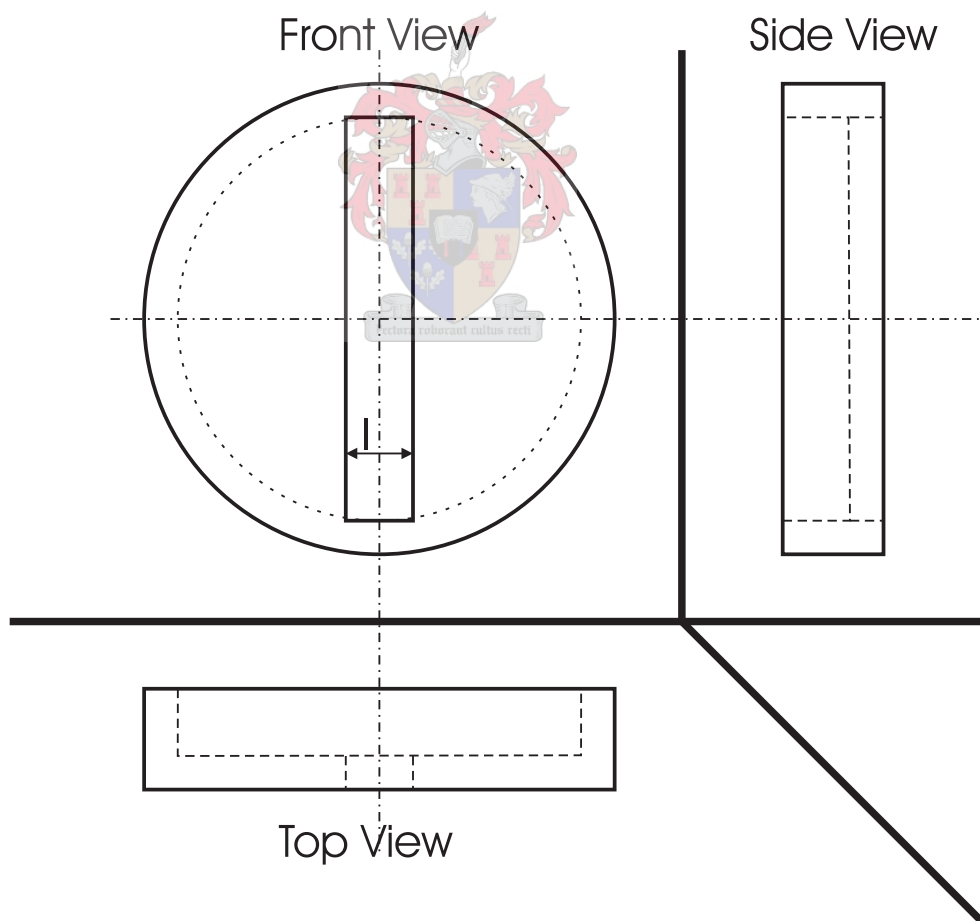


Figure B.1: *Aperture Mask of the Ultrasonic sensor*





**Figure B.2:** *Picture of Aperture Mask and Casing of the Ultrasonic Sensor*

## B.2 Sensor position

$\theta$  (the angle the sensors are rotated with respect to one another) is calculated as follow from Fig. 4.3:

$$180^\circ = BA + 2\Psi \quad (\text{B.1})$$

$$\Psi = \alpha + \theta \quad (\text{B.2})$$

Eq. [B.2] in Eq. [B.1]

$$180^\circ = BA + 2(\alpha + \theta) \quad (\text{B.3})$$

$$180^\circ = BA + 2\alpha + 2\theta \quad (\text{B.4})$$

$$2\alpha = 180 - BW \quad (\text{B.5})$$

Eq. [B.5] in Eq. [B.4]

$$180^\circ = BA + 180 - BW + 2\theta \quad (\text{B.6})$$

$$\theta = -\frac{1}{2}(BA - BW) \quad (\text{B.7})$$

The distance between the two sensors  $L$  (Fig. 4.3) is calculated from:

$$l1 = l2 = l \quad (\text{B.8})$$

$$L = 2l \quad (\text{B.9})$$

$$\phi = 90 - \theta \quad (\text{B.10})$$

$$\tan\phi = \frac{R}{l}, \text{ thus} \quad (\text{B.11})$$

$$L = 2\frac{R}{\tan\phi} \quad (\text{B.12})$$

$$L = 2\frac{R}{\tan(90 - \theta)} \quad (\text{B.13})$$

$$L = 2R\frac{1}{\cot\theta} \quad (\text{B.14})$$

$$L = 2R\tan\theta \quad (\text{B.15})$$

### B.3 Object position

With the following equations, the distance and angle to the object is calculated.

$$D2^2 = D1^2 + L^2 - 2 D1 L \cos(c), \quad \text{Solve for } c \quad (\text{B.16})$$

$$c = \cos^{-1}\left(\frac{D2^2 - D1^2 - L^2}{-2 D1 L}\right) \quad (\text{B.17})$$

Now with  $c$ ,  $D$  can be calculated

$$D^2 = D1^2 + \left(\frac{L}{2}\right)^2 - 2 D1 \frac{L}{2} \cos(c) \quad [\text{Distance to object}] \quad (\text{B.18})$$

with  $D$  from B.18 the angle  $\rho$  can be calculated

$$D1^2 = D^2 + \left(\frac{L}{2}\right)^2 - 2 D \frac{L}{2} \cos(\rho) \quad (\text{B.19})$$

$$\rho = \cos^{-1}\left(\frac{D1^2 - D^2 - \left(\frac{L}{2}\right)^2}{-2 D \frac{L}{2}}\right) \quad [\text{Angle to object}] \quad (\text{B.20})$$

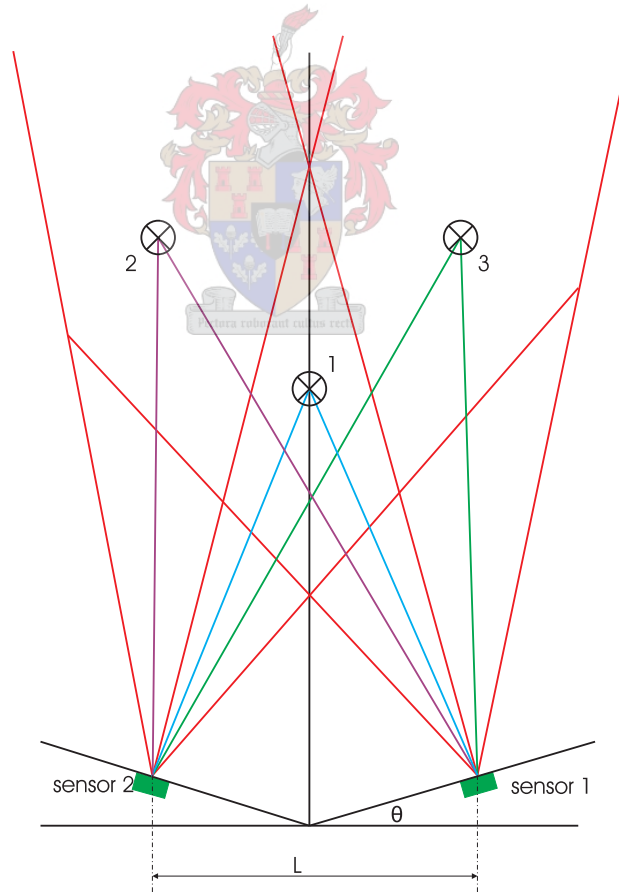


Figure B.3: Object detection

## B.4 Signal Inversion

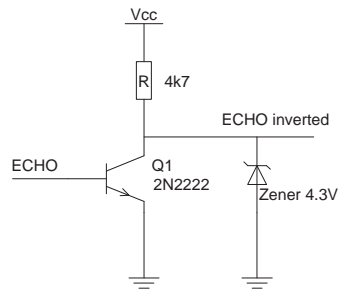


Figure B.4: *ECHO inversion*

## B.5 Flow Chart of position detection program

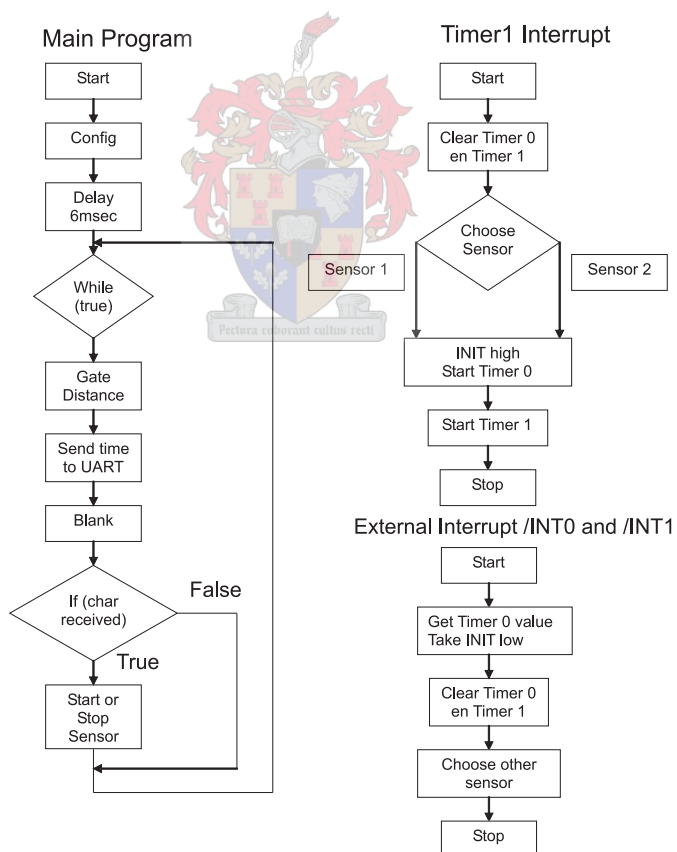


Figure B.5: *Flow chart of position detection program*

# Appendix C

## DC motor model

From [1] the following equations of the DC motor are appropriate :

$$T_{em} = K_T I_a \tag{C.1}$$

$$E_a = K_E \omega_m \tag{C.2}$$

$$V_t = E_a + R_a I_a + I_a L_a s \tag{C.3}$$

$$T_{em} = J\dot{\omega} + B\omega + T_{WL}, \text{ choose } T_{WL} = 0 \tag{C.4}$$

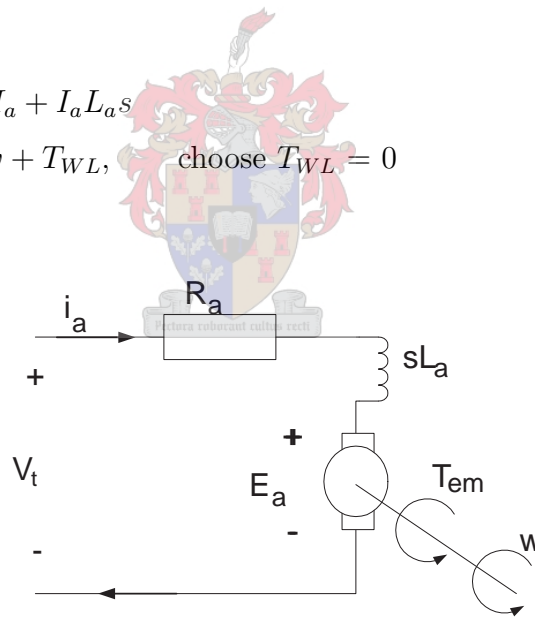


**Figure C.1:** DC Motor equivalent circuit

Consider only one direction of movement for the momentum wheel from Fig. 4.8 (red line). Assume an ideal Mosfet, therefore ignore voltage drop and losses in Q1. Include some extra resistance with,  $R_a$ , the motor resistance [Fig. C.1,  $R_a = 1.23\Omega$ ] to cover these losses. The DC motor current plant equation is defined in (Eq. C.3). With  $E_a$  considered small enough to be zero the equation is simplified as:

$$\frac{I_a}{V_t} = \frac{1}{R_a + sL_a} \tag{C.5}$$

From the datasheet and schematics, the following constants are evident and are necessary for the model:

Supply Voltage,  $V_{cc} = 12 - 14V$  depending on whether the battery is charged or not

Current sensing resistor,  $R = 0.15\Omega$

Terminal resistance,  $R_a = 1.23\Omega$

Terminal inductance,  $L_a = 0.12 \times 10^{-3}H$

Torque constant,  $K_t = 16.3mNm/A$

Damping,  $B \approx 0$

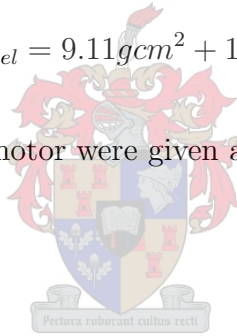
Electric constant,  $K_e = 0.016323 V/\frac{rad}{s}$  from,

$$\text{Speed constant} = 585 \left[ \frac{rpm}{V} \right] = 585 \left[ \frac{rpm}{V} \right] \times \frac{2\pi}{60} = 61.261 \left[ \frac{rad/sec}{V} \right]$$

The total inertia of the momentum wheel consists of the inertia of the rotor and that of the momentum wheel attached to the rotor.

$$J = J_{motor} + J_{momentum\ wheel} = 9.11gcm^2 + 1.5 \times 10^{-3}kgm^2 = 1.500911 \times 10^{-3}kgm^2$$

The electronics for driving the motor were given and the schematic is shown in Fig. C.2, C.3 and C.4.



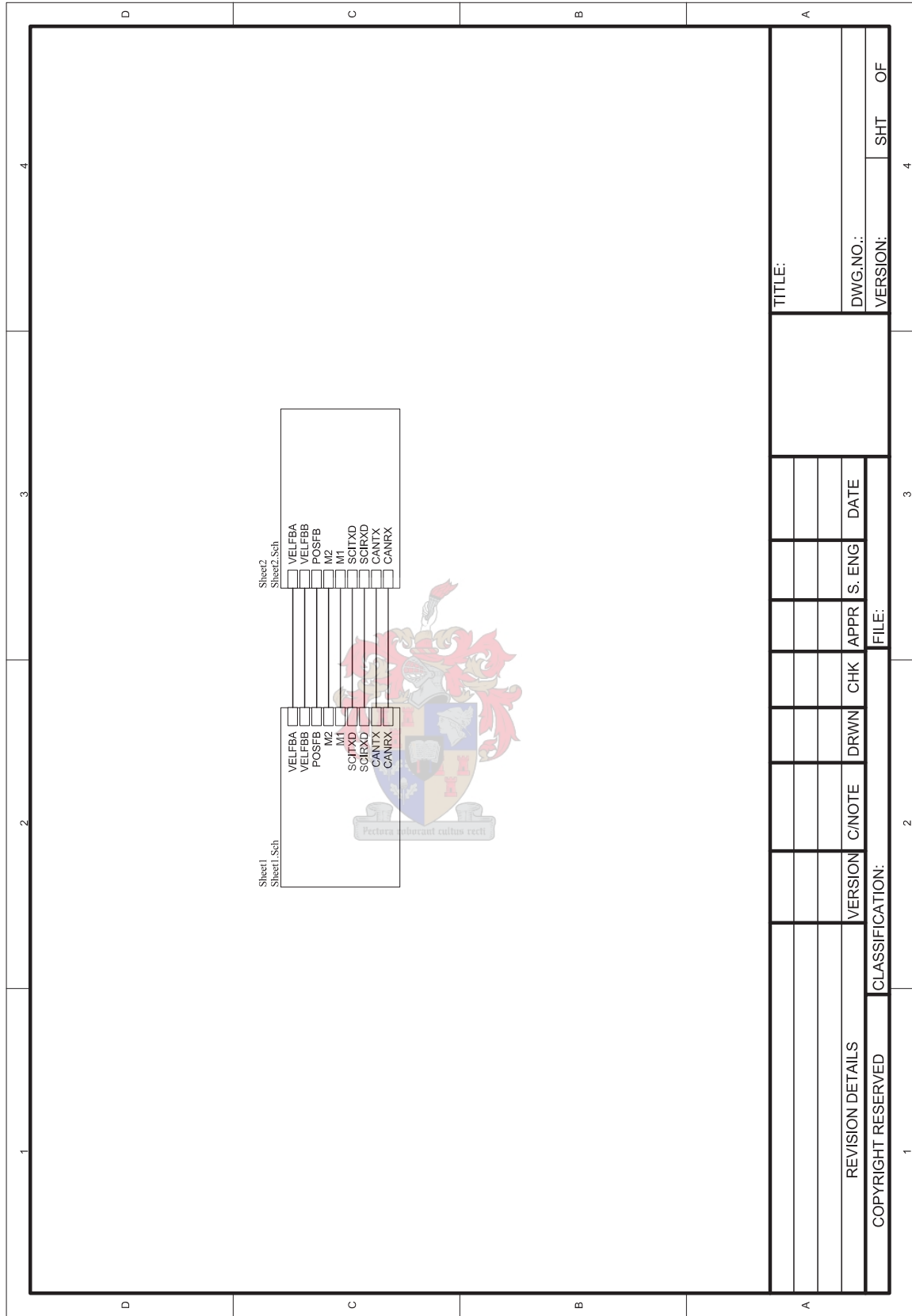


Figure C.2: DC motor Electronics schematic

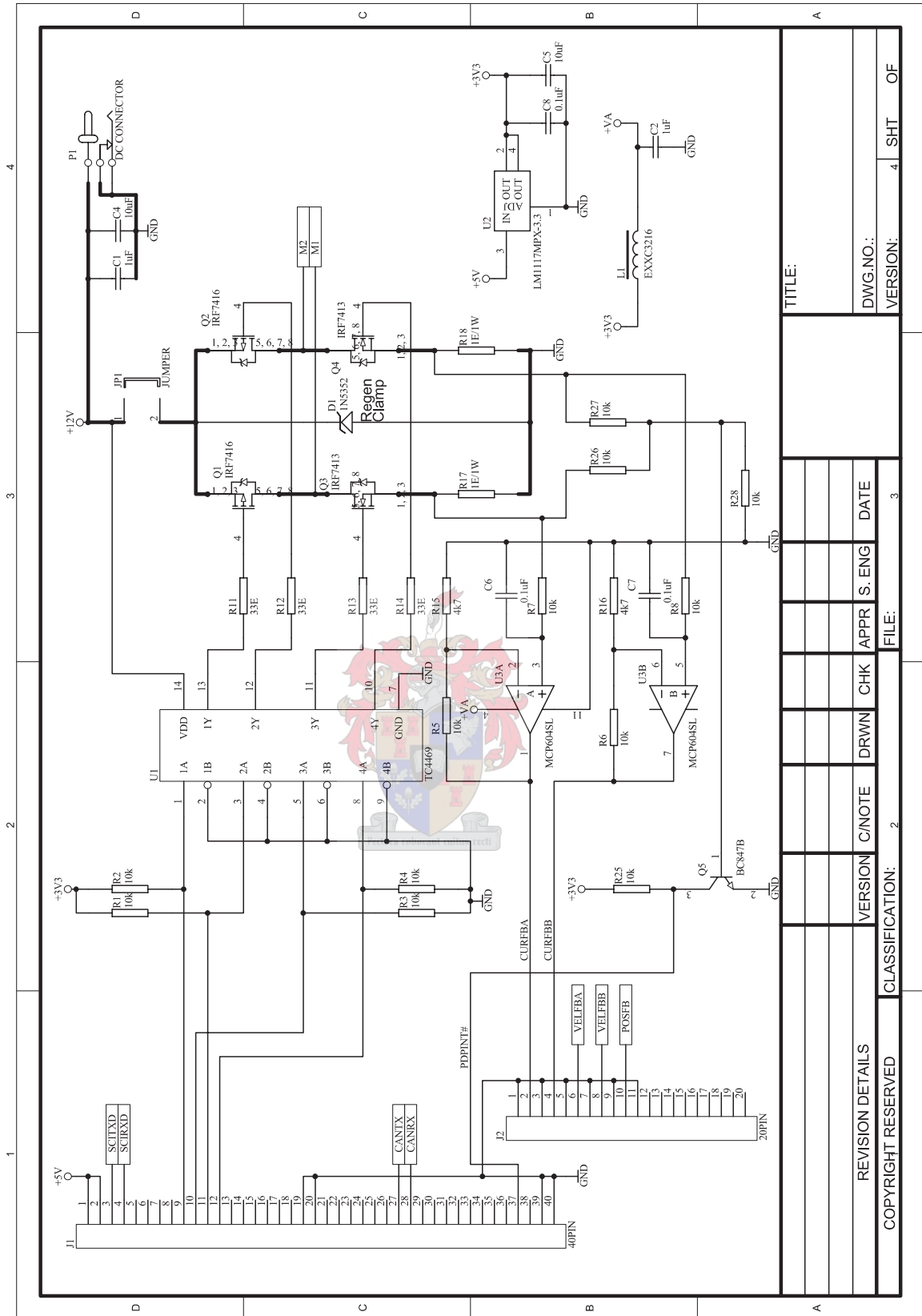


Figure C.3: DC motor Electronics schematic



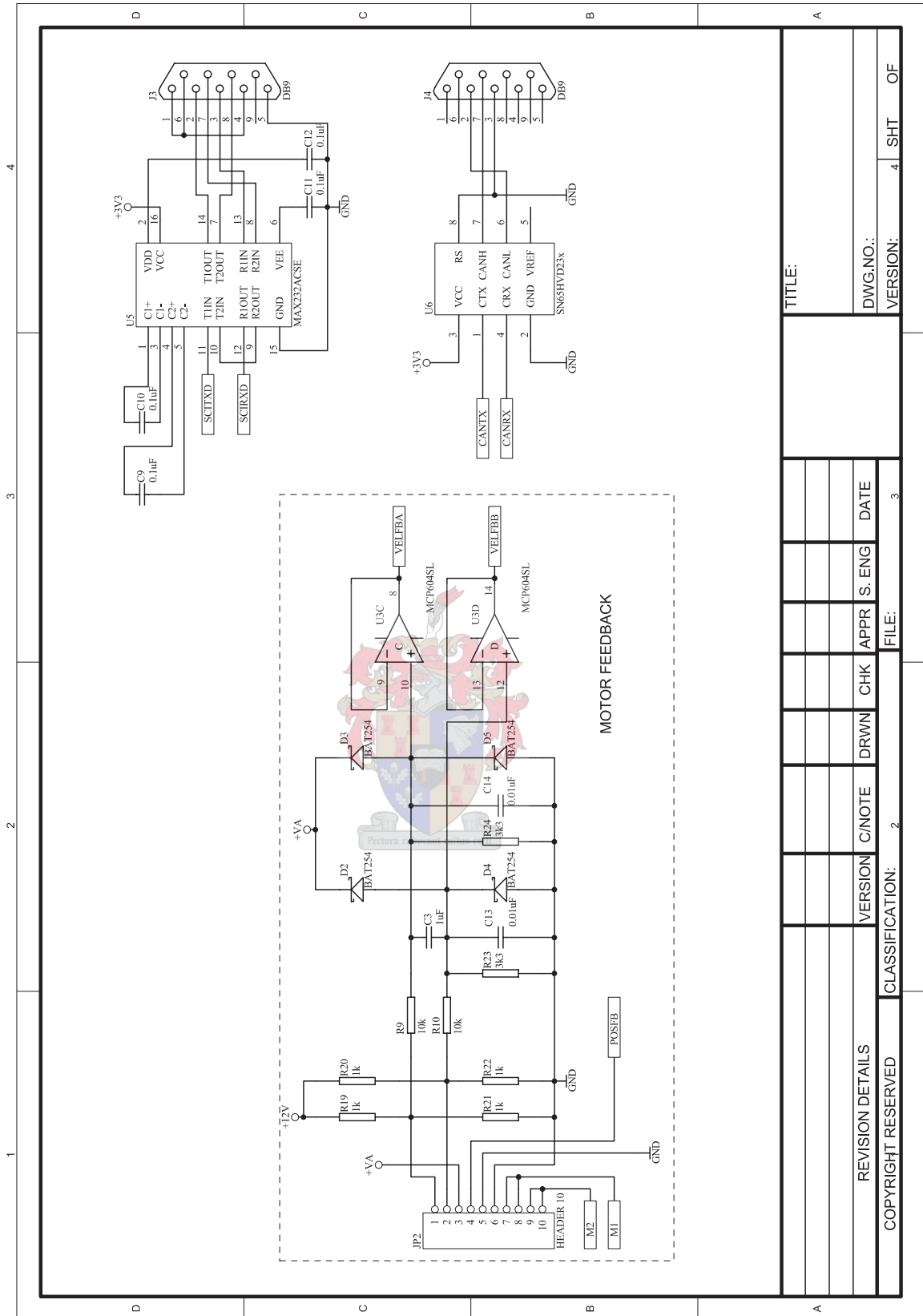


Figure C.4: DC motor Electronics schematic

# Appendix D

## Current Loop

### D.1 Sampling frequency

The sampling time is chosen as a multiple of the PWM frequency. An 8 bit register is set on the microprocessor to change the duty cycle of the PWM. With a resolution of 256 (0 to 255 for 100% to 0% Duty Cycle) and a time base of  $217.01nsec$  per tick, one Duty Cycle will be  $55.555\mu sec$ .

$$\frac{System\ clk}{4} = \frac{18,432MHz}{4} = 4.608MHz \Rightarrow 217.01nsec$$

$$217.01nsec \times 256 = 55.555\mu sec = 18kHz$$

If the sampling frequency is chosen as 50 times slower than the PWM frequency, the sampling frequency will be 360Hz.

$$T_s = 50 \times T_{PWM} = 50 \times 55.555\mu sec = 2.77777msec = 360Hz$$

The current measurement and control loop is therefore implemented at this speed.

## D.2 Current Measurement

The given circuit measures the current through a resistor R as  $V_a$ .  $V_a$  is then filtered and multiplied as seen in Fig. 4.10. The equations for the gain and the filter are as follows:

$$V_{out} = V_2 \frac{R_{15} + R_5}{R_{15}} \quad (D.1)$$

$$V_1 = V_2 \quad (D.2)$$

$$V_1 = V_a \frac{\frac{1}{sC_6}}{\frac{1}{sC_6} + R_7} \quad (D.3)$$

When Eq. D.1, D.2 and D.3 are combined:

$$\frac{V_{out}}{V_a} = \frac{R_{15} + R_5}{R_{15}} \frac{\frac{1}{C_6 R_7}}{s + \frac{1}{C_6 R_7}} \quad (D.4)$$

With  $C_6 = 0.1\mu f$  and  $R_7 = 10k\Omega$ , the cut-off frequency of the current sensing voltage is:

$$\frac{1}{C_6 R_7} = 1000 rad/s = 159.15 Hz$$

Because 159.15Hz is less than 2 times the sampling frequency, it will act as an anti-aliasing filter and reduce noise levels of the measurement.

The datasheet of the DC motor gives a torque constant of 16.3mNm/A. For a maximum of 3A from the power supply, the motor will have an output of 48.9mNm. Choosing a maximum current  $I_a$  equal to 3.5A, the voltage across resistor R is:

$$V_a = I_a R = 3.5 \times 0.15 = 0.525V$$

The maximum voltage that the A/D converter can read is 2.45V. With this in mind, the gain of the op-amp must be:

$$Gain = \frac{2.45}{0.525} = 4.67$$

The gain of the opamp is (from Eq. D.4):

$$\frac{R_{15} + R_5}{R_{15}} = 4.67$$

With  $R_{15}$  equal to  $2k7\Omega$  and  $R_5$  equal to  $10k\Omega$  the gain is 4.7.

The Current in Ampere is related to Current in ticks as follows:

$$1[A] \times R \times OPAMP[Gain] \times A/D \text{ Conversion} = [ticks] \quad (D.5)$$

$$1[A] \times 0.15 \times 4.7 \times \frac{2048}{2.45} = 589[ticks] \quad (D.6)$$

### D.3 Current Loop Controller

For a continuous PI controller the equations are as follows:

$$D(s) = K_p + \frac{K_i}{s} = \frac{K_p s + K_i}{s} = K_p \frac{s + a}{s} \quad (D.7)$$

where  $a = \frac{K_i}{K_p}$

With the discrete PI controller as:

$$D(z) = \frac{u(z)}{e(z)} = K_p \left( \frac{z + (aT - 1)}{z - 1} \right) \quad (D.8)$$

$$u[n] = u[n - 1] + K_p e[n] + (aT - 1)K_p e[n - 1] \quad (D.9)$$

The controller was chosen with  $K_p = 0.6$  and  $K_i = 233.1$  (Sampling frequency = 360Hz), Therefore:

$$D(z) = \frac{0.6z + 0.0475}{z - 1}$$

$D(z)$  is implemented with the following equation:

$$u(n) = u(n - 1) + 0.6 e(n) + 0.0475 e(n - 1) \quad (D.10)$$

$$u(n) = u(n - 1) + (e(n) + (e(n - 1) \times 8/101)) \times 6/10 \quad (D.11)$$

At each sampling time, the following was done on the microcontroller:

1. Current is read from the A/D Converter
2. The error current is calculated
3. The controller equation is implemented as in Eq. D.11

The reason for not using floats on the microprocessor is because it is calculative expensive.  $e[n]$  is the current error at the sample time and  $e[n-1]$  is the current error at the previous sample time.  $u[n]$  is the output of the controller in percentage duty cycle and  $u[n-1]$  is the previous output. As stated in Section 4.2.1, the controller output is in percentage duty cycle but the microcontroller changes a corresponding 8 bit register. For this reason the controller output is multiplied by 256. Also, to prevent saturation, the controller output is divided by 1767, corresponding to the maximum measured current 3A (Eq. D.6).



# Appendix E

## Velocity Loop

### E.1 Discrete Controller

From Matlab, the discrete controller is:

$$D_{\omega}(z) = D(z)F(z) = \frac{0.6794z - 0.6794}{z^2 - 1.66z + 0.6603} \quad (\text{E.1})$$

with a sampling frequency of 360Hz.

This however cannot be implemented as is due to the absent velocity conversion constant. The conversion from  $\omega$  [rad/s] to  $\omega$  [ticks] has to be included. This was already computed as 1.5014 in Appendix E.2. The designed controller gives current as output. The input to the current controller only accepts a current command in ticks. For this reason the I[A] to I[ticks] constant is also included. This constant was already calculated in Appendix D.2. With these constants and Eq. E.1 the implemented controller is,

$$D_{\omega}(z) = \frac{267.7z - 267.7}{z^2 - 1.659z + 0.6592} \quad (\text{E.2})$$

The implemented difference equation:

$$y[n] = 267.7u[n - 1] - 267.7u[n - 2] + ((166y[n - 1] - 66y[n - 2])/100) \quad (\text{E.3})$$

$y[n]$  is the input to the current controller.  $u[n]$  is the velocity error. With this equation implemented, the output is already in current ticks for the current loop controller.

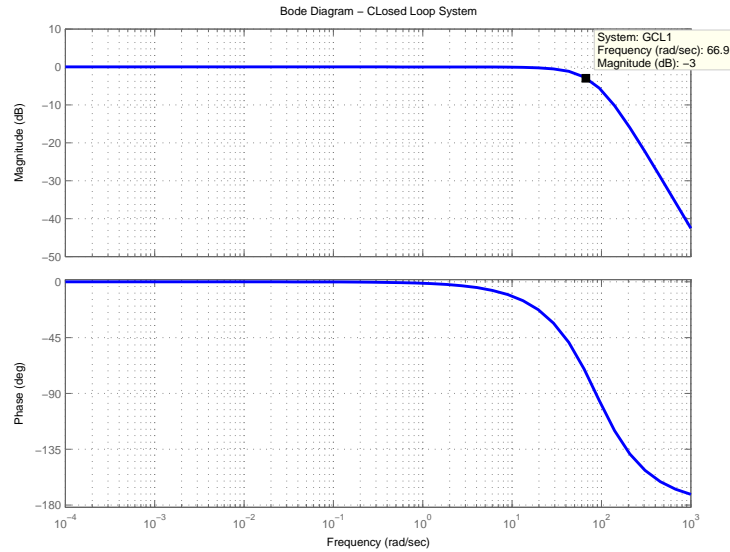


Figure E.1: Bode Plot of Closed loop Velocity Controller Plant

## E.2 Velocity measurement

The maximum measured voltage on  $V_{\omega 1}$  or  $V_{\omega 2}$  (Fig. 4.15) (depending on which way the motor turns) is 8.5V. This voltage is buffered with an op-amp with supply rails of 3.3V. This implies that the measured voltage from the tachometer must be multiplied with 0.388 ( $8.5V / 3.3V = 0.388$ ). The voltage dividing in Fig. 4.15 is done with the following equation:

$$\frac{V_{elFBA}}{V_{\omega 1}} = \frac{R_{24}}{sR_9R_{24}C_{14} + (R_9 + R_{24})} \quad (E.4)$$

With  $R_{24} = R_{23} = 6k8\Omega$  and  $R_9 = R_{10} = 12k\Omega$  the gain is 0.3617.  $C_{14} = C_{13} = 0.01\mu F$  gives a bandwidth of 3660Hz. This can be ignored because the bandwidth of the velocity loop is 10Hz.

If the motor is turned at 6000RPM, the voltage  $V_{\omega}$  is equal to 3.12V. When this is multiplied by the gain 0.3617, the maximum measured voltage is 1.13V. This is less than half of the voltage the A/D converter can convert. This implies very poor velocity measurement resolution. Controlling the speed of the momentum wheel at lower velocity is difficult due to this resolution problem.

To get from  $\omega$  [rad/s] to  $\omega$  [ticks] the following gain is considered from Fig. E.2,

$$\omega \text{ [rad/s]} \times 1.5014 = \omega \text{ [ticks]}$$

$$\text{RPM} \times 0.157223 = \omega \text{ [ticks]}$$

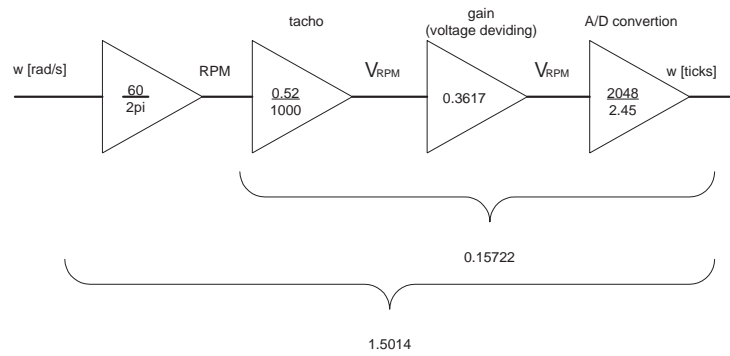


**Figure E.2:** Angular velocity in [rad/s] to [ticks]

### E.3 Anti Aliasing filter

The low pass Butterworth filter was derived from [2]. The cutoff frequency can be chosen with,

$$RC = \frac{1}{2\pi f_c} \quad (\text{E.5})$$

Choose  $f_c = 100\text{Hz}$  and  $C = 100\text{nF}$ . This gives  $R = 15\text{k}\Omega$ . The gain of the opamp configuration will be chosen as unity with  $R_2$  open circuit and  $R_1$  short circuit.

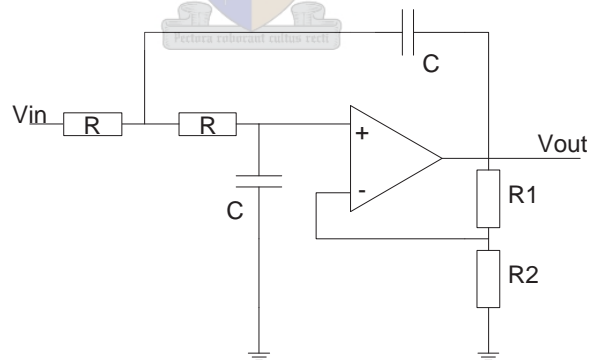


**Figure E.3:** Butterworth low pass filter



## E.4 Pre-Filter

With a torque constant of 16.3mNm/A and a maximum current of 3A from the power supply, the torque delivered is 48,9mNm. The inertia of the motor is  $1.500911 \times 10^{-3} kg m^2$ . With these constants, the maximum acceleration of the momentum wheel is calculated as:

$$T = I\dot{\omega} \quad (E.6)$$

$$\dot{\omega} = \frac{T}{I} \quad (E.7)$$

$$= \frac{48,9mNm}{1.500911 \times 10^{-3}kg m^2} \quad (E.8)$$

$$= 32.58 rad/s^2 \quad (E.9)$$

$$= 48.82 ticks/s \quad ([rad/s] \text{ to } [ticks] \text{ conversion from Appendix E.2}) \quad (E.10)$$

Thus the gradient of the speed controller reference may not exceed 48.92 [ticks/s].

$$Gradient = \frac{y[n] - y[n - 1]}{T_s} \leq 48.92, \quad \text{with } T_s = \frac{1}{360} = 0.002777sec. \quad (E.11)$$

$$y[n] - y[n - 1] \leq 0.1359 \quad (E.12)$$

Through experimentation it was found that the gradient can be increased to 73.6rad/s<sup>2</sup> (110.5 ticks/s). The reason for this is the fact that the battery can deliver much more current than the 3A from the power supply, therefore the gradient equation changes to:

$$Gradient = y[n] - y[n - 1] \leq 0.3073 \quad (E.13)$$

$y[n]$  and  $y[n-1]$  represent the present  $\omega_{ref}$  and previous  $\omega_{ref}$  respectively. The slew rate limiter is implemented by adding 3073 to the reference if the input is greater than the reference. A subtraction is done when the reference is greater than the input. After this is done, the reference is divided by 10000. It was implemented this way because floats were calculative expensive.

# Appendix F

## Strategy Implementation

### F.1 Inertial relationship between the Momentum wheel and Cart

From [8] the following equation is relevant for the conservation of angular momentum between the cart and the momentum wheel,

$$T_{MW} = -T_{cart} \quad (F.1)$$

$$I_{MW}\dot{\omega}_{MW} = -I_{cart}\dot{\omega}_{cart} \quad (F.2)$$

$$\dot{\omega}_{cart} = \frac{-I_{MW}}{I_{cart}}\dot{\omega}_{MW} \quad (F.3)$$

Integrating both sides and setting initial values to zero  
the angular velocity of the cart is,

$$\omega_{cart} = \frac{-I_{MW}}{I_{cart}}\omega_{MW} \quad (F.4)$$

### F.2 Discrete controller of the cart angular velocity

The controller implemented in Eq. 5.4 was converted to a discrete version using Matlab. The sampling frequency is 360Hz. Also included is the constant in Appendix F.3.

$$D_{\omega(cart)}(z) = \frac{-0.06650z + 0.0643}{z - 1} \quad (F.5)$$

The difference equation is implemented with floating point values.

### F.3 Conversion of gyro measurement

To scale the gyro measurement in  $\omega$ [rad/s] to  $\omega$ [ticks] the following is considered. The gyro converts  $^\circ/s$  to a voltage with  $12.5 \times 10^{-3} \text{V}/^\circ/s$ . The gyro measurement range is from 0.26V to 4.75V. The A/D converter can only read up to 2.45V. An opamp with gain 0.5058 is therefore implemented. Fig. F.1 illustrates the conversion. The conversion constant equals 605.63.

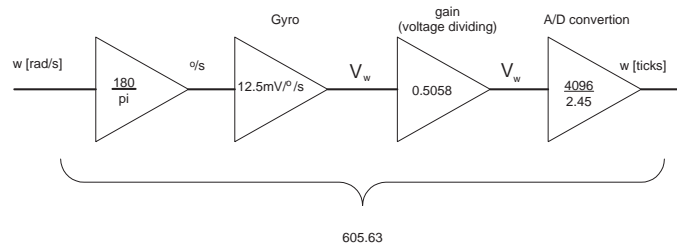
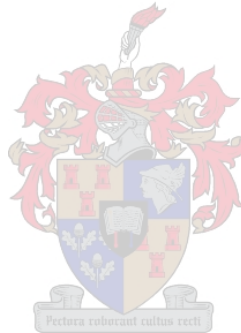


**Figure F.1:**  $\omega$  [rad/s] to  $\omega$  [ticks] conversion of the cart



## F.4 Inertial measurement of the Cart

The moment of inertia is calculated using the principle of conservation of angular momentum (Eq. F.2). The inertia of the momentum wheel is known,  $I_{MW} = 1,5 \times 10^{-3} \text{kg m}^2$ . The momentum wheel is accelerated at a constant rate on the air bearing table. Linear angular acceleration is used for the calculation. The wheel was accelerated from rest were the torque of the momentum wheel is still at maximum. The gyro [9] gives the angular rate of the cart. The results of 6 consecutive tests are in Table F.1.

$$I_{cart} = \frac{-I_{MW}}{\dot{\omega}_{cart}} \dot{\omega}_{MW} \quad (\text{F.6})$$

$\omega_{MW}$	$\omega_{cart}$	$I_{MW}$	$I_{cart}$
59.87486154	-0.118289872	$1.5 \times 10^{-3}$	0.75925598
-59.86410847	0.109820513	$1.5 \times 10^{-3}$	0.817662934
-61.6750956	0.119166667	$1.5 \times 10^{-3}$	0.776329875
61.00164704	-0.12814	$1.5 \times 10^{-3}$	0.714082024
61.7457199	-0.11066879	$1.5 \times 10^{-3}$	0.836898822
-57.94016791	0.110104777	$1.5 \times 10^{-3}$	0.789341336

**Table F.1:** Results of Moment of Inertia measurement

The average moment of inertia for the whole cart with batteries, thrusters, electronics and momentum wheel is  $I_{cart} = 0.78 \text{kg m}^2$ . Fig. F.2 illustrates the angular velocities of the cart and momentum wheel. This illustrates a typical inertial measurement.

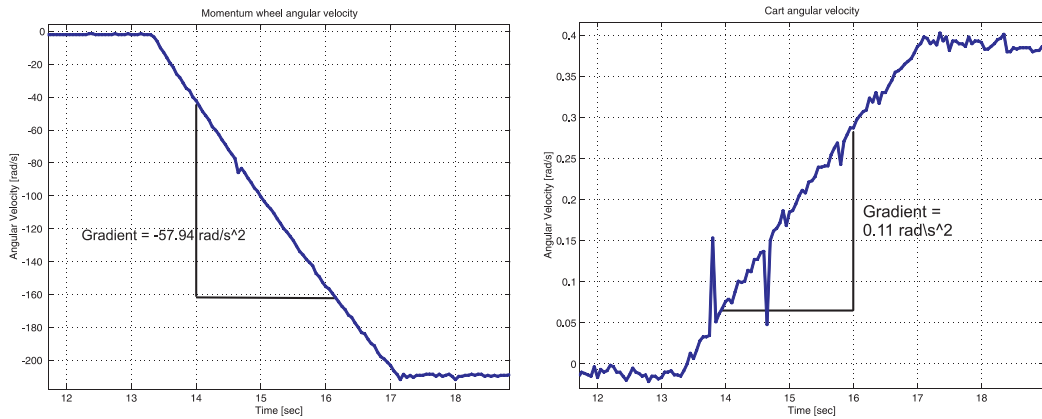


**Figure F.2:** Angular velocity of the momentum wheel and the cart

## F.5 Plant simplification of the Angular velocity controller

The closed loop plant of the angular velocity controller of the cart is:

$$G_{\omega CL}(s) = \frac{575.4(s + 9.5)}{(s + 75 + 48.96j)(s + 75 - 48.96j)(s + 0.6858)} \quad (\text{F.7})$$

With a root locus in Fig. F.3.

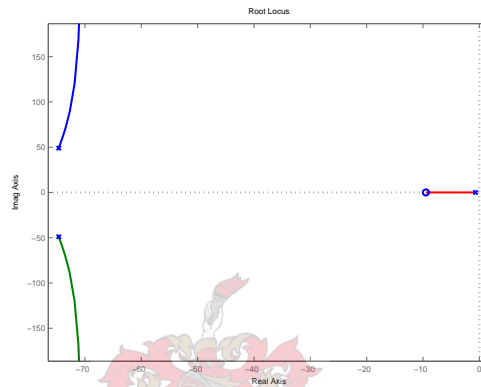


**Figure F.3:** *Root locus of closed loop plant*

Eq. F.7 is approximated with the following,

$$G_{\omega CL}(s) = \frac{0.6858}{s + 0.6858} \quad (\text{F.8})$$

All the high frequency dynamics are omitted. The reason for this being the cart's angle controller bandwidth of 0.07Hz. The high frequency components have no effect. The result of the approximation is illustrated in Fig. F.4.

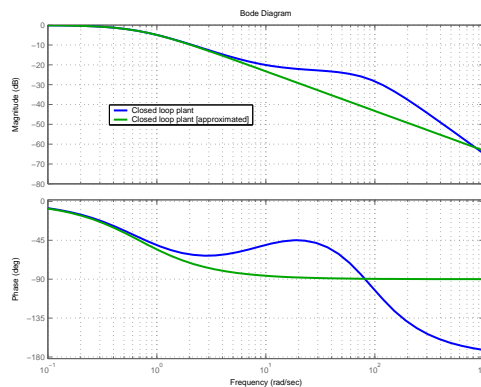


**Figure F.4:** *Bode plot of closed loop angular velocity plant and approximation*

## F.6 Angle acquire constant

From Fig. F.5 and Eq. F.14 a delta distance is calculated.

$$D1^2 = D^2 + \left(\frac{L}{2}\right)^2 - 2D\frac{L}{2}\cos(\rho) \quad (\text{F.9})$$

$$D1 = \sqrt{D^2 + \left(\frac{L}{2}\right)^2 - 2D\frac{L}{2}\cos(\rho)} \quad (\text{F.10})$$

$$D2^2 = D^2 + \left(\frac{L}{2}\right)^2 - 2D\frac{L}{2}\cos(180 - \rho) \quad (\text{F.11})$$

$$D2 = \sqrt{D^2 + \left(\frac{L}{2}\right)^2 - 2D\frac{L}{2}\cos(180 - \rho)} \quad (\text{F.12})$$

Eq. F.10 minus Eq. F.12

$$D1 - D2 = \sqrt{D^2 + \left(\frac{L}{2}\right)^2 - 2D\frac{L}{2}\cos(\rho)} - \sqrt{D^2 + \left(\frac{L}{2}\right)^2 - 2D\frac{L}{2}\cos(180 - \rho)} \quad (\text{F.13})$$

with  $\beta = 90 - \rho$

$$D1 - D2 = \sqrt{D^2 + \left(\frac{L}{2}\right)^2 - 2D\frac{L}{2}\sin(\beta)} - \sqrt{D^2 + \left(\frac{L}{2}\right)^2 + 2D\frac{L}{2}\sin(\beta)} \quad (\text{F.14})$$

With  $D = 1\text{m}$  (average target distance) and  $L = 28.24\text{cm}$  (Chapter 4.1.3) a delta

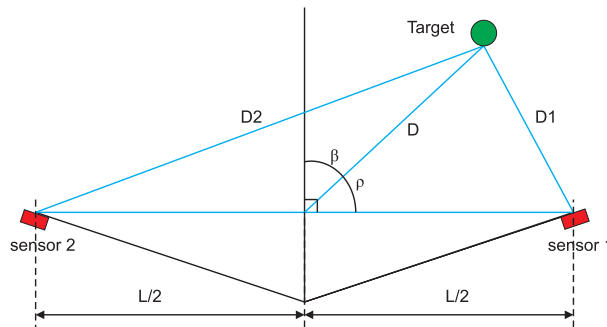


**Figure F.5:** *Delta D*

distance ( $D1 - D2$ ) vs. angle ( $\beta$ ) is plotted. The measurement of delta distance is in seconds and included in Fig. F.6 is a constant to convert distance to time. See the delta time vs. angle graph below. To linearise over an angle range of  $\pm 22.9^\circ$  ( $\pm 0.3989[\text{rad}/\text{s}]$ ), a gradient of 2506.9 [ticks/rad] is calculated. The controller is divided with this value to get the angle in rad/s.

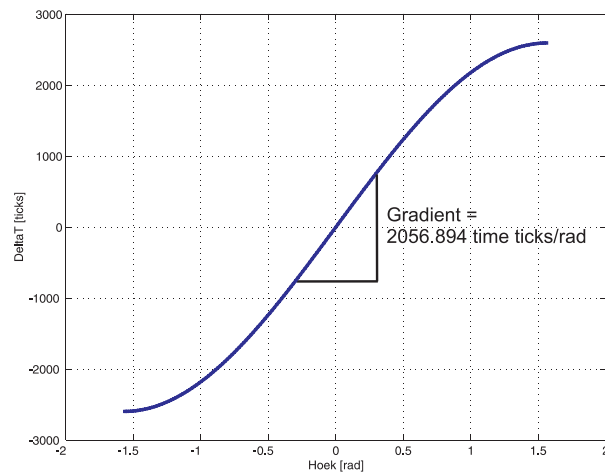
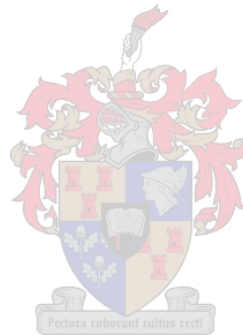


**Figure F.6:** *Delta D (D1 - D2)*

Due to the nature of the strategy the target distance  $D$  could vary, but it will be in the range of 0.9 - 1.1 m. This has little effect on the calculated constant and this variation is omitted.



# Appendix G

## EKF

### G.1 EKF equation derivation

The discrete  $F_k$  is approximated with  $F_{dk} \approx I + F_k T_s$  (Eq. 2.22 and 2.25),

$$F_k = \left. \frac{\partial f(\underline{x})}{\partial \underline{x}} \right|_{\underline{x}=\hat{\underline{x}}_k} = \begin{bmatrix} 0 & 1 & 0 & 0 & 0 & 0 \\ 0 & 0 & 0 & r & 0 & v \\ 0 & 0 & 0 & 1 & 0 & 0 \\ 0 & -r & 0 & 0 & 0 & -u \\ 0 & 0 & 0 & 0 & 0 & 1 \\ 0 & 0 & 0 & 0 & 0 & 0 \end{bmatrix} \bigg|_{\underline{x}=\hat{\underline{x}}_k} \quad (\text{G.1})$$

### G.2 EKF variance calculation

The variance ( $\sigma_m^2$ ) of the resulting acceleration probability density model, and the reciprocal acceleration time constant ( $\alpha$ ) are calculated as [19](process noise):

$$\sigma_m^2 = \frac{A_{max}^2}{3} [1 + 4P_{max} + P_0] \quad (\text{G.2})$$

$$A_{max} = a_x \approx 0.05\text{m}/s^2 \text{ (Maximum acceleration)} \quad (\text{G.3})$$

$$P_{max} = 0 \text{ (Probability of maximum acceleration)} \quad (\text{G.4})$$

$$P_0 = 0 \text{ (Probability of no acceleration)} \quad (\text{G.5})$$

$$\alpha = \frac{1}{50}, \text{ for a lazy turn} \quad (\text{G.6})$$

The variance of the measurement noise is calculated from 5 consecutive measurements (distance and angle). The sensors were set up to measure a target at  $22.5^\circ$ , at a distance



of 1m. The variance of these measurements is given below.

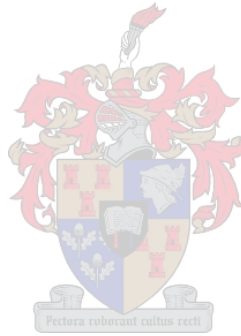
$$\sigma_R^2 = 4.75 \times 10^{-7}, \text{ variance from 5 consecutive distance measurements} \quad (\text{G.7})$$

$$\sigma_\theta^2 = 7.04 \times 10^{-6}, \text{ variance from 5 consecutive angle measurements} \quad (\text{G.8})$$

Because the Kalman filter gain  $L_k$  is related to  $Q_k$  and  $R_k$  (calculated from measurements) with the following:

$$L_k \equiv \sqrt{\frac{Q_k}{R_k}} \quad (\text{G.9})$$

The diagonal elements from Eq. 5.12 were design variables.  $Q_k$  was iteratively found in simulation and implemented as such.



# Appendix H

## Simulation Results

### H.1 Control strategy with angle controller

The table below illustrates the order of commands for the non-linear strategy controller.

<u>State</u>	<u>Control Criteria</u>	<u>Command To</u>	<u>Reference</u>
<b>Initiate</b>		Momentum wheel	-1000 RPM
<b>Initiate</b>		Angular Velocity Control of cart	0 RPM
<b>Initiate</b>		X Thruster (at 25 sec.)	0.8 sec. thrust
<b>Control</b>	$\theta \leq 7^\circ$	Angle control of cart	$0^\circ$
<b>Control</b>	$\phi \geq 36^\circ$	Angular Velocity control of cart	0 RPM
<b>Control</b>	$\phi \geq 45^\circ$	Y thruster ON	1.2 sec. thrust
<b>Control</b>	Y Thruster time ON = 1.2 sec.	Angle control of cart	$0^\circ$
<b>Control</b>	$\phi \geq 68^\circ$	Angular Velocity control of cart	0 RPM
<b>Control</b>	$\phi \geq 90^\circ$	Y thruster ON	2 sec. thrust
<b>Control</b>	Y Thruster time ON = 2 sec.	Angle control of cart	$0^\circ$

**Table H.1:** *Non Linear Strategy Controller*

## H.2 Control strategy with open loop angle control

The table below illustrates the order of commands for the non-linear strategy controller.

<u>State</u>	<u>Control Criteria</u>	<u>Command To</u>	<u>Reference</u>
<b>Initiate</b>		Momentum wheel	-2000 RPM
<b>Initiate</b>		Angular Velocity Control of cart	0 RPM
<b>Initiate</b>		X Thruster (at 25 sec.)	0.5 sec. thrust
<b>Control</b>	$\theta \leq 0^\circ$	Momentum wheel	(-2000 RPM + 850 RPM)
<b>Control</b>	Momentum Wheel RPM $\geq (-2000 + 850)$ RPM	Momentum wheel	-2000 RPM
<b>Control</b>	Momentum Wheel RPM $\leq -2000$ RPM	Angular Velocity Control of cart	0 RPM
<b>Control</b>	Y position $\geq -0.8$	Y thruster ON	1.2 sec. thrust
<b>Control</b>	$\theta \leq -1^\circ$	Momentum wheel	(-2000 RPM + 1010 RPM)
<b>Control</b>	Momentum Wheel RPM $\geq (-2000 + 1010)$ RPM	Momentum wheel	-2000 RPM
<b>Control</b>	Momentum Wheel RPM $\leq -2000$ RPM	Angular Velocity Control of cart	0 RPM
<b>Control</b>	Y position $\geq -0.25$	Y thruster ON	1.7 sec. thrust

**Table H.2:** *Non Linear Strategy Controller*

## H.3 Angular Acceleration of the cart

With the known inertias of the momentum wheel and cart, as well as the angular acceleration of the momentum wheel, the cart's angular acceleration is calculated,

$$\begin{aligned}
 I_{MW}\dot{\omega}_{MW} &= -I_{cart}\dot{\omega}_{cart} \quad \text{with,} & (H.1) \\
 I_{MW} &= 1.5 \times 10^{-3}kg m^2 \\
 I_{cart} &= 0.782265kg m^2 \\
 \dot{\omega}_{MW} &= \pm 73.6rad/s^2 \quad (\text{pre-filter}) \\
 &\text{thus,} \\
 \dot{\omega}_{cart} &= \pm 0.141rad/s^2
 \end{aligned}$$

## H.4 Results for strategy controller with closed loop angle control

The figure below shows actuator commands for the strategy implemented.

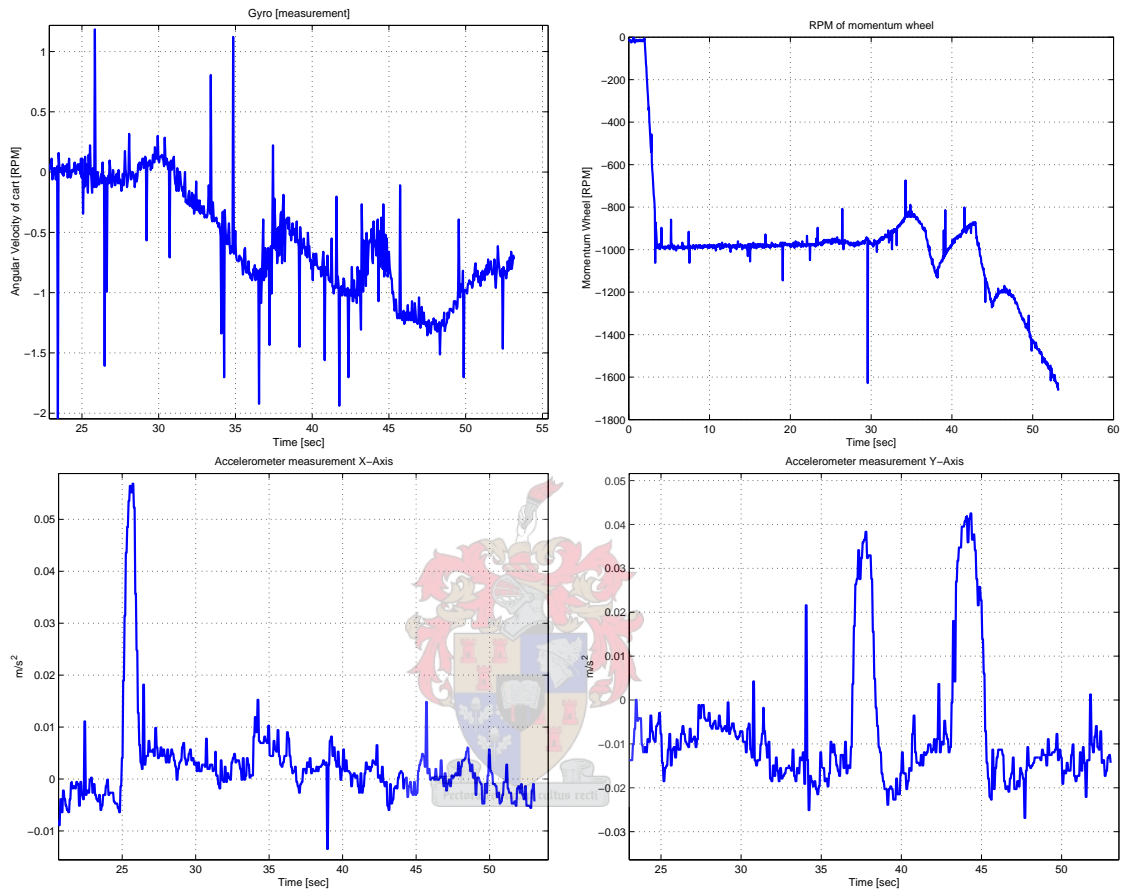


**Figure H.1:** *Actuator commands of the cart*

The reason for the initial condition of the momentum wheel (-1000 RPM) is to avoid transient effects around 0 RPM due to a low resolution RPM measurement. The X thruster is switched on for 0.8 sec. to achieve the initial velocity. The Y thruster is switched on for 1.2 and 2 sec. for the 1st and 2nd corners respectively.

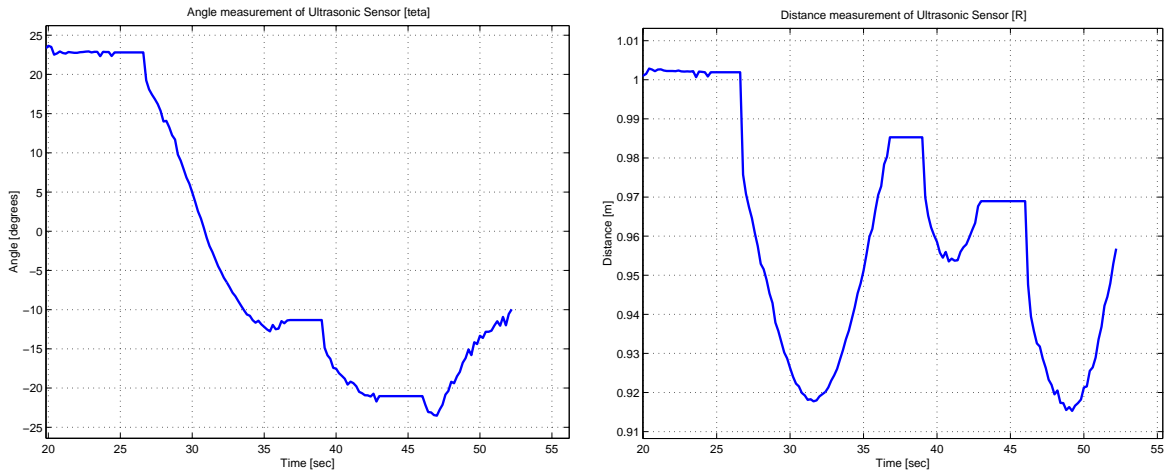


**Figure H.2:** *Ultrasonic measurements*

The calculated measurements from the ultrasonic sensors shows the initial conditions of  $R = 1\text{ m}$  and  $\theta = 22.5^\circ$  from Fig. H.2 at time prior to 25 sec. When the cart starts off from the initial position, the distance and angle increases and decreases as the cart moves along the segmented track. During the thrust period, the ultrasonic sensors are switched off and the measurements are clamped. The vibration and sound intensity interrupts the working condition of the ultrasonic sensors. The flat spots on the measurements are the clamped values.

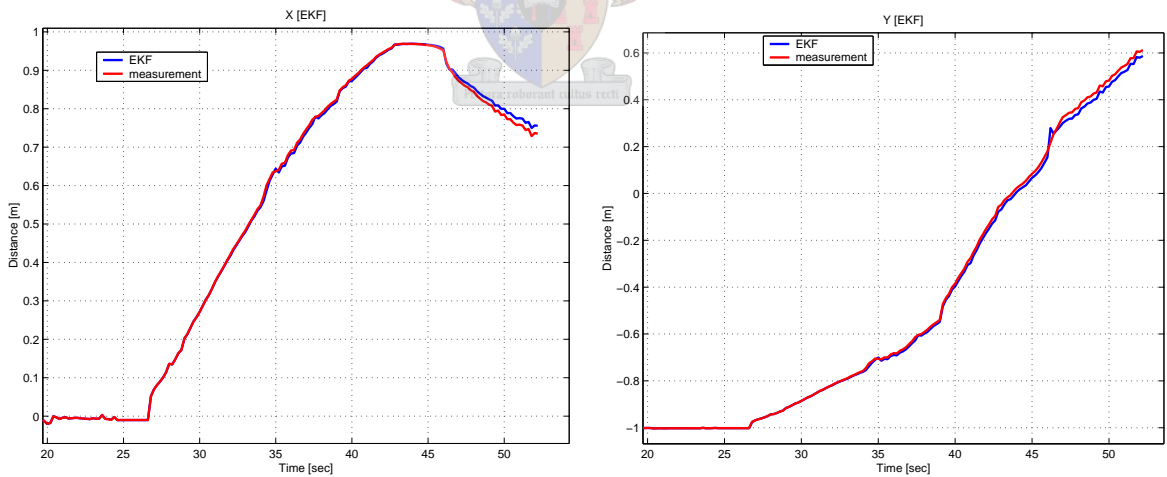


**Figure H.3:** *EKF state measurements*

To illustrate the working of the EKF, the actual position measurements are compared to the estimated values in Fig. H.3. These two figures are confirmation of a working EKF.

The values for the measurements are from from Fig. 5.7:

$$X = R \sin(\phi - \theta) \quad (\text{H.2})$$

$$Y = -R \cos(\phi - \theta) \quad (\text{H.3})$$

$$\begin{aligned} R \text{ and } \theta \text{ calculated from ultrasonic sensors measurements,} \\ \phi \text{ from gyro (integrated)} \end{aligned} \quad (\text{H.4})$$

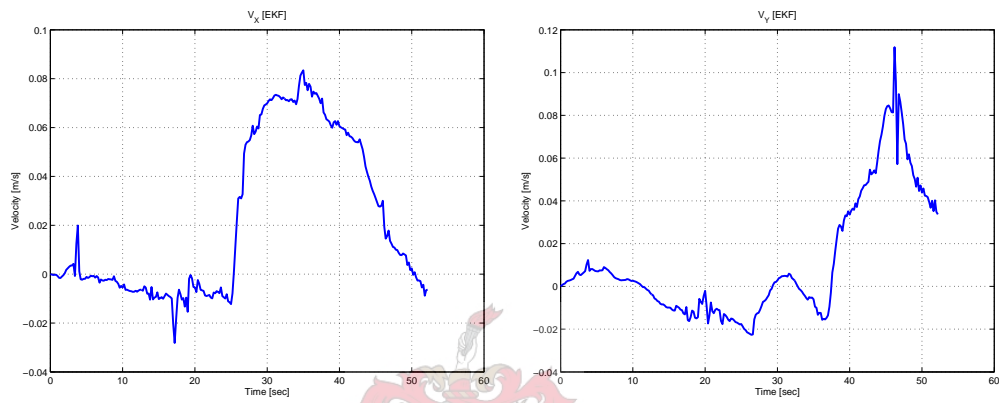
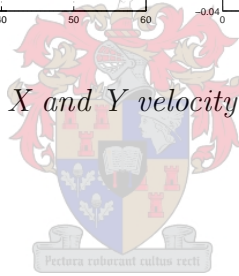


**Figure H.4:** *X and Y velocity estimates from EKF*



## H.5 Results for strategy controller with open loop angle controller

The actuator command measurements are shown below.

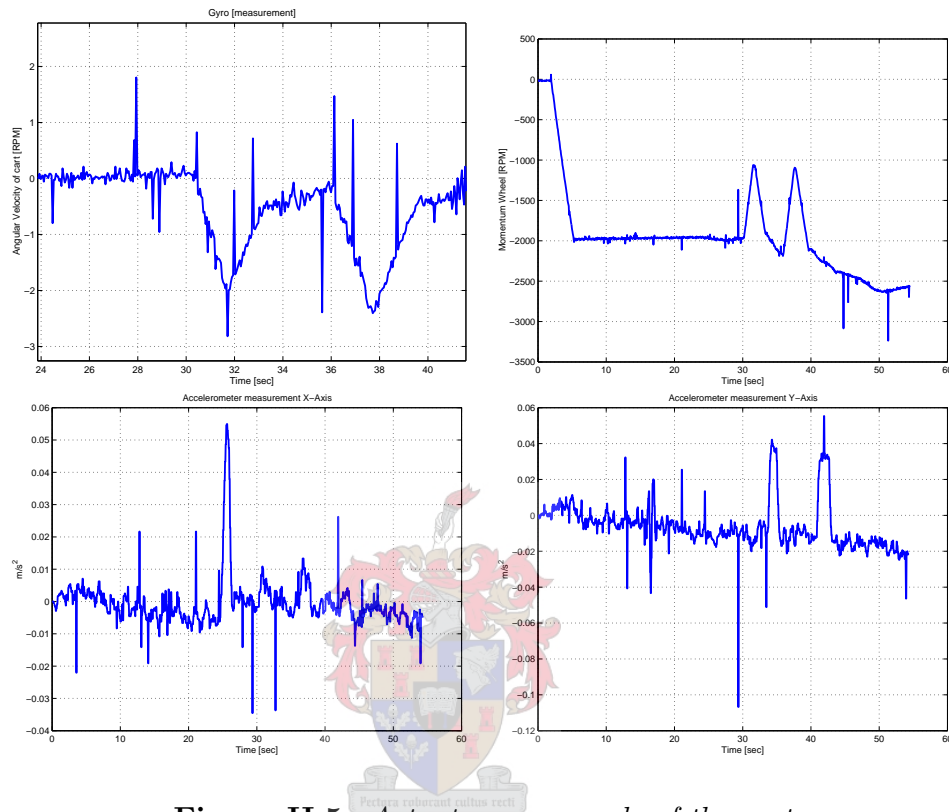


**Figure H.5:** *Actuator commands of the cart*

The initial condition of the momentum wheel is -2000 RPM so as to avoid zero crossings with the open loop angle control for the same reason as given in Appendix H.4. The X thruster is switched on for 0.5 sec. to achieve the initial velocity. For transitions between the 1st and 2nd segment, as well as the 2nd and 3rd, the Y thruster is switched on for 1.2 and 1.7 sec. respectively.

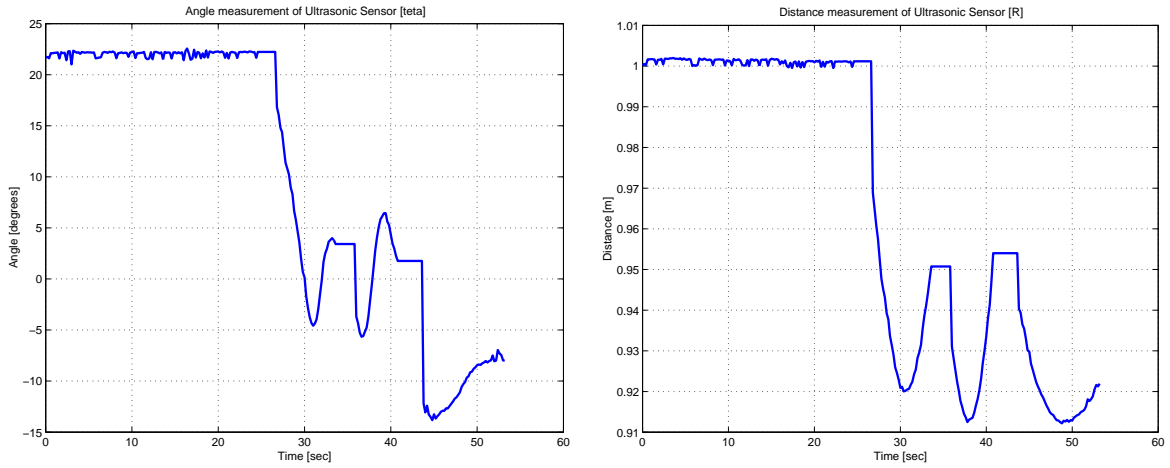


**Figure H.6:** *Ultrasonic measurements*

The initial conditions are shown in Fig. H.6 with  $R = 1\text{m}$  and  $\theta = 22.5^\circ$ . When the cart moves from segment to segment the distance and angle measurement increases and decrease accordingly. The measurements are also clamped for the same reasons as given in Appendix H.4.

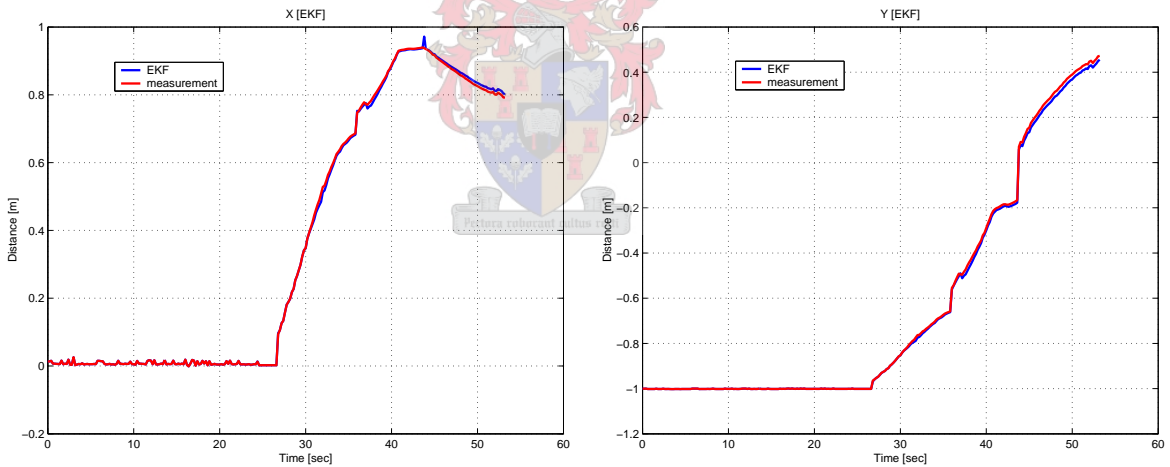


**Figure H.7:** *EKF state measurements*

Fig. H.7 illustrates a working EKF due to the measured and estimated states concurring. The X and Y position are calculated from Eq. H.2 and H.3. The jumps in the X and Y position estimates are due to the ultrasonic sensors measurements being clamped as discussed earlier.



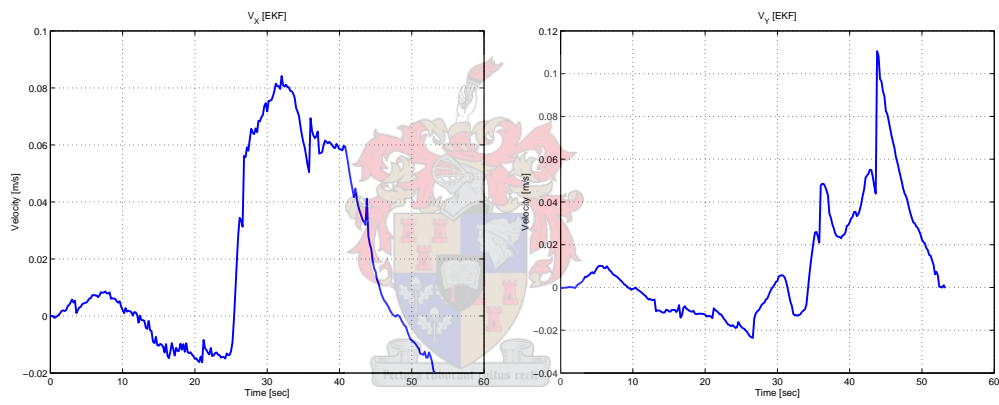


**Figure H.8:** *Velocity estimates from EKF*